Chemistry, Applications, and Future Prospects of Structured Liquids

Journal:	*Chemical Society Reviews*
Manuscript ID	CS-REV-06-2024-000549.R1
Article Type:	Review Article
Date Submitted by the Author:	30-Jul-2024
Complete List of Authors:	Ghaffarkhah, Ahmadreza; The University of British Columbia Hashemi, Seyyed Alireza; The University of British Columbia Okanagan, Isari, AliAkbar; The University of British Columbia Panahi-Sarmad, Mahyar ; The University of British Columbia Jiang, Feng; University of British Columbia, Wood Science Russell, Thomas; University of Massachusetts System, Rojas, Orlando; The University of British Columbia, Chemical and Biological Engineering Arjmand, Mohammad; University of British Columbia,

Chemistry, Applications, and Future Prospects of Structured Liquids

Ahmadreza Ghaffarkhah [1,2]*, Seyyed Alireza Hashemi* [2]*, Ali Akbar Isari*[2]*, Mahyar Panahi-Sarmad* [1,3]*, Feng Jiang* [3]*, Thomas P. Russell* [4,5,6]*, Orlando J. Rojas* [1,7,8]***, and Mohammad Arjmand* [2]***

[1] Bioproducts Institute, Department of Chemical & Biological Engineering, The University of British Columbia, Vancouver, BC V6T 1Z3, Canada

[2] Nanomaterials and Polymer Nanocomposites Laboratory, School of Engineering, University of British Columbia, Kelowna, BC, V1V 1V7, Canada

[3] Sustainable Functional Biomaterials Laboratory, Bioproducts Institute, Department of Wood Science, The University of British Columbia, Vancouver, BC V6T 1Z4, Canada

[4] Polymer Science and Engineering Department, University of Massachusetts Amherst, 120 Governors Drive, Amherst, MA, 01003, USA

[5] Materials Sciences Division, Lawrence Berkeley National Laboratory, 1 Cyclotron Road, Berkeley, CA, 94720, USA

[6] Advanced Institute for Materials Research (WPI-AIMR), Tohoku University, 2-1-1 Katahira, Aoba, Sendai 980-8577, Japan

[7] Department of Chemistry, The University of British Columbia, Vancouver, BC, V6T 1Z1, Canada.

[8] Department of Wood Science, The University of British Columbia, Vancouver, BC V6T 1Z4, Canada.

***Corresponding Author:** orlando.rojas@ubc.ca; mohammad.arjmand@ubc.ca

Abstract

Structured liquids are emerging functional soft materials that combine liquid flowability with solid-like structural stability and spatial organization. Here, we delve into the chemistry and underlying principles of structured liquids, ranging from nanoparticle surfactants (NPSs) to supramolecular assemblies and interfacial jamming. We then highlight recent advancements related to the design of intricate all-liquid 3D structures and examine their reconfigurability. Additionally, we demonstrate the versatility of these soft functional materials through innovative applications, such as all-liquid microfluidic devices and liquid microreactors. We envision that in the future, the vast potential of the liquid-liquid interface combined with human creativity will pave the way for innovative platforms, exemplified by current developments like liquid batteries and circuits. Although still in its nascent stages, the field of structured liquids holds immense promise, with future applications across various sectors poised to harness their transformative capabilities.

Keywords: Structured liquids; Liquid-liquid interface; Nanoparticle surfactant; Supramolecular assembly; Interfacial jamming.

Contents

1 Introduction 7

2 Dynamic and liquid-like assembly of nanoparticles at the liquid-liquid interface 10

3 Structured liquids: Solid-like interfacial assemblies 17

  3.1 Nanoparticle surfactants: From discovery to direct evidence 18

  3.2 From nanoparticle surfactants to macroscale structured liquids 23

    3.2.1 Structured Pickering emulsions and emulgels 23

    3.2.2 All-liquid molding 28

    3.2.3 Liquid streaming and 3D liquid-in-liquid printing 30

    3.2.4 Bicontinuous interfacially jammed emulsion gels (Bijels) 39

      3.2.4.1 Principles and mechanisms related to Bijel fabrication 39

      3.2.4.2 Experimental evidence concerning Bijels 42

      3.2.4.3 Solvent transfer-induced phase separation (STRIPS) 45

      3.2.4.4 NPS-based Bijels 56

  3.3 Structuring liquids through interfacial supramolecular assemblies 58

    3.3.1 Supramolecular assemblies via hydrogen bonding and van der Waals forces 61

    3.3.2 Supramolecular assemblies via electrostatic interaction and π-π stacking 68

    3.3.3 Supramolecular assemblies via host-guest interaction 72

4 Reconfigurability of structured liquids 78

  4.1 External stimuli 78

    4.1.1 Photo-responsive structured liquids 78

    4.1.2 Thermo-responsive structures 83

    4.1.3 Electric-field responsive structures 86

    4.1.4 Magnetic-field responsive structures 90

  4.2 Internal stimuli 96

    4.2.1 pH-responsive structures 96

    4.2.2 Redox-responsive structures 101

5 Applications 105

  5.1 All-liquid systems 105

    5.1.1 All liquid electronics 105

    5.1.2 Environmental remediation using all-aqueous structured liquids 107

    5.1.3 All-liquid microreactors 109

  5.2 From liquid-liquid interface to functional thin film fabrication 120

5.3 Liquid-templated soft materials and aerogels 124
5.3.1 Conductive liquid-templated aerogels for EMI shielding..126
5.3.2 Conductive liquid-templated aerogels for strain/pressure sensing..................................132
5.3.3 Liquid-templated aerogels for oil absorption and water purification...............................133
6 Behind characterization of nanoscale assemblies at liquid-fluid interfaces...................................135
6.1 Direct observation of nanoparticles and supramolecular assemblies at the liquid-fluid interface 136
6.2 Macroscopic evaluation of nanoscale assemblies at liquid-fluid interfaces 148
6.2.1 Interfacial tension measurements 148
6.2.1.1 Determining the binding energy of nanoparticles at the liquid-liquid interface through interfacial tension measurements 150
6.2.2 Expansion/contraction of a pendant drop 153
6.2.3 Interfacial rheology...155
6.2.3.1 Interfacial rheometry at constant area 157
6.2.3.2 Interfacial rheometry at changing area using droplet shape analysis.......................160
7 Current challenges and prospects 163
Acknowledgments 167
References 168

Table of Abbreviations

2D SOFs	Two-dimensional supramolecular organic frameworks
α-CD	α-cyclodextrin
Alg-β-CD	Alginate-modified β-cyclodextrin
AFM	Atomic force microscopy
Azo	Azobenzene
AzoC12	Azobenzene-functionalized alkyl chains
Azo-PLLA	Azo-terminated poly-L-lactide
Azo-PS	Azo-terminated polystyrene
Azo-PVA	Azo-terminated PVA
Bijels	Bicontinuous interfacially jammed emulsion gels
CB[8]	Cucurbit[8]uril
CNCs	Cellulose nanocrystals
CNC-OSO_3H	Sulfate-functionalized cellulose nanocrystals
CNF	Cellulose nanofiber
CR	Congo red
CTAB	Cetyltrimethylammonium bromide
DCE	1,2-dichloroethane
DEP	Diethylphthalate
DTBE	2,2′-dithiobis[1-(2-bromo-2 methylpropionyloxy)ethane]
FC-PLLA	Ferrocene-terminated PLLA
FML	Ferromagnetic liquid
Fc-PLLA	Ferrocene-terminated PLLA
GISAXS	Grazing-incidence small-angle X-ray scattering
GIS-XPCS	Grazing incidence small angle XPCS
GO	Graphene oxide
HRP	Horseradish peroxidase
IFT	Interfacial tension

mGO	Magnetic graphene oxide
MV	Methyl viologen
MV^{2+}	Oxidized form of methyl viologen
NPSs	Nanoparticle surfactants
PDMS	Poly(dimethylsiloxane)
PDMS-NH_2	Amine-terminated polydimethylsiloxane
PDMS-NH_3^+	Protonated amine-terminated polydimethylsiloxane
PEG	Polyethylene glycol
PNIPAM	Poly(N-isopropylacrylamide)
PNIPMAM	Poly(N-isopropyl methacrylamide)
POSS-NH_2	Aminopropylsobutyl polyhedral oligomeric silsesquioxane
PS-Fc^+	Ferrocenium-terminated polystyrene
PS-NH_2	Amine terminated polystyrene
PS-NH_3^+	Protonated amine-terminated polystyrene
PVA	Polyvinyl alcohol
SAXS	Small-angle X-ray scattering
SEM	Scanning electron microscopy
STRIPS	Solvent transfer-induced phase separation
TEM	Transmission electron microscopy
TOPO	Tri-n-octylphosphine oxide
UCST	Upper critical solution temperature
WAXS	Wide-angle X-ray scattering
XPCS	X-ray photon correlation spectroscopy

*A complete list of abbreviations is also provided in Table S1 of the supporting information.

1 Introduction

Structured liquids are soft materials that combine the flowability of liquids with the structural stability of solids. In general, designing structured liquids relies on the inherent characteristics of liquid-liquid interfaces that afford the assembly of a wide range of nanoparticles and supramolecules. These components can be densely packed through chemical and/or physical manipulation to generate compartmentalized liquid-in-liquid systems. In these systems, the densely packed interfacial layer ensures structural stability, while the colloidal flowability within the compartmentalized liquid provides malleability similar to liquids. This configuration allows for the creation of various structured all-liquid constructs capable of performing chemical reactions or specific tasks in the liquid state, [1, 2] and even serve as a new generation of templates to fabricate other classes of soft materials, such as aerogels.[3]

The power and beauty of structured liquids were first demonstrated by the interfacial assembly and jamming of nanoparticles at the liquid-liquid interface, where the inherent properties of nanoparticles can be integrated into the final structures to design programmable all-liquid constructs.[4] In practice, interfacial jamming occurs when nanoparticles dispersed in one liquid interact with ligands possessing complementary functionalities suspended or solubilized in a second immiscible liquid. This interaction results in the formation of nanoparticle surfactants (NPSs) that, upon packing, arrest the decrease in interfacial area and thereby stabilize highly non-equilibrium liquid shapes.[3] Due to the nature of NPS assemblies, the bonding energy and packing order of nanoparticles at the liquid-liquid interface can be coded to impart responsiveness to the final constructs.[5, 6] Such a unique reconfigurability has been explored for designing a wide range of functional soft materials, including reconfigurable discrete droplets,[7, 8] molded liquid objects,[9] 3D all-liquid-in-liquid printed constructs,[10] and even a new generation of bicontinuous interfacially jammed emulsion gels (bijels).[11]

Later on, the concept of structured liquids increased in breadth through the development of a wide range of all-liquid reconfigurable constructs based on interfacial assemblies of supramolecules at the liquid-liquid interface. In this scenario, supramolecules form a knitted network at the interface that resists not only compression but also expansion forces, the latter not possible with structured liquids formed with NPSs.[12] Such an interfacial network can also be designed dynamically, allowing the connection and junction of supramolecular assemblies to break and reform repeatedly. In such systems, the interfacial assemblies are stress-free, allowing the resultant structured liquids to be expandable or inflatable.[12] This structural design concept, despite being relatively new, offers potential for developing 3D structured liquids and microfluidic systems with reconfigurable characteristics and applications ranging from on-demand chemical separation and encapsulation to stimuli-responsive devices.[12, 13]

To date, the concept of structured liquids and their underlying mechanisms have been explored in several review articles.[14] These studies have addressed key topics, ranging from dynamic and liquid-like assemblies of nanoparticles to NPSs and,[1, 2] more recently, interfacial assemblies of supramolecules at the liquid-liquid interface.[12] However, a comprehensive perspective comparing the differences and similarities in the chemistry of these assemblies, along with exploring the potential for combining their advantages, has been absent from the literature. Moreover, the mechanisms discussed in the previous review articles have been recently applied to a wider variety of nanoparticles and supramolecules, each with novel chemistries and unique characteristics that merit detailed discussion. For example, the well-established concept of NPS has recently evolved to include functional nanomaterials such as graphene and MXene, presenting several new opportunities that could significantly impact the application and future prospects of these soft functional materials.

Apart from the underlying mechanisms and chemistry responsible for the formation of structured liquids, previous review articles have also highlighted their potential in designing novel systems that were unimaginable a few decades ago. Examples include all-liquid batteries and electronics,[15, 16] liquid microreactors,[17] and all-liquid robots.[18] However, in this rapidly evolving field, some significant developments have not been addressed. For instance, emerging applications of structured liquids, such as their use as templates for the fabrication of other soft materials like aerogels with programmable properties[19] and the development of microreactors and microfluidics capable of performing on-demand reactions[20, 21] have been barely discussed. Additionally, innovations in the choice of materials, reconfigurability of structured liquids, and underlying mechanisms governing the fabrication of these new classes of soft materials have not been systematically reviewed. Finally, characterizing the assembly and jamming of different species at the liquid-liquid interface is another topic that has received limited attention.

In what follows, we will present the most important topics in the field of structured liquids, starting from dynamic and solid-like assemblies of nanoparticles at the liquid-liquid interface (Sections 2-3). Our focus will be on the chemistry of these assemblies alongside various mechanisms that can be used to design a range of 3D structured liquids, from structured emulsion gels (emulgels) and molded liquids to 3D all-liquid-in-liquid printing and bijels. We also devote sections to the chemistry and mechanisms of supramolecular assemblies, highlighting their differences with NPS assemblies (Section 3). Knowing the background and concepts, we delve into the reconfigurability of structured liquids (Section 4) and applications (Section 5). We also discuss various strategies that can characterize the interfacial assembly and jamming of nanoparticles and supramolecules (Section 6) and share our ideas and prospects regarding this evolving field (Section 7), a field that is currently in its infancy but will change our perspective regarding reconfigurable, functional, soft materials when it grows to its potential.

2 Dynamic and liquid-like assembly of nanoparticles at the liquid-liquid interface

At the interface of two immiscible liquids, such as oil and water, molecules are subjected to opposing intermolecular forces—cohesive forces within each liquid and adhesive forces at the interface.[1, 22, 23] These forces generate an energy barrier that impedes the expansion of the interface and the mixing of the immiscible liquids. For instance, when a container holding immiscible oil and water phases is shaken, the dispersed phase tends to form spherical droplets.[24] These droplets have the lowest surface area in contact with the secondary immiscible phase, consequently experiencing the lowest energy difference between the two immiscible phases.[24] However, in the absence of additional external influence, these droplets will merge, eventually creating two distinct layers. The lighter liquid will settle atop the denser one, delineated by a flat interface that minimizes the system's interfacial area.

The concept of an energy barrier between two immiscible liquids becomes most relevant in the presence of colloidal solid particles in one of these phases. In this scenario, solid particles segregate to the interface and position themselves between the immiscible liquids, effectively reducing the interfacial energy between the two phases.[24] This arrangement of solid particles at the liquid-liquid interface is commonly used to stabilize both oil-in-water and water-in-oil Pickering emulsions.[1] In this context, the surface wettability of the particles, characterized by their contact angle (θ) at the three-phase line (solid-liquid-liquid), essentially governs the equilibrium positioning of the particles at the interface. If θ <90°, indicating greater hydrophilicity, the particles stabilize oil-in-water emulsions. Conversely, if θ>90°, indicating increased hydrophobicity, the particles stabilize water-in-oil emulsions.[1, 25]

Typically, the migration of a single particle towards the oil/water interface results in a decrease in the energy barrier between the two immiscible phases, denoted as ΔE. This change can be calculated by considering the square of the particle's effective radius (R) and the interfacial tensions between the oil and water (γ_0), i.e., a detailed discussion, including the relevant equation, is provided in Section 6 of this paper. [1] This clearly illustrates the impact of solid particle sizes on reducing the interfacial energy barriers between two immiscible fluids. Since ΔE is proportional to R^2, the reduction in energy barrier is significantly greater for micrometer-sized solid particles compared to nanoparticles. As a result, the assembly of nanoparticles at the liquid-liquid interface is dynamic or liquid-like in nature. So, not only does thermal energy impart mobility to the nanoparticles, but it is sufficient to induce desorption of the nanoparticles from the interface.[25]

In this scenario, nanoparticles continuously adsorb onto, desorb from, and exchange positions with those in the bulk liquid phases. This phenomenon can be illustrated in water-in-oil emulsion systems. As nanoparticles stabilize the interface, they form a monolayer-like structure.[1] However, this layer is far from static; it continually interacts with nanoparticles dispersed in the surrounding fluids. A key factor governing this exchange is the relationship between nanoparticle radius and interfacial binding energy. Larger nanoparticles exhibit significantly stronger binding, enabling them to displace smaller nanoparticles already residing at the interface. When the size difference is substantial, the mobile nature of the nanoparticle assembly even permits phase separation within the interfacial plane, driven purely by nanoparticle size.[1]

The aforementioned liquid-like behavior of nanoparticle assemblies at the liquid-liquid interface was first visually tracked by Russell and coworkers.[23] To accomplish this, they investigated the assembly of tri-n-octylphosphine oxide (TOPO)–capped cadmium selenide (CdSe) nanoparticles at the toluene/water interface using various characterization techniques, including three-dimensional confocal microscopy. Their results revealed that nanoparticles with an average diameter of ≈1.6 nm cannot stabilize water droplets in the external toluene phase, whereas nanoparticles with a diameter of 2.8 nm can.[2] This size-dependent assembly can be attributed to the fact that larger nanoparticles exhibit a higher propensity to assemble at a liquid-liquid interface, thereby minimizing the Helmholtz free energy.

Furthermore, the low energy associated with the liquid-like assembly of nanoparticles at the toluene/water interface provides a pathway for a size-dependent displacement of nanoparticles at the interface. In this context, upon introducing 4.6-nm nanoparticles to aqueous droplets stabilized by 2.8 nm CdSe, larger particles were observed to displace smaller nanoparticles at the interface, as depicted in Figure 1a. This inherent tendency to displace small nanoparticles with larger ones can be leveraged for applications related to controlled-release encapsulation, including cargo delivery and size-dependent assembly/functionalization.

The liquid-like assembly of nanoparticles at the interface also depends on their surface charge, where the packing order of particles can be controlled by adjusting their inherent charge. This phenomenon was explained in a system containing a monolayer of charged citrate-covered gold (Au) nanoparticles without ligands at the heptane/water interface.[26] When heptane is added to an aqueous solution of Au nanoparticles, a layer of charged nanoparticles forms at the interface between water and heptane, as depicted in Figure S1a. However, with the addition of ethanol to the aqueous phase, the packing density of nanoparticles at the interface significantly increases, and a metallic-looking layer forms (Figure S1a, center and right). This layer formation can be explained by reducing the surface charge of nanoparticles upon the addition of ethanol, which significantly reduces the electrostatic repulsion force between nanoparticles at the interface.[6] This concept was further confirmed by reducing the pH of aqueous phase from 5.8 to 2.0. In this scenario, the charge on the Au nanoparticle's surface decreases by protonating the adsorbed citrate ions, resulting in the formation of a dense monolayer at the heptane/water interface, similar to that of adding ethanol to the system.

Subsequently, Duan and colleagues devised a method to adjust the liquid-like assembly of nanoparticles at the oil/water interface by encapsulating them with ligands that end in 2-bromopropionate.[27] Through ligand substitution, hydrophilic Au or silver (Ag) nanoparticles were modified with 2,2′-dithiobis[1-(2-bromo-2-methylpropionyloxy)ethane] (DTBE), resulting in Au-DTBE and Ag-DTBE nanoparticles.[7] The modified nanoparticles readily migrated to the toluene/water interface and formed tightly packed layers, resulting in a film characterized by its metallic luster. Furthermore, Au-DTBE and Ag-DTBE nanoparticles could concurrently migrate to the interface, generating nanoalloy films. Furthermore, a similar surface modification was employed for hydrophobic nanoparticles, such as iron oxide (Fe_3O_4), where monolayers of Fe_3O_4-capped 2-bromo-2-methyl propionic acid were formed at the toluene/water interface.[27]

It is worth noting that the liquid-like assembly of nanoparticles at the liquid-liquid interface has been widely recognized as a simple yet powerful strategy for fabricating thin monolayers of nanoparticles, where the inherent characteristics of nanoparticles can be tuned and effectively locked into the final thin films. A notable example showcased the self-assembly of hydrophilic nanoparticles, such as Au, platinum (Pt), and silicon dioxide (SiO_2), into neatly organized monolayers at the juncture of water and toluene.[28] The addition of ethanol acted as a catalyst, nudging the nanoparticles toward the interface, while sonication further expedited this segregation. After allowing the nanoparticles to assemble at the liquid-liquid interface, the majority of the toluene was removed. This process resulted in the formation of a closely packed monolayer, which can then be transferred onto various surfaces. These films displayed a tight arrangement of nanoparticles (Figures S1c-d). The arrangement and clustering of these nanoparticles were influenced by their surface charge and the molecules attached to their surfaces. For instance, monolayer films of Pt nanoparticles with polyvinylpyrrolidone (PVP) as a stabilizing agent showcased a distinct structural formation. Transmission electron microscopy (TEM) images of these samples indicated that the gaps between Pt nanoparticles were approximately 3 nm, mirroring the actual size of the nanoparticles, with no significant clusters detected within the monolayer film (Figure S1e).

Building upon this, Girault and colleagues introduced the idea of a "liquid mirror" made of Au nanoparticles at the [heptane + 1,2-dichloroethane (DCE)]/water interface.[29] In their study, the unique optical properties of Au nanoparticles were locked into a highly reflective monolayer driven by interfacial forces. To achieve this, they added ethanol to the aqueous phase and sonicated the sample to enhance the migration of Au nanoparticles to the interface, resulting in the formation of ordered monolayer films. Optical images in Figures S1f-g vividly illustrate the formation and reflectivity characteristics of these films at the [heptane + DCE]/water interface under laser irradiation at a wavelength of 532 nm.

Park and colleagues also delved into designing a monolayer of Au nanoparticles at the liquid-liquid interface, specifically the hexane/water interface.[30] Similar to previous studies, the initial treatment of the aqueous phase with ethanol was noted to drive nanoparticles toward the interface. However, to further enhance the packing density and arrangement of nanoparticles at the liquid-liquid interface, 1-dodecanethiol was added to the hexane phase. This compound was observed to attach to nanoparticles at the interface, reducing their surface charges, thereby weakening their electrostatic repulsions and facilitating the formation of closely packed assemblies. Interestingly, they discovered that increasing the concentration of 1-dodecanethiol enhanced van der Waals interactions, enabling entrapped nanoparticles to reorganize within the 1-dodecanethiol matrix after hexane evaporation, ultimately leading to the formation of multilayer structures.

In another study, Russell and colleagues explored the liquid-like assembly of nanoparticles to create transferable monolayers of CdSe.[22] The CdSe nanoparticles were initially capped with TOPO, and upon assembly, these capping agents were chemically crosslinked to form transferable monolayer films. The choice of CdSe nanoparticles was deliberate, as their inherent photoluminescence provided a direct means to examine the spatial organization of the particles at the liquid-liquid interface. Figure 1b illustrates confocal microscopy images of these cross-linked CdSe thin films, showcasing the thickness and uniformity of the assembled membrane. More importantly, these monolayers of CdSe nanoparticles exhibited permeability, presenting numerous potentials in applications ranging from chemical separation to dialysis.[22] Figure 1c demonstrates that when an aqueous solution of sulforhodamine-B was placed at the top of these films, these interracially driven membranes effectively impeded the merging of the dyed droplet and the water phase beneath the membrane. However, due to their permeability, the dye molecules could diffuse into the water phase over time.

It is important to recognize that the dynamic assembly of nanoparticles at the liquid-liquid interface should be viewed as a universal methodology due to the limitless options of nanomaterials available for this process, with numerous applications yet to be explored in future studies. Exploring the potential applications of liquid-like assemblies of nanoparticles, we can consider monolayers of graphene with outstanding electrical conductivity (>1000 S cm^{-1})[31] and optical transmission (>70% at 550 nm), which hold promise for future applications such as sensing, transparent heaters, and electromagnetic interference (EMI) shielding. Furthermore, the interfacial assembly of $NiCo_2O_4$ platelets,[32] ZnO hollow spheres,[33] or SnO_2[34] has already been utilized in designing highly sensitive and stable photodetectors. Another example could be the interracially driven constructs of $Co(OH)_2$ platelet nanofilms, which transform into CoO films and are used as electrically resistive switches upon annealing.[35] In conclusion, the dynamic assembly of nanoparticles at the liquid-liquid interface stands out as one of the most effective strategies for leveraging the inherent characteristics of nanoparticles into final constructs, with numerous potential applications to be explored in the future.

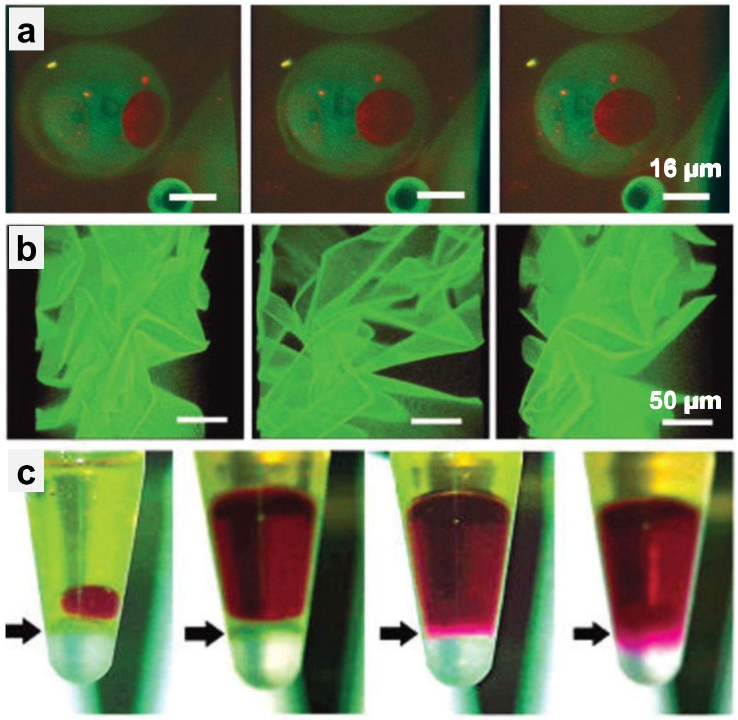

Figure 1: (a) An aqueous suspension of 4.6 nm CdSe nanoparticles (colored red) was injected into a water droplet stabilized by 2.8 nm CdSe nanoparticles (colored green) in an external toluene phase. The three images depict the same sample rotated within the field of view. (a)

Reproduced with permission. Copyright 2003.[23] The American Association for the Advancement of Science. (b) Confocal microscopy images of chemically cross-linked CdSe thin films, highlighting the thickness and uniformity of the assembled membrane. (c) Digital images capture the process of an organic red dye solution becoming entrapped and subsequently diffusing across a membrane composed of chemically cross-linked CdSe nanoparticles. (b-c) Reproduced with permission.[22] Copyright 2003, American Chemical Society.

3 Structured liquids: Solid-like interfacial assemblies

The assembly of solid particles and macromolecules at the liquid-liquid interface becomes even more intriguing if we can engineer the interface to exhibit solid-like behavior. Such a system can help maintain non-equilibrium configurations of immiscible liquids, generating a novel class of soft materials routinely called “structured liquids.” In practice, transitioning from the liquid-like or dynamic assembly of nanoparticles and macromolecules to solid-like behavior can be achieved through interfacial jamming.[36, 37]

Interfacial jamming typically happens when geometric constraints among neighboring particles hinder their mobility at the interface, and even with dynamic forces at the liquid-liquid interface, the solid particles remain attached, i.e., pinned to the interface.[38] For instance, when nanoparticles become jammed at the interface, the temperature gradient and subsequent Brownian motion, which would typically displace nanoparticles in liquid-like assemblies with ease, are unable to eject them from the interface in a jammed system. This scenario is similar to experiencing traffic jams in a crowded city. During normal hours, with fewer cars on the street, maneuvering towards our destination is easy. However, during rush hours, when there are too many cars around us, changing lanes becomes difficult due to geometric constraints imposed by other vehicles, reducing our maneuverability. Similarly, interfacial jamming restricts particle mobility at the liquid-liquid interface, leading to solid-like behavior and maintaining non-equilibrium configurations.[1]

The concept of interfacial jamming and structured liquids has been explored through two primary pathways: the formation and jamming of nanoparticle surfactant (NPS) and the assembly of supermacromolecules at the liquid-liquid interface. In practice, interfacial jamming of NPSs occurs when functionalized nanoparticles in one liquid interact with polymeric/oligomeric ligands possessing complementary functionalities dissolved in another immiscible liquid. This interaction leads to the in-situ formation of NPSs, which subsequently prevents the reduction of the interfacial area and stabilizes highly non-equilibrium liquid shapes. On the other hand, supramolecular jamming involves the formation of a network of interconnected macromolecules at the interface. This structure offers the distinct advantage of creating an interface capable of resisting both compression and expansion, a capability not possible with nanoparticle-structured liquids.[12]

Up to now, these concepts have been used in designing a broad range of interfacially driven soft materials, including structured Pickering emulsions and emulgels,[39] worm-like liquids,[40] molded liquids,[9] and, to some extent, Bijels.[11] In the following sections, we delve into the underlying mechanisms governing structured liquids, examine various morphologies designed based on interfacial jamming, and highlight the most important differences between NPS and supramolecular assemblies.

3.1 Nanoparticle surfactants: From discovery to direct evidence

NPSs are a unique product of interfacial complexation, forming as a result of electrostatic interaction between nanoparticles with active functionalities in one liquid phase and ligands in another immiscible phase.[41] This process was initially introduced by Russell and co-workers in which the interfacial interaction of an aqueous phase containing carboxylated polystyrene (PS) (diameter (D): 15 nm) was examined against an oil phase reinforced with amine-terminated polydimethylsiloxane (PDMS-NH_2).[41] In this system, NPSs were formed at the interface of the two immiscible liquids upon ammonium-carboxylated electrostatic interactions, capable of overcoming the weak interfacial forces governing the nanoparticles' interfacial adsorption.

The mechanism of NPS formation at the interface of two immiscible liquids involves multiple processes, starting from the end-functionalized ligands diffusion to the interface, followed by the diffusion of nanoparticles from bulk toward the interface, and their subsequent assembly at the interface by electrostatic interaction between the nanoparticles and ligands. In the case of in-situ formation of NPSs through electrostatic interactions, the final number of the anchored ligands to the nanoparticles at two immiscible liquid interfaces is self-regulated, acting in a way to reduce the interfacial energy as much as possible.[42] Correspondingly, if the number of anchored ligands is too small, NPS assemblies would draw into the aqueous phase, whereas if the number of these ligands is too large, the NPS would draw into the oil phase, known as phase transfer.[43-46]

The packing of NPSs and their interfacial complexation can be controlled by tuning various parameters, including but not limited to 1) concentration of nanoparticles and ligands, 2) the molecular weight of the amine-terminated polymeric ligands, 3) size of nanoparticles, 4) pH of the medium, and 5) ionic strength of the aqueous phase.[8, 47-51] In general, an increase in the nanoparticles or ligand concentration highly contributes to minimizing the interfacial tension, thereby stabilizing the liquid structures. It is also worth noting that aside from the concentration of the ligands, their size also affects the interfacial assembly and jamming of NPSs, especially in the case of polymeric ligands. For instance, in the case of amine-terminated polymeric ligands, by increasing the molecular weight of ligands, their diffusion into the interface slows down. Therefore, the initial reduction in interfacial tension is much lower. Conversely, reducing the molecular weight of the polymer can lead to a significant decrease in equilibrium interfacial tension as individual polymeric chains become more effective in migrating to the interface.[1]

The formation of NPSs is also significantly influenced by the pH of the medium. This influence arises from the pKa values of the functional groups involved in electrostatic interactions. For instance, in a study by Russell and coworkers, the carboxylic acid group of nanoparticles and the amino groups of ligands have pKa values of approximately 4.2 and 9, respectively.[41] When the pH of the medium is between the pKa values associated with the amine group of ligands and carboxyl functional groups of nanoparticles, the functional groups of nanoparticles get deprotonated while the amine functional groups of ligands get protonated. These deprotonated and protonated species undergo a strong electrostatic interaction that leads to interfacial complexation between nanoparticles and amine-terminated ligands. This process leads to NPS jamming at the interface, creating a thin solid layer capable of preserving the non-equilibrium shape of liquid constructs, facilitating the transition from liquid-like to solid-like behavior.[1, 52, 53] However, if the pH value, for example, is lower than the pKa of carboxylic functional groups, these chemical moieties cannot undergo deprotonation. As a result, we get no NPS formation and jamming at the interface. Therefore, pH is one of the strongest factors for controlling the NPSs assemblies and jamming in a system.

The ionic strength of the aqueous phase is another effective factor that can affect the interfacial packing of NPSs at the oil/water interface. Accordingly, an increase in the ionic strength could decrease the interfacial tension, increasing the density of disordered assemblies of the nanoparticles at the oil/water interface.[49] So far, various types of NPS assemblies have been introduced and employed, preserving the non-equilibrium shape of liquid constructs through the jamming of NPS via a transition to solid-like behavior at the interface of two immiscible liquids. Table 1 tabulates a list of recently practiced interfacially driven systems based on the NPSs formation.

Table 1: Recently developed nanoparticle surfactant (NPS) systems and the resulting liquid construct with a solid-like behavior.

Liquid Construct	**Nanoparticle(s)**	**Surfactant(s)**	**Remarks**	**Ref.**
Filamentous GO threads	GO	POSS-NH_2	Liquid-in-liquid printing and streaming of aqueous GO ink into the silicone oil containing POSS-NH_2. In this work, the electrostatic interaction between the deprotonated carboxylic acid groups of graphene oxide (GO) and the protonated amine groups of POSS-NH_2 leads to the formation of nanoparticles at the liquid-liquid interface.	[54]
Filamentous GO threads	GO	POSS-NH_2	Streaming of GO ink into the hexane containing POSS-NH_2.	[55]
Filamentous emulsion GO threads	GO	POSS-NH_2	Streaming of GO emulsion (O/W emulsion upon mixing hexane-enriched POSS-NH_2 with an aqueous phase containing GO) into the hexane-POSS-NH_2.	[55]
Filamentous GO threads	GO	POSS-NH_2	Streaming of GO ink into the POSS-NH_2 enriched hexane, pentane, or toluene.	[40]
Filamentous GO:mGO threads	GO:mGO, 1:1 weight ratio	POSS-NH_2	Streaming of hybrid magnetic GO:mGO ink (1:1 weight ratio) into the hexane-POSS-NH_2.	[40]
Filamentous GO threads	GO	POSS-NH_2	Streaming of GO ink into the hexane-POSS-NH_2.	[19]
Filamentous GO:MXene threads	GO:MXene	POSS-NH_2	Streaming of hybrid GO:MXene ink into the hexane-POSS-NH_2. The weight ratios of GO:MXene are 1:1 and 0.2:0.8.	[19]
MXene beads	MXene	POSS-NH_2	Generating MXene liquid beads upon extruding 50 or 80 wt% MXene suspension into the hexane-POSS-NH_2; the liquid beads form as a result of liquid stream break-up into discrete droplets.	[19]
Filamentous Janus threads of GO:MXene/GO:mGO	Side1:GO:MXene, 0.2:0.8 weight ratio. Side 2:GO:mGO 1:1 weight ratio	POSS-NH_2	Streaming conductive and magnetic Janus liquid threads composed upon integration of two streams, including side 1: GO:MXene with 0.2:0.8 weight ratio and side 2: GO:mGO with 1:1 weight ratio.	[3]
Filamentous Janus threads of GO:MXene/GO	Side1:GO:MXene 0.2:0.8 weight ratio Side 2:GO	POSS-NH_2	Streaming conductive and non-magnetic (non-responsive) Janus liquid threads composed upon integration of two streams, including side 1: GO:MXene with 0.2:0.8 weight ratio and side 2: GO	[3]

Filamentous GO:CNF threads	GO:CNF 1:1 weight ratio	POSS-NH_2	A GO:CNF ink with a 1:1 weight ratio was streamed into a nonpolar domain containing hexane and POSS-NH_2.	[56]
Reconfigurable liquid structure of silica and CNC NPs	Carboxylated silica, Carboxylated CNC	PDMS-NH_2	Liquid-in-liquid printing of aqueous suspension of carboxylated silica or CNC nanoparticles in the PDMS-NH_2 enriched silicone oil, leading to reconfigurable and stimuli-responsive (pH-responsive) liquid structures.	[6]
Nanocaly liquid constructs	Nanoclay	PDMS-NH_2	Streaming or liquid-in-liquid printing of nanoclay suspension into the PDMS-NH_2 enriched silicone oil, toluene, or hexadecane.	[10]
Conductive PEDOT:PSS liquid constructs	PEDOT:PSS	PDMS-NH_2	3D liquid-in-liquid printing of PEDOT:PSS ink into the PDMS-NH_2 enriched silicone oil.	[57]
UV curable PEDOT:PSS liquid constructs	PEDOT:PSS plus PEG-DA	PDMS-NH_2	Liquid-in-liquid printing of PEDOT:PSS ink with PEG-DA accompanied with a photo-curable component into the PDMS-NH_2 enriched silicone oil.	[57]
CNC liquid letters	CNC-OSO_3^-	PS-NH_2	Generation of the liquid letter upon interfacial complexation between the deprotonated CNC-OSO_3^- and protonated PS-NH_2.	[9]
Filamentous CNC liquid constructs	CNC	PS-NH_2	Streaming of CNC aqueous dispersion into the toluene containing PS-NH_2, forming CNC liquid threads.	[58]
Liquid tubules or beads based on silica nanoparticles	Carboxylated silica	PDMS-NH_2	Formation of tubules or bead-shaped liquids upon extruding aqueous dispersion of carboxylated silica nanoparticles into toluene-enriched PDMS-NH_2.	[59]
Pickering emulsion gel	Carboxylated silica	PDMS-NH_2	Formation of Pickering emulsion gel upon electrostatic interaction of carboxylated nanoparticles dispersed in the aqueous phase with α, ω-diamino functionalized polymers in the oil phase. The complexation happens at the oil/water interface.	[39]
3D printable GO/MXene emulsion gel	GO and MXene	ODA	Formation of emulsion upon electrostatic interaction between the GO and MXene dispersed in the water phase and ODA in the oil phase (toluene), improving the viscoelastic character of the ink and allowing direct ink writing.	[38]
3D printable hybrid GO emulsion gel	GO, CNC, or nanoclay	DDAB	Formation of 3D printable emulsion ink upon interfacial complexation between the negatively charged nanoparticles dispersed in the aqueous phase and DDAB in the oil phase.	[60]
Interfacially complexed Bijel arrangement	Silica nanoparticles	PDMS-NH_2	Formation of Bijel upon mixing aqueous dispersion of silica nanoparticles and toluene containing two different molecular weights of PDMS-NH_2 (1000 and 3000 g/mol).	[11]

A complete list of used abbreviations in this table is provided in Table S1 within the supporting information.

3.2 From nanoparticle surfactants to macroscale structured liquids

3.2.1 Structured Pickering emulsions and emulgels

The Pickering emulsion is known as a type of emulsion in which its stabilization passes through the adsorption of colloidal particles at the interface of two immiscible phases.[61] The Pickering emulsion can be either water-in-oil (w/o) or oil-in-water (o/w) types based on the wettability of the particles. This can be described according to the contact angle of a solid particle at the oil/water interface.[62, 63] In emulsion systems stabilized by solid particles, typically, one liquid wets the particles more thoroughly than the other, causing the less wetting liquid to become the dispersed phase. Accordingly, if the contact angle measured through the water phase becomes less than <90°, the particles are more hydrophilic, stabilizing the o/w emulsion systems. In contrast, at contact angles more than >90° where the particles are hydrophobic, the w/o emulsion will be stabilized.[64, 65]

Interestingly, employing the art of interfacial complexation in the Pickering emulsions provides the opportunity to stabilize the emulsion through the jamming of nanoparticles at the interface of two immiscible liquids. Additionally, structured emulsions facilitate the tailoring of viscoelastic properties and microstructures, enabling the creation of structured emulgels suitable for use in additive manufacturing.[38, 39, 60] In this regard, attractive Pickering emulsion gels (APEGs) were obtained via electrostatic interactions between the nanoparticles stabilizing the water droplets and a telechelic polymer within the oil phase.[39] In this approach, the water droplets are covered via negatively charged nanoparticles, i.e., carboxylic acid functionalized nanoparticles, providing active sites for electrostatic interaction with the positively charged telechelic polymeric ligands. Similar to typical NPS assemblies, this interaction is also based on the ammonium-carboxylated electrostatic interactions, in which telechelic polymeric ligands with two -NH_2 ends interact with two negatively charged nanoparticles in two neighboring aqueous droplets, bridging these droplets and facilitating the formation of APEGs (Figure 2). In such a system, the type of nanoparticles, oil phase, and telechelic polysemic ligands are customizable, providing a pathway to engineering the composition of APEGs on demand. Importantly, such a jammed system induces a strong viscoelastic and shear-thinning character, enabling the direct ink writing of the APEGs to yield customized 3D structures in the air or even under water. Of note, the rheological properties of APEGs can also be tuned by the molecular weight of the telechelic polymeric ligand, pH, and temperature, providing several opportunities for designing functional materials with controllable composition and rheological characteristics.

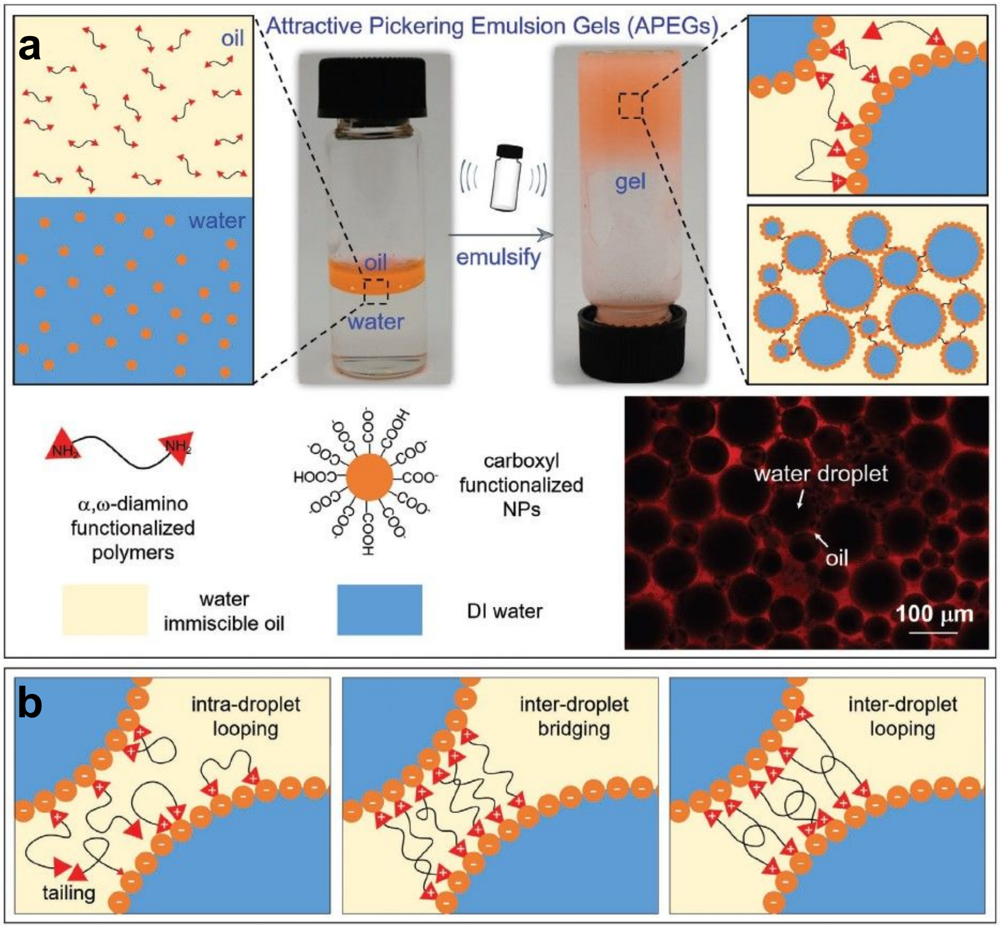

Figure 2: (a) Formation of Pickering emulsion gel through the electrostatic interaction between the carboxylic acid functionalized nanoparticles in the aqueous phase and the α, ω-diamino functionalized polymer as the colloidal surfactant in the oil phase; the displayed confocal microscopy image showcases the formation of Pickering emulsion gel in which the oil phase is stained with Nile Red. (b) Interfacial assembly and formation of Pickering emulsion gel through the electrostatic interaction between the negatively charged nanoparticles and polymeric surfactant at the oil/water interface, starting from tailing and intra-droplet looping to inter-droplet bridging and looping. (a-b) Reproduced with permission.[39] Copyright 2018, Wiley-VCH.

In another study, Zhang et al.[60] developed viscoelastic Pickering emulsion gel through NPSs jamming at the interface. The formed Pickering emulsion gel consisted of negatively charged nanoparticles dispersed within the aqueous phase, i.e., cellulose nanofiber (CNF), graphene oxide (GO), and nanoclay (laponite), and didodecyldimethylammonium bromide (DDAB) as the ligand dispersed within the oil phase.[60] The electrostatic interaction between the nanoparticles and ligands at the interface formed stable Pickering emulgels that stabilized the oil droplets within the continuous phase. In this system, the jamming of nanoparticles such as GO restricted the droplets and led to an increase in the viscosity and stiffness of the emulsion gel, leading to ideal printability. This also provides the possibility of homogeneous hybridization of non-water soluble and water-soluble nanoparticles at each respective oil and water phase, allowing for the customized composition and flexibility of design (Figure 3a). It was evident that the GO stacking at the interface through jamming could improve the viscoelastic properties of the dispersions.[66, 67] Upon an increase in the concentration of GO to more than 1 wt%, short distances among the GO flakes promote their interactions, which are mainly based on hydrogen bonding, limiting their movement and mobility. This could also be accompanied by the steric hindrance of large GO flakes that restrict their movement upon jamming at the interface.[67, 68] The jamming of the nanoparticles substantially reduces the spacing between the droplets, limiting their ability to deform and move. This restriction enhances the viscosity and stiffness of the emulgels, thereby improving their printability.

In contrast to Pickering emulgels, which are designed using classical surfactants without interfacial jamming, NPSs formed through electrostatic interactions between nanoparticles in the aqueous phase and ligands in the oil phase can stabilize emulsion systems more effectively. This enhanced stability arises from the significantly higher binding energy of NPSs to the interface compared to classical surfactants, thereby preventing droplet coalescence in emulsion systems. In this regard, Li et al.[38] employed the art of interfacial complexation to yield 3D printable GO/MXene emulsion gel inks at low nanoparticle concentrations. The system is composed of low concentrations of GO (2.8 mg cm^{-3}) and MXene (4.1 mg cm^{-3}) in the aqueous phase, electrostatically interacting with the octadecyl amine (ODA) as the ligand in the oil phase (toluene), forming sheet-like NPS assemblies at the interface (Figure 3b). In this system, the anchored ligand interactions among droplets dictate the rheological characteristic of the system, allowing a gel-like behavior with required viscoelastic properties toward direct ink writing at low 2D nanomaterials concentration. This happens upon reduction in the interfacial tension by electrostatic interactions between the nanoparticles and ligands at the interface, their subsequent jamming, and minimizing the interfacial area of the emulsion droplets.[69, 70] This locks in the shape of the droplets within the continuous aqueous phase and forms stable emulsion gel with ideal viscoelastic behavior toward additive manufacturing. It is worth noting that the interfacial assembly of 2D GO and MXene and the viscoelastic characteristics of the resulting emulsion gel are spurred by a substantial reduction in Helmholtz free energy, which is contingent upon the geometry and shape of these nanoparticles.[41] This suggests that a broader array of 2D nanomaterials, such as MoS_2 or boron nitride, could potentially be employed to create emulsion gel systems in the future.

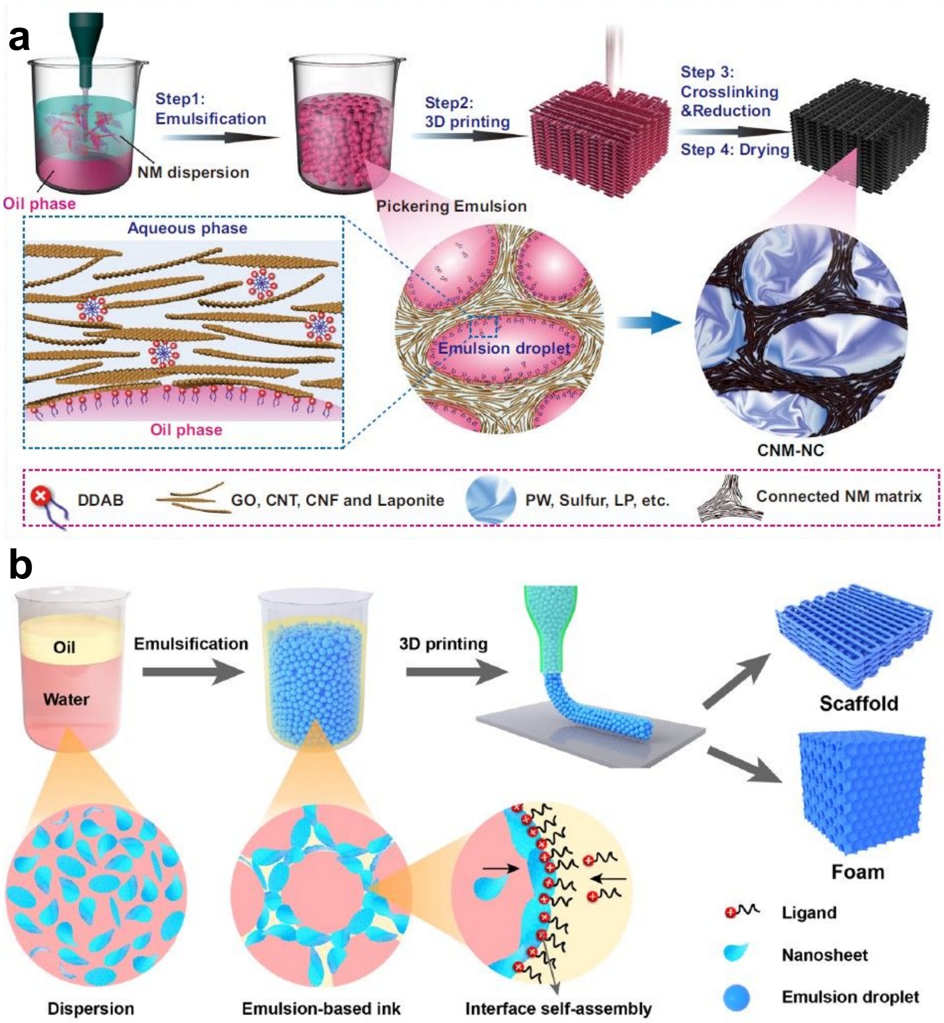

Figure 3: (a) From the formation of Pickering emulsion gel to 3D printing; step 1) emulsification of the aqueous phase containing nanoparticles and the oil phase containing ligand via homogenizer leading to Pickering emulsion gel formation; the jammed emulsion system provides the possibility to tune the viscoelastic character of the ink toward direct ink writing. Step 2) 3D printing of the jammed emulsion gel, controlling the spatial arrangement of 3D constructs. Step 3) crosslinking and reduction, and step 4) drying to yield a 3D structured construct with the ability to add water soluble and non-soluble nanoparticles in each water and oil phase, respectively. (a) Reproduced with permission.[60] Copyright 2021, Nature Publishing Group. (b) Formation of emulsion gel through interfacial complexation of MXene/GO and octadecyl amine

as the ligand, enabling direct ink writing and 3D structural design. The jamming process allows tuning the rheological and viscoelastic characteristics of the ink toward 3D printing. (b) Reproduced with permission.[38] Copyright 2022, American Chemical Society.

3.2.2 All-liquid molding

The robust NPS assemblies also provide a versatile and simple approach for the fabrication of 3D-shaped all-liquid molded constructs.[9] In this method, adaptive and stimuli-responsive all-liquid structures are fabricated through molding and density-driven extraction of the formed liquid construct from the mold, in which the shape and details of the mold are preserved on the formed liquid objects. The sculpted liquid construct retains all the inherent characteristics of the constituent nanoparticles and preserves its 3D shape like a solid object, showcasing the potential of NPS in driving the liquid structures from liquid-like to solid-like behavior on demand. Notably, the approach enables a wide range of material selection for advanced functions and designs, providing a lot of opportunities for the next generation of smart soft materials.

Importantly, from the technical perspective, the formation of all-liquid molded constructs is quite challenging due to several crucial criteria: 1) the binding energy that preserves the NPS assemblies at the interface must be high enough to retain their integrity, 2) the NPS assemblies formation must be faster than any relaxation of fluids, avoiding their deformation into equilibrium droplets, 3) the disordered interfacially driven elastic film generated from the jamming of NPS assemblies must be strong enough to suppress the instabilities during the removal of structured liquids from the mold and maintain the integrity of the liquid construct in a non-equilibrium form.[1, 9] These criteria were satisfied through the prompt and strong binding of the cellulose nanocrystals (CNCs) with amine-terminated polystyrene (PS-NH_2) at the oil/water interface, forming robust interfacially driven assemblies of cellulose nanocrystal surfactants (CNCSs).[58] The turning point of CNCSs is their rapid and strong binding to the oil/water interface that could overcome the instabilities and retain the structural integrity of the liquid structures, paving the way for precisely designed 3D-structured all-liquid constructs.[9]

The all-liquid molding process starts from the placement of the CNC suspension into a predesigned mold, prewetted with an oil solution containing an amine-terminated polymeric ligand (Figure 4a). Upon immersing the mold in the oil solution containing amine-terminated ligands, CNCSs rapidly form at the exposed interfaces, and the sculpted liquid constructs will be extracted from the mold because of the oil's higher density than the aqueous phase. Upon the extraction of the sculpted liquid construct from the mold, a decrease in the interfacial area will be initiated upon jamming of CNCSs assemblies at the interface, arresting the non-equilibrium shape of the molded liquid structure indefinitely.

The electrostatic interaction of CNC and PS-NH_2 ligand is pH-driven and occurs as a result of the complexation of the deprotonated sulfate group ($-OSO_3^-$, pK$_a$ of ≈ 1.9) of CNC and protonated amine group ($-NH_3^+$, pK$_a$ of ≈ 9.0) of PS-NH_2, leading to disordered CNCSs assemblies at the interface and a dramatic decline in the interfacial tension. Accordingly, altering the pH of the medium can significantly affect the surface coverage of CNCSs assemblies, with higher surface coverage and structural stability at pH~3 (Figures 4b-c). This enables reconfigurable all-liquid molded soft materials with ideal structural integrity and fidelity, e.g., complex geometries of alphabets with inherent mechanical robustness of NPS assemblies (Figure 4d). Furthermore, the shape of the sculpted liquid objects can be altered via external stimuli by applying an electric field, external force, shear force, and varying the medium's pH, [9] holding a great promise for developing smart and stimuli-responsive soft materials.

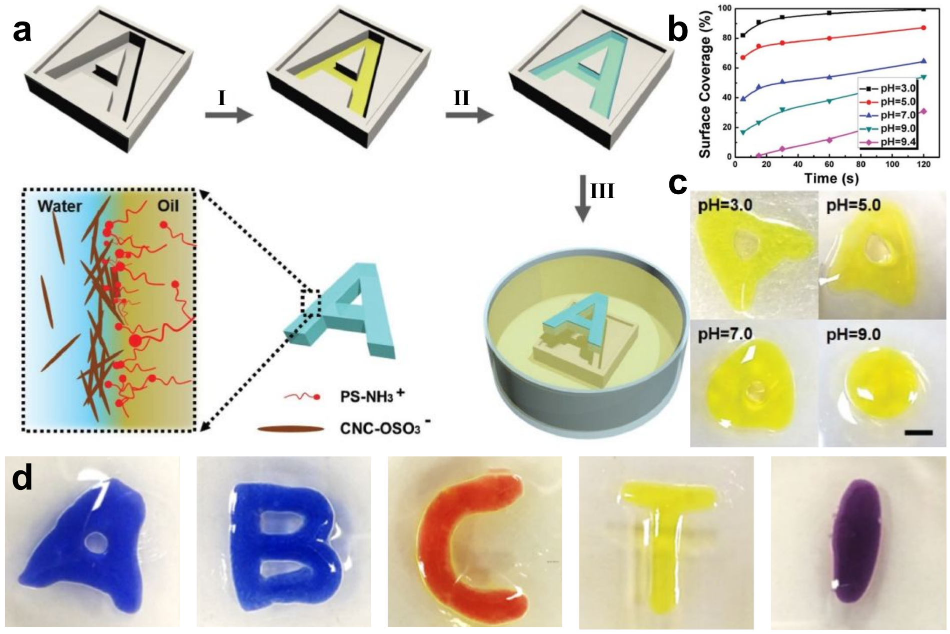

Figure 4: (a) The process of all-liquid molding, starting from (I) prewetting the mold with oil/ligand solution and placement of the CNC suspension in the mold. (II) Immersion of the mold into the oil/ligand solution and (III) its subsequent density-driven extraction from the mold. (b) Surface coverage of the CNCSs assemblies altered via the variation of pH. (c) Effect of pH on the shape fidelity of the molded liquid constructs, and (d) formation of molded liquid structured alphabets via the liquid molding strategy. (a-d) Reproduced with permission.[9] Copyright 2018, Wiley-VCH.

3.2.3 Liquid streaming and 3D liquid-in-liquid printing

Liquid streaming is a versatile method where a jet of one liquid within another immiscible liquid is stabilized by interfacial jamming of NPSs, leading to the formation of tubular or worm-like liquid threads.[11, 18, 53] To understand the potential of this approach, it is essential to explore what happens when a liquid stream is introduced into another immiscible domain, a phenomenon often elucidated by Plateau-Rayleigh instabilities. Upon streaming an aqueous liquid jet into a secondary immiscible liquid, the stream elongates and undergoes radius reduction after a specific distance. The jet's elongation increases the surface area relative to volume, triggering periodic oscillations in the jet's diameter and the formation of curvature sites with concave and convex shapes. This causes an internal flux from areas with higher imposed pressure (concave area) to lower-pressure sites (convex area). This pressure gradient-induced flux declines the surface area on concave sites and promotes the applied pressures and interfacial tension. As a result, the liquid stream breaks down into discrete droplets from these concave sites to overcome instabilities and reach an equilibrium by lowering the energy state.[40, 71] As a result, a jetted liquid within another immiscible liquid domain has been unable to produce filamentous structures or be used for 3D structural design via liquid-in-liquid printing. However, this limitation has recently been overcome by structuring a liquid jet through the interfacial assembly and jamming of NPSs, opening up numerous opportunities for further exploration in future studies.[71, 72]

Liquid streaming's potential was recently showcased through the creation of structured liquid threads, also known as liquid worms.[40] In this approach, an aqueous suspension of graphene oxide (GO) was injected into a nonpolar domain containing hexane and aminopropylsobutyl polyhedral oligomeric silsesquioxane (POSS-NH_2). The fast and pH dependant electrostatic interaction between the deprotonated carboxylic acid functional groups of GO ($-COO^-$, pKa $\approx$ 4.2) and the protonated amine group of (POSS-NH_2) ($-NH_3^+$, pKa $\approx$ 9.0) was reported to stabilize the falling stream of GO in a nonpolar domain through suppressing the Plateau-Rayleigh instabilities (Figures 5a-c).[40]

It is important to highlight that to efficiently produce these tubular all-liquid structures, the speed of NPSs formation, assembly, and jamming needs to surpass the relaxation rate of fluids. Additionally, their binding energy must be sufficiently high to offer mechanical stability to the tubular liquid structures. Once these conditions are met, a nanometer-thin interfacially driven skin forms around the liquid thread. This skin consists of disordered assemblies of NPSs at the interface, reducing interfacial tension and ensuring the integrity of the non-equilibrium form of the liquid structure.[40] This development holds great promise for generating multifunctional liquid assemblies, enabling the creation of stimuli-responsive soft materials such as bicontinuous separation systems, all-liquid electronics, and biphasic reactors.[10, 11, 73, 74]

More interestingly, hybrid suspensions of GO with other nanomaterials, such as magnetic GO flakes (GO-Fe_3O_4) and 2,2,6,6-Tetramethylpiperidine-1-oxyl (TEMPO)-oxidized CNFs, were also used to develop liquid threads through the liquid streaming approach.[40] This demonstrates the potential of GO as a universal carrier for liquid streaming, where other nanomaterials can be added to the aqueous phase. Accordingly, GO facilitates the interfacial assembly, while other nanomaterials in the system impart magnetic responsiveness or additional functionalities that can be leveraged for the final applications of these constructs. This potential of GO as a universal carrier for stabilizing hybrid systems in liquid streaming stems from its dual hydrophilic/hydrophobic nature.[19, 40] It possesses hydrophilic functional groups such as carboxylic acid, hydroxyl, and epoxide functional groups, along with a hydrophobic basal plane. Consequently, GO acts as a surfactant, easily migrating to the interface and interacting with the ligand to form NPSs that subsequently stabilize the liquid streams.[19] This minimizes interfacial tension, enhances the integrity of the liquid structures, and allows for the utilization of the inherent characteristics of the nanomaterials in the final assembly to create advanced functional materials.

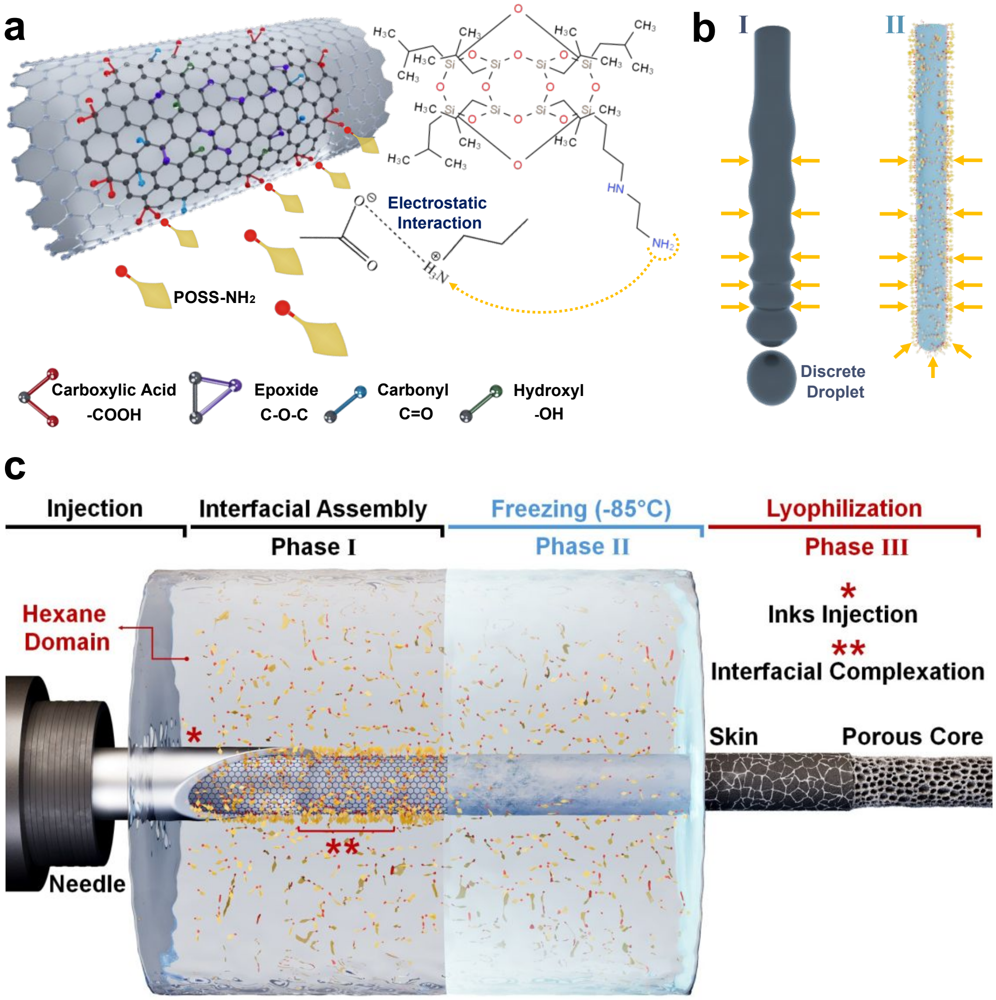

Figure 5: (a) Schematic illustration of electrostatic interaction between the deprotonated carboxylic acid functional groups of GO and the protonated amine group of POSS-NH_2, forming filamentous liquid threads by suppressing the instabilities. (b) (I) Break-up of the streamed liquid into discrete droplets to overcome the instabilities and (II) formation of filamentous liquid threads in a non-equilibrium form, stabilized through the formation of NPSs. (c) The process of "liquid streaming" starts from the injection of an aqueous ink containing custom composition/concentration of nanoparticles into a non-polar oil domain containing ligands, leading to (Phase I) interfacial complexation and formation of liquid threads, generating 3D structured multi-scale porous constructs upon (Phase II) ultra low-temperature freezing (-85°C) and (Phase III) lyophilization, yielding core-shell filamentous threads composed of a porous core

surrounded by a thin interfacially driven skin. (a-c) Reproduced with permission.[40] Copyright 2018, Wiley-VCH.

In another study, researchers explored the potential of co-assembling GO and MXene (specifically, $Ti_3C_2T_x$) at the interface to create conductive tubular liquid worm-shaped threads (Figure 6a).[19] $Ti_3C_2T_x$ on its own cannot generate liquid streams; instead, it breaks up into discrete droplets when its aqueous dispersion is injected into the hexane-POSS-NH_2 domain. It is worth noting that $Ti_3C_2T_x$ flakes are negatively charged and possess various negative moieties like -O, -F, and -OH, which interact with the protonated amine groups of POSS-NH_2, leading to overlapping assemblies that jam at the interface.[75] However, these assemblies are not robust enough to maintain the non-equilibrium shape of liquid threads and end up breaking into discrete droplets. In contrast, when GO and $Ti_3C_2T_x$ are co-assembled at the interface, GO rapidly and robustly assembles at the interface, forming a strong hybrid assembly with MXene and POSS-NH_2. This hybrid assembly can withstand applied compressive loads and maintain the integrity of the construct. This development is particularly practical for producing electrically conductive multi-scale porous aerogels through freezing and lyophilization of the formed liquid structures, offering potent electromagnetic interference (EMI) shielding capabilities.

On the other hand, harnessing the potential of Plateau–Rayleigh instabilities in pure aqueous streams of MXenes allows for the creation of structured liquid beads (Figures S2a-d).[19] When introducing the $Ti_3C_2T_x$ stream into the hexane-POSS-NH_2 domain, the stream eventually breaks down into liquid droplets, forming MXene liquid beads after a certain distance. This is because the formed MXene NPS assemblies cannot adequately suppress the instabilities and the compressive loads imposed on the filaments.[76-78] However, the developed liquid beads were structured with a solid skin of NPS around the bulk of the constructs (Figure S1a). As a result, these liquid beads remained completely stable after streaming and did not merge even under constant shaking or aging. Thanks to the distinctive stability of liquid beads, the constructs developed were used as a liquid template to create conductive aerogel beads. These beads are characterized by their ultra-low density and are mechanically strengthened by a solid skin formed through liquid streaming and NPSs assemblies (Figures S1e-g).

In another study, Janus filamentous liquids were developed based on the concept of liquid streaming (Figures 6b-e).[3] These Janus structures, characterized by an anisotropic distribution of custom nanomaterials at opposite faces, are formed through the integration of two liquid streams within the hexane/ligand domain. The resulting liquid construct consists of two distinct sides, each housing a controllable composition and concentration of nanoparticles. This dual-sided composition allows for the utilization of the inherent characteristics of nanoparticles on each side, enabling on-demand responsiveness at independent sides of the liquid streams. To achieve this, Janus liquids with conductive, non-conductive, or magnetic sides were developed by merging streams of pure GO (non-responsive), GO/$Ti_3C_2T_x$ (conductive), and GO/magnetic GO (magnetic). This method provides an opportunity to program the functionality of filamentous structured liquids, spanning from micro to macro scales, to produce smart soft materials with the desired responsiveness.

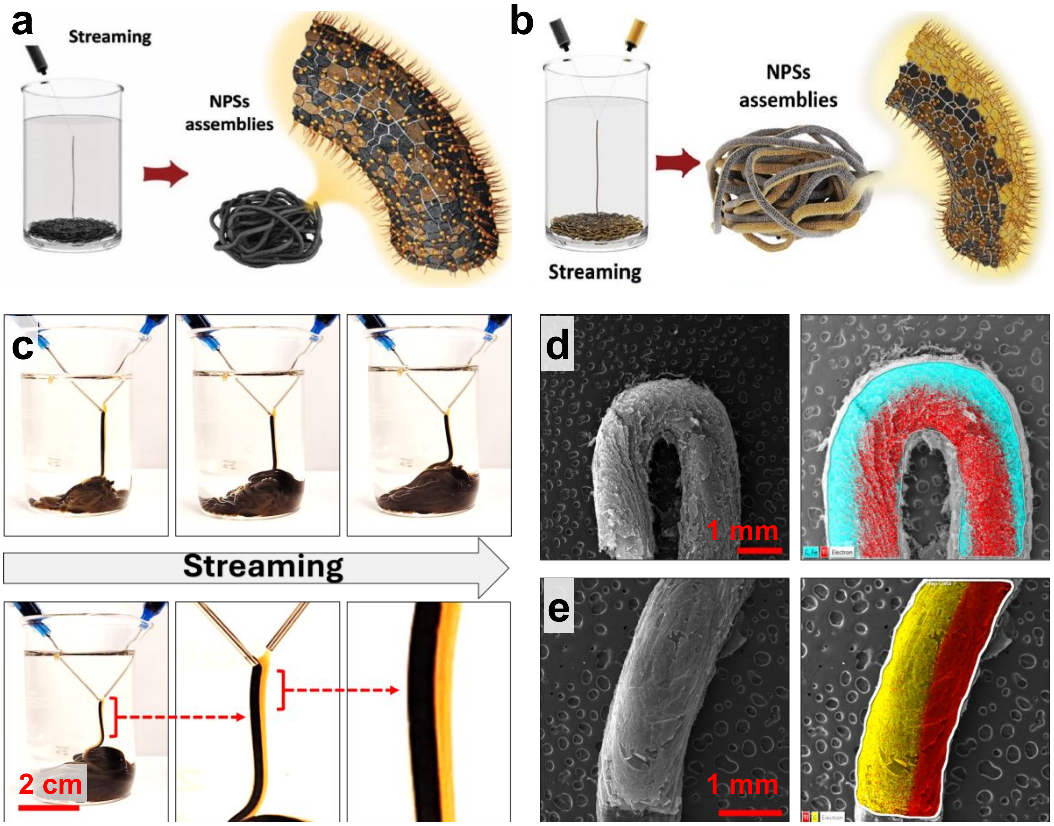

Figure 6: (a) Hybrid GO/MXene liquid streams stabilized into a non-equilibrium filamentous form upon suppressing the instabilities and imposed compressive loads; in this case, the GO promptly assembled at the interface and preserved the integrity of the liquid stream in the presence of MXene. (a) Reproduced with permission.[19] Copyright 2023, Wiley-VCH. (b) Formation of filamentous Janus liquid constructs with distinct composition/concentration of nanomaterials at opposite sides. (c) Janus structures with non-interfering magnetic and conductive domains were fabricated by merging streams of $Ti_3C_2T_x$/GO and GO/mGO. FESEM and EDX analysis of (d) $Ti_3C_2T_x$/GO:mGO/GO (conductive/magnetic worms) and (e) $Ti_3C_2T_x$/GO:GO Janus constructs (conductive/nonresponsive). (b-d) Reproduced with permission.[3] Copyright 2023, Nature Publishing Group.

Stabilized liquid streams have also been used in liquid-in-liquid printing to design complex all-liquid 3D geometries with on-demand chemical or structural features. [6, 41] To this end, 3D liquid-in-liquid printing of an aqueous suspension of carboxylated nanoparticles into a highly viscous silicone oil containing amphiphilic amine-terminated polymeric ligands, i.e., amine-terminated PDMS was introduced (Figure 7a).[6] Interestingly, these printed structures are responsive to their external environment, i.e., pH, possess a tunable lifetime, and exhibit a compartmentalized response to chemical cues. As a result, such a construct can be used in applications ranging from liquid electronics and biphasic reaction vessels to cell or active material encapsulation platforms.

Furthermore, reconfigurable all-liquid printed constructs have also been used to develop all-liquid microfluidic devices. In this regard, an assembly of NPSs, consisting of nanoclay and amine-functionalized polydimethylsiloxane (PDMS), was used to create 3D all-liquid fluidic devices.[10] This device features spatially programmed functions and can be infinitely reconfigured (Figure 7b). Employing 3D liquid-in-liquid printing, micropatterned 2D arrays were printed as channels for fluid flow. These channels are stabilized via a semi-permeable and anionic NPS membrane formed at the interface of liquids, allowing the on-demand chemical exchange in the system. Besides, the anionic membrane of the device can be further functionalized with small cationic molecules, nanocrystal catalysts, and enzymes for a wide range of applications. Interestingly, the device could undergo multi-step chemical transformations in the induced microchannels, allowing selective mass transportation across the assemblies at the liquid-liquid interface for task-oriented separation. These microfluidic devices can be automated using detectors, pumps, and appropriate control systems, demonstrating potential capabilities for learning and recognizing chemical logic (Figure 7c).

In another attempt, conductive structures of poly (3,4-ethylenedioxythiophene):polystyrene sulfonate (PEDOT:PSS) were fabricated through 3D liquid-in-liquid printing, where an aqueous suspension of PEDOT:PSS was injected into an oil phase containing PDMS-NH_2 as a ligand. In this process, the colloidal PEDOT:PSS particles, consisting of a hydrophobic PEDOT core with a hydrophilic shell, electrostatically interact with the protonated amine group of PDMS-NH_3^+ via the deprotonated sulfonate group R-SO_3^- of PSS upon injection into the ligand-enriched oil phase. This results in the formation of an elastic skin at the interface, which stabilizes the threads and maintains their non-equilibrium filamentous shape (Figures 7d-e). To improve the mechanical strength of these conductive liquid threads, poly(ethylene glycol) diacrylate (PEG-DA) was added to the aqueous phase and crosslinked by being irradiated under 395 nm UV light. This approach enables the creation of mechanically robust and electrically conductive liquid structures suitable for biomedical applications, as well as customizable electro-microfluidic devices designed for implanting biochips for near-field communication within living organisms.[57]

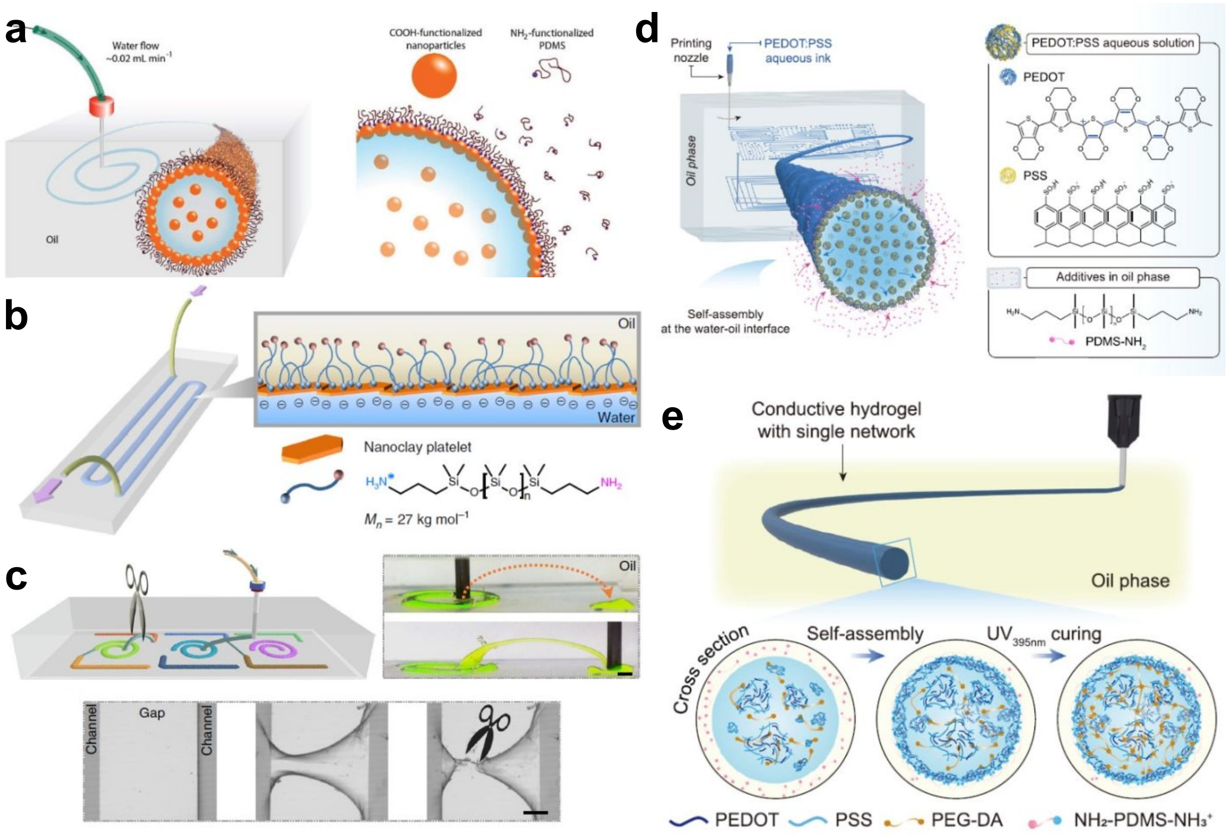

Figure 7: (a) Liquid-in-liquid printing of aqueous phases containing carboxylated nanoparticles into highly viscous silicon oil. This method generates liquid constructs with a pre-defined 3D architecture upon NPS formation and creation of an elastic film at the interface. (a) Reproduced with permission.[6] Copyright 2018, Wiley-VCH. (b) Schematic illustration of an all-fluidic device fabricated through interfacial complexation of nanoclay and polymeric surfactant, holding the integrity of the liquid constructs and allowing the flow of fluids through the channels. (c) The disconnection of microchannels in all-liquid microfluidic devices is possible by simply cutting the bridged connections. (b-c) Reproduced with permission.[10] Copyright 2019, Nature Publishing Group. (d) Liquid-in-liquid printed constructs with tunable electrical conductivity, mechanical robustness, and morphology; the 3D printed threads form upon extruding the PEDOT:PSS-based aqueous suspensions into an oil phase enriched with amine-functionalized PDMS. (e) Schematic illustration of PSS-stabilized hydrogel threads within ligand-enriched silicone oil after UV curing of the acrylatemonomer. (d-e) Reproduced with permission.[57] Copyright 2023, Nature Publishing Group.

3.2.4 Bicontinuous interfacially jammed emulsion gels (Bijels)

3.2.4.1 Principles and mechanisms related to Bijel fabrication

Bijels are non-equilibrium emulsion systems where two immiscible liquids' interpenetrating domains are stabilized through interfacial colloidal monolayers.[79, 80] The formation of Bijels was initially predicted through simulations, which suggested the possibility of generating this class of soft materials through demixing and spinodal decomposition (phase separation). This process creates interpenetrating domains of two liquids with an extensive interfacial area, forming a fluid labyrinth where each liquid phase connects one side of the sample to the other. In such a system, the interpenetrating domains of liquids are arrested in place by the adsorption of a layer of colloidal nanoparticles onto the liquid-liquid interface.

In the context of Bijels, spinodal decomposition describes the process of phase separation where two immiscible fluids naturally separate into distinct regions due to thermodynamic instability caused by changes in the chemical composition or temperature of the system. This phenomenon results in the formation of tortuous or interconnected domains of liquids, as previously discussed. However, achieving and maintaining Bijels through this mechanism pose significant challenges, requiring two key considerations: 1) The first consideration involves selecting particles that are neutrally wettable by both liquid phases, ensuring a contact angle of 90° to prevent curvature imposition on the liquid-liquid interface during phase separation. 2) The size of nanoparticles used to stabilize the complex interfaces within the Bijel domain is also crucial. Small nanoparticles (<50 nm) have lower binding energies to oil/water interfaces, especially in Bijels with low surface tensions, limiting their ability to solidify the non-equilibrium interface shapes.[81-83]

In the context of demixing and spinodal decomposition in an oil/water/surfactant system, it is crucial to determine the proportions of each component to achieve bicontinuous systems instead of forming oil-in-water or water-in-oil emulsion droplets. To accomplish this, triangular pseudo-ternary phase diagrams should be created for such systems (refer to Figure 8). These diagrams serve as technical maps that depict the emulsion's phase behavior, stability, properties, and droplet size.[84] As illustrated in Figure 8, the apex of the triangular phase diagram represents the pure component (100%), gradually decreasing to 0% as it approaches the opposite apex, where the other component is at 100%. This diagram is typically generated using the water titration method, where fixed weight ratios of the surfactant are mixed into either the oil or water phase and then added to the opposite phase at varying ratios (w/w). The resulting phase diagram provides a visual guide to observe spinodal decomposition at specific oil/water/surfactant ratios.

This observation helps determine the likelihood, type, and characteristics of the emulsions formed at different compositions of oil/water/surfactant.[84, 85]

As illustrated in Figure 8, the triangular phase diagram delineates several distinct regions: Side A represents a water/surfactant binary system, indicating the likelihood of oil-in-water (O/W) emulsion formation due to an abundance of water and limited concentrations of oil and surfactant. This configuration results in micelles with hydrophilic groups oriented outward, situated within the water phase. Side B depicts an oil/surfactant binary system, showcasing the highest probability of water-in-oil (W/O) emulsion formation. Here, reverse micelles with hydrophobic groups positioned outward within the oil phase are predominant. Side C illustrates the water and oil binary system with minimal surfactant content, leading to the presence of multiple phases with decreased stability. The upper apex corresponds to the maximum surfactant concentration and minimal water or oil content, resulting in surfactant molecules adopting a lamellar morphology to prevent emulsion formation. Finally, the bicontinuous phase represents the desired region for Bijels, where a bicontinuous structure will form, characterized by interpenetrating domains of both water and oil phases. These delineations offer insights into the phase behavior and emulsion formation tendencies within the oil/water/surfactant system, aiding in the design and understanding of complex emulsion structures.[84, 86]

With this brief introduction to Bijels in mind, the following sections explore experimental evidence regarding Bijels. We will also discuss the concept of Bijel formation using the solvent transfer-induced phase separation (STRIPS) method. Finally, we will explain how NPSs assembly and jamming can contribute to Bijel fabrication.

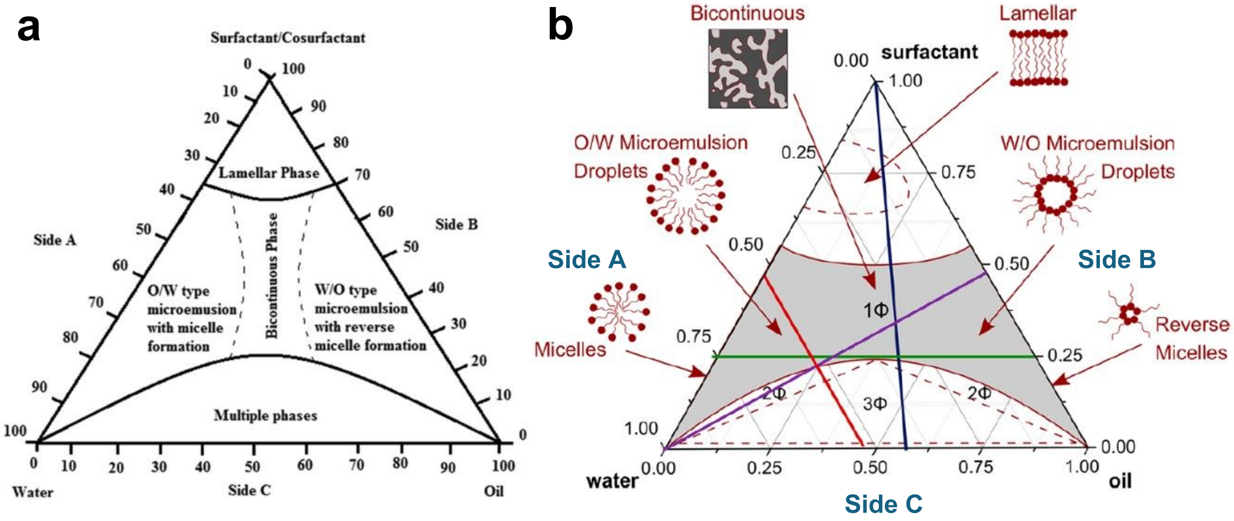

Figure 8: (a) Schematic illustration of ternary phase diagram showcasing diverse emulsion states. (a) Reproduced with permission.[84] Copyright 2021, Elsevier. (b) According to the ternary phase diagram, adjusting the relative concentrations of oil, water, and surfactant can result in the formation of various systems, including oil-in-water (O/W), water-in-oil (W/O), or bicontinuous emulsions. (b) Reproduced with permission.[86] Copyright 2021, American Chemical Society.

3.2.4.2 Experimental evidence concerning Bijels

To date, numerous experimental methodologies have been developed to create Bijels, primarily using partially miscible liquids such as 2,6-lutidine and water. These liquids can form a bicontinuous arrangement upon quenching, leading to phase separation through spinodal decomposition.[87-92] For instance, Herzin et al.[87] introduced Bijel production using a critical 2,6-lutidine/water mixture, where colloidal particles stabilized the interfaces within the system. In this case, the spinodal decomposition occurs upon heating, and the bicontinuous arrangement was locked in through the jamming of colloidal silica nanoparticles with neutral wettability at the interface. Specifically, their approach involved adding 2 wt% silica colloidal nanoparticles to the critical 2,6-lutidine/water system and heating the system to 34.1 °C to form well-defined Bijels.

Another study employed aluminum-coated silica (AlO-SiO) nanoparticles to stabilize the same 2,6-lutidine/water Bijel system, resulting in free-standing bicontinuous monoliths of AlO-SiO nanoparticles with meso- and macroporosity, coupled with the mechanical robustness of the stabilized nanoparticles network (Figure S3).[88] This innovative system offered a scalable, template- and binder-free method for generating co-continuous emulsion systems, paving the way for the production of materials ideal for separation, storage, or catalytic applications.

In another study, an alternative approach to generating lutidine-based Bijels was introduced using the solvent segregation-driven gel (seedGel) method.[89] This method is effective for developing bicontinuous assemblies with excellent reproducibility, structural thermal reversibility, adjustable transition temperature, and impressive optical properties. The system utilizes the critical water/2,6-lutidine system and incorporates spherical silica nanoparticles with an average diameter of 27 nm, characterized by a high surface charge and preferential wetting with water. The solvent ratio was meticulously set near the critical point, consisting of 71.6% water and 28.4% 2,6-lutidine, with a particle volume fraction of 24.3%. This composition leads to gel formation at elevated temperatures, effectively arresting the bicontinuous assemblies with micrometer-scale domain sizes. In another study, Rojas and coworkers developed a renewable lutidine-based Bijel where the bicontinuous assemblies were arrested with chitin nanocrystals.[90] In their work, chitin nanocrystals aqueous suspension (0.6 wt.%) is first mixed with the organic phase at room temperature (23 °C). Then, the system was heated to 60 °C to initiate phase separation, during which chitin nanocrystals jamming occurs due to the sudden change in phase volume (Figure S4). The generated green Bijel with chitin nanocrystals allows the manufacturing of ultra-lightweight aerogels with unique macroscopic arrangement.

In addition to the 2,6-lutidine/water system, various other binary liquid combinations have also been explored for Bijel development. For instance, in a recent study, all-aqueous bicontinuous emulsions with cholesteric liquid crystal domains were formed via nanoparticle colloidal assemblies.[93] In this work, the spinodal decomposition of a dextran polymeric solution and polyethylene glycol (PEG) was controlled using CNCs. The resultant liquid crystal emulsion system exhibited a well-defined 3D percolating bicontinuous arrangement following CNC cholesteric self-assembly in the PEG domain. This research demonstrated a method for arresting the bicontinuous arrangement through intraphase trapping and nanoparticle assembly, compatible with various colloidal configurations (Figure S5).

Cai et al.[91], on the other hand, reported an interesting approach for generating Bijel through a premixing technique that contains a type of lithium salt, bis(trifluoromethane) sulfonimidelithium salt (LiTFSI). In this system, the Bijel formed by arresting the spinodal decomposition of p-xylene and ethylene carbonate, two partially miscible liquids, in the presence of LiTFSI. The non-equilibrium arrangement was stabilized using silane-modified silica nanoparticles. The obtained construct is composed of interpenetrating ionically conductive and non-conductive channels formed from xylene-rich and ethylene-carbonated-rich phases, in which one phase provides the ionic conductivity and the other one preserves the structural integrity. The resulting Bijel directly formed a composite electrolyte upon diffusion of the polystyrene into the xylene-rich phase, followed by the xylene's selective removal. Interestingly, the Bijel's structure was retained, showcasing a well-arranged bicontinuous framework composed of solid and liquid phases with a wide range of tunability (Figure S6). The existence of ionically conductive channels was proved via electrochemical impedance spectroscopy, turning the resulting Bijel into a multi-phase functional material.

3.2.4.3 Solvent transfer-induced phase separation (STRIPS)

STRIPS is a versatile approach for the fabrication of hierarchical and asymmetric Bijels with customized morphologies.[92] In this technique, phase separation or spinodal decomposition is triggered via extracting a solvent from a ternary homogenous mixture of three liquids injected into a continuous flowing liquid phase. In this system, two fully immiscible liquids co-exist with a third solvent capable of rendering the two other liquids miscible. During the injection process, the solvent that initially rendered the other two immiscible components miscible will be extracted into the flowing continuous phase, leading to phase separation.[94]

The concept of STRIPS for Bijel fabrication was first introduced by Haase et al.[92] In their study, they achieved a bicontinuous arrangement by using silica nanoparticles and cetyltrimethylammonium bromide (CTAB) to form interfacial complexes. To produce Bijel fibers using STRIPS, they developed a ternary homogeneous mixture of ethanol/diethylphthalate (DEP)/water containing silica nanoparticles that interacted with an external liquid phase, i.e., an aqueous suspension of CTAB (Figures 9a-b). In their experimental setup, they utilized a coaxial capillary system: the inner capillary tube injected the ternary mixture, while the outer capillary injected CTAB aqueous suspension (refer to Figure 9b). The continuous phase injected from the second capillary extracted ethanol from the ternary phase, inducing phase separation. Here, CTAB played a crucial role in stabilizing the nanoparticles within the ternary mixture and facilitating their jamming at the interface through electrostatic interactions, thus preserving the non-equilibrium arrangement of Bijels (refer to Figures 9c-e).

It is worth noting that the STRIPS method offers a fascinating opportunity to choose from a wide array of ternary liquid combinations and particles, enabling the continuous production of highly stable bicontinuous frameworks. Notably, Bijels formed with submicrometer domains using the STRIPS technique facilitate efficient interphase mass transport for the separation of various chemical compounds. Moreover, adjusting the concentrations of nanoparticles and surfactants allows for the modification of internal micropores and surface porosities in the resulting bicontinuous structures, ranging from micrometers to a few hundred nanometers. This versatility enables the fabrication of Bijel fibers, microparticles, and membranes with tailored morphology or porosity arrangements, leading to multifunctional assemblies (refer to Figures 9f-g). Additionally, polymerized Bijels obtained through the STRIPS approach open avenues for producing planar or hollow threads suitable for applications such as battery components, efficient filtration systems, solid catalysts, sensors, and beyond.[92]

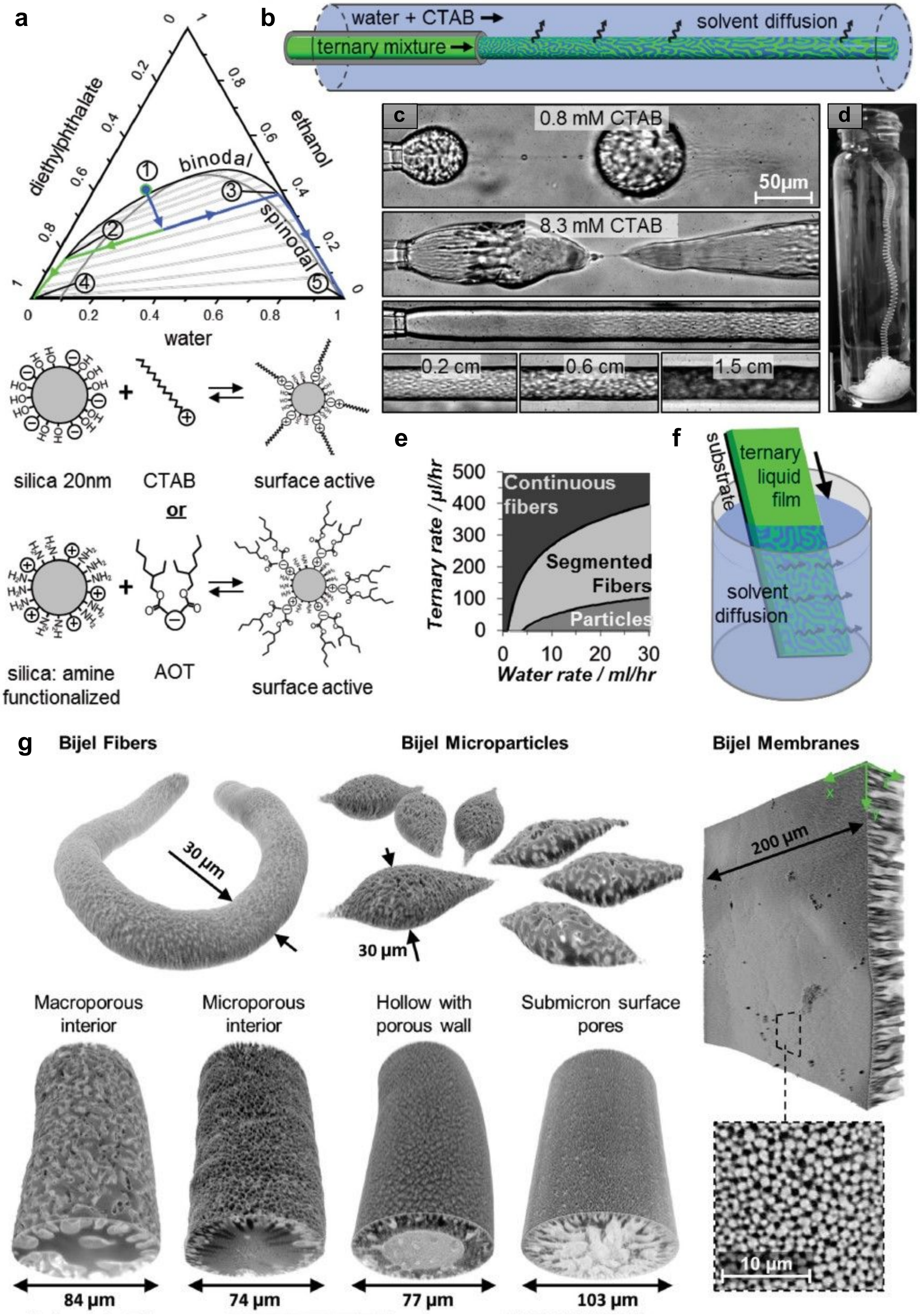
a
b
water + CTAB →
ternary mixture →
solvent diffusion
diethylphthalate
ethanol
water
binodal
spinodal
① ② ③ ④ ⑤
0 0.2 0.4 0.6 0.8 1
silica 20nm
CTAB
or
surface active
silica: amine functionalized
AOT
surface active
c
0.8 mM CTAB
50μm
8.3 mM CTAB
0.2 cm
0.6 cm
1.5 cm
d
e
Continuous fibers
Segmented Fibers
Particles
Ternary rate / μl/hr
Water rate / ml/hr
0 100 200 300 400 500
0 10 20 30
f
substrate
ternary liquid film
solvent diffusion
g
Bijel Fibers
Bijel Microparticles
Bijel Membranes
30 μm
30 μm
200 μm
Macroporous interior
Microporous interior
Hollow with porous wall
Submicron surface pores
84 μm
74 μm
77 μm
103 μm
10 μm

Figure 9: (a) The ternary phase diagram of water, ethanol, and DEP was used as a guide to adjust the concentrations of each component, enabling the formation of Bijel through the STRIPS method. This diagram also illustrates the modification of silica nanoparticles with CTAB or 3-aminopropyltrimethoxysilane functionalized with docusate sodium salt. (b) The devised capillary system was used to fabricate Bijel via the STRIPS method. In this system, a ternary mixture of liquids containing suspended nanoparticles and CTAB flows into a water stream with a pH of 3. (c) Images showcasing the fabricated Bijel microparticles and threads. (d) Digital images demonstrating the continuous formation of Bijel threads. (e) The effect of flow rate on the structure of Bijel within the capillary system is shown. (f) A schematic illustration of Bijel membrane formation, where a hydrophobic substrate coated with a thin film of CTAB and a silica-reinforced ternary mixture is immersed in a water bath. (g) The formation of asymmetric and hierarchical Bijel-based constructs is illustrated, highlighting the ability to manufacture threads, microparticles, and membranes with customizable porosities and sizes. (a-g) Reproduced with permission.[92] Copyright 2015, Wiley-VCH.

In another study, it was demonstrated that the non-equilibrium self-assembly process of nanoparticles during spinodal decomposition can be effectively controlled using the STRIPS method.[95] In this study, a ternary homogeneous mixture of water, propanol, and DEP containing silica nanoparticles and cetyltrimethylammonium cations (CTA^+) was prepared. Bijel fibers or membranes were fabricated by either flowing the mixture through an octadecyl trichlorosilane-coated glass capillary into toluene or by submerging an untreated glass slide coated with a thin film of the mixture into toluene (refer to Figures 10a-c). Interestingly, the porosity of the fabricated Bijels was controlled based on the type of alcohol used in the ternary homogeneous mixture, where the samples prepared using 1-propanol exhibited much smaller porosities compared to those prepared using 2-propanol (Figure 10d). This precise level of control enables the formation of Bijels with exceptionally small pore sizes of 300–500 nm and extensive internal surface areas. These characteristics make Bijels a powerful platform for mass transfer between two liquids, with numerous applications in catalysis, membrane separations, and energy storage/conversion devices.[95]

Aside from controllable porosities, STRIPS-driven Bijel fibers also exhibit exceptional mechanical characteristics. In this regard, we highlight a recent investigation that delves into the mechanical resilience of Bijel fibers fabricated using a microfluidic platform.[96] By analyzing the hydrodynamic stresses applied to the fibers, the range of stress that each fiber can withstand before fracturing into distinct segments has been highlighted. This fracture strength was further evaluated through comprehensive stress field analysis, revealing the potential of Bijel fibers to withstand fracture strengths exceeding several hundred Pascals, depending on the loading of nanoparticles. Such robustness makes them well-suited for diverse applications requiring varying mechanical strengths. Moreover, the segmentation of Bijels facilitated by hydrodynamic stresses enables the creation of a broad spectrum of bicontinuous structures, including continuous fibers, blobs, and rods, as illustrated in Figure S7.

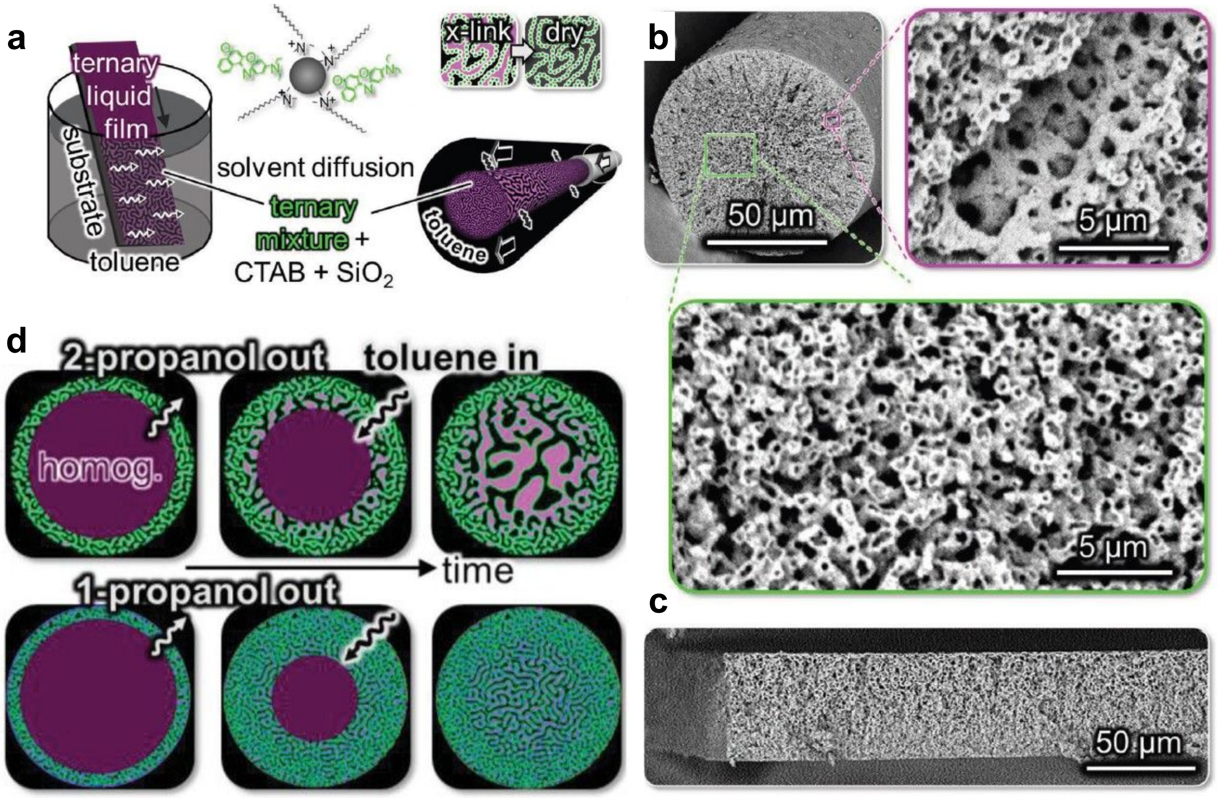

Figure 10: (a) Formation of Bijel films and fibers via STRIPS method. SEM images of a percolated pathway of silica nanoparticles scaffold in the (b) Bijel fibers and (c) free-standing films. (d) Schematic illustrations of the fiber cross-section and the proposed structure formation dynamics during STRIPS using 1-propanol and 2-propanol. (a-d) Reproduced with permission.[95] Copyright 2022, Wiley-VCH.

In another study, helical micro-ropes of Bijels were fabricated by integrating the STRIP method and microfluidic centrifugal effect.[97] The method utilizes a ternary liquid mixture consisting of 13.4% water, 44% n-butyl acrylate, and 37.2% methanol by volume. In this mixture, methanol acts as a facilitating agent, enhancing the miscibility of the otherwise immiscible components, water and n-butyl acrylate. Upon injection of the ternary liquid into a continuous flowing phase, the extraction of methanol will initiate the spinodal decomposition, which was thence arrested upon electrostatic interaction between the 4.6 vol% silica nanoparticles (20 nm diameter) and 0.8 vol%

hexadecyltrimethylammonium bromide ($C_{16}TAB$). The role of methanol is very crucial in this ternary system as it sustains the homogeneity of the liquid mixture and avoids the aggregation of silica nanoparticles because of electrostatic repulsion and the hydrophobic effect. The interaction between nanoparticles and surfactants stabilizes the non-equilibrium shape of the Bijel, enabling the formation of micro-ropes when four streams of ternary liquid are simultaneously injected and twisted using a centrifugal effect. This effect is induced by rotating a microcapillary, generating helical soft materials (Figure 11). The optimization of the coined method enabled controlling the assembly of the formed helical fibers into a well-defined micro-rope. The micro-ropes are pH-responsive, capable of swelling and shrinking in response to changes in pH. This feature opens up a range of potential applications in fields such as soft robotics, tissue engineering, sensing, and controlled release.

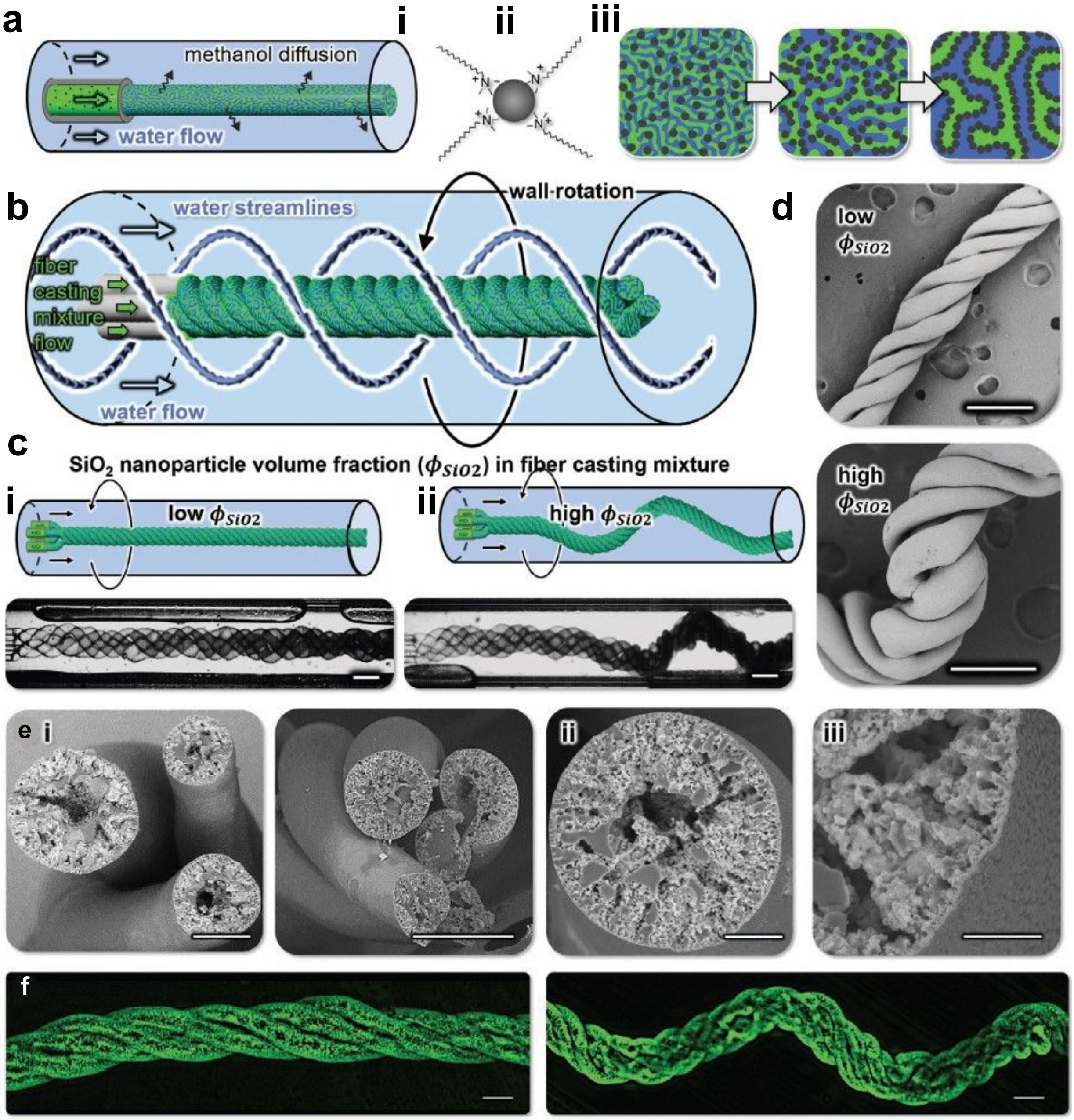

Figure 11: Microfluidically twisted Bijel threads generated via the STRIPS method; (a) (i) a schematic illustration of the capillary device used for fabrication of Bijel threads; (ii) a view of adsorbed C_{16}TAB on silica nanoparticles; (iii) water (blue) and oil (green) phase separation plus their subsequent stabilization via nanoparticles (black dots). (b) Micro-rope generation by streaming four threads into a twisting flow field. (c) Schematic illustration of micro-rope formation at (i) low and (ii) high nanoparticle loading. (d) SEM images of the formed micro-ropes; scale bars are equal to 0.2 mm. (e) SEM images from the cross-section of micro-ropes; scale bars are equal

to (i) 100 µm, (ii) 20 µm, and (iii) 10 µm. (f) Confocal images of stained micro-ropes with Nile red; scale bars are equal to 100 µm. (a-f) Reproduced with permission.[97] Copyright 2022, Wiley-VCH.

Another study enhanced the STRIPS method by introducing photopolymerization of a UV-curable monomer into a ternary liquid mixture. This modification facilitates the generation of Bijel hollow fibers, advancing the development of complex membranes.[98] Generally, enhancing a porous membrane with a dense layer of nanoparticles can improve its separation performance and resistance to folding. However, creating a membrane with a specific nanoparticle arrangement is challenging and typically requires laborious multi-step processes. By employing the STRIPS method, it is possible to streamline this into a single-step process, facilitating the production of nanoparticle-decorated hollow fibrous membranes.

In this regard, a ternary liquid system composed of water, ethanol, and hexanediol diacrylate (HDA) monomer reinforced with CTAB as the surfactant, 2-hydroxy-2-methylpropiophenone as photoinitiator, and 22-nm sized silica nanoparticles was designed.[98] Using a coaxial nozzle, a stream of water and ternary liquid is injected into the co-flowing external water stream. Ethanol extraction from the core initiated the phase separation and spinodal decomposition, which was subsequently locked by nanoparticle jamming. Upon ethanol extraction, the interaction between the silica nanoparticles and CTAB arrests the bicontinuous assemblies containing photo-curable monomers. Next, from a specifically fixed distance from the co-axial nozzle, the hollow Bijel fiber is irradiated with UV light, initiating the polymerization of the monomer and formation of a hollow solidified membrane (Figure 12a-e).

Interestingly, these hollow Bijel fibers demonstrated high resistance to organic solvents due to their crosslinked polymeric structure. Additionally, these fibers contained a significant amount of silica nanoparticles, up to 50 wt%, forming densely packed nanoparticle assemblies uniformly distributed across the membrane surface. This feature allows for the production of stimuli-responsive soft structures by controlling the membrane flux and composition. Moreover, the method's controllable nature enables the adjustment of surface porosity size from micrometers down to approximately 15 nm by varying the ethanol concentration (refer to Figures 12f-h). Consequently, this system introduces a versatile approach to fabricating advanced membranes with intricate geometries suitable for industrial separation processes, water treatment applications, or catalytic reactors.

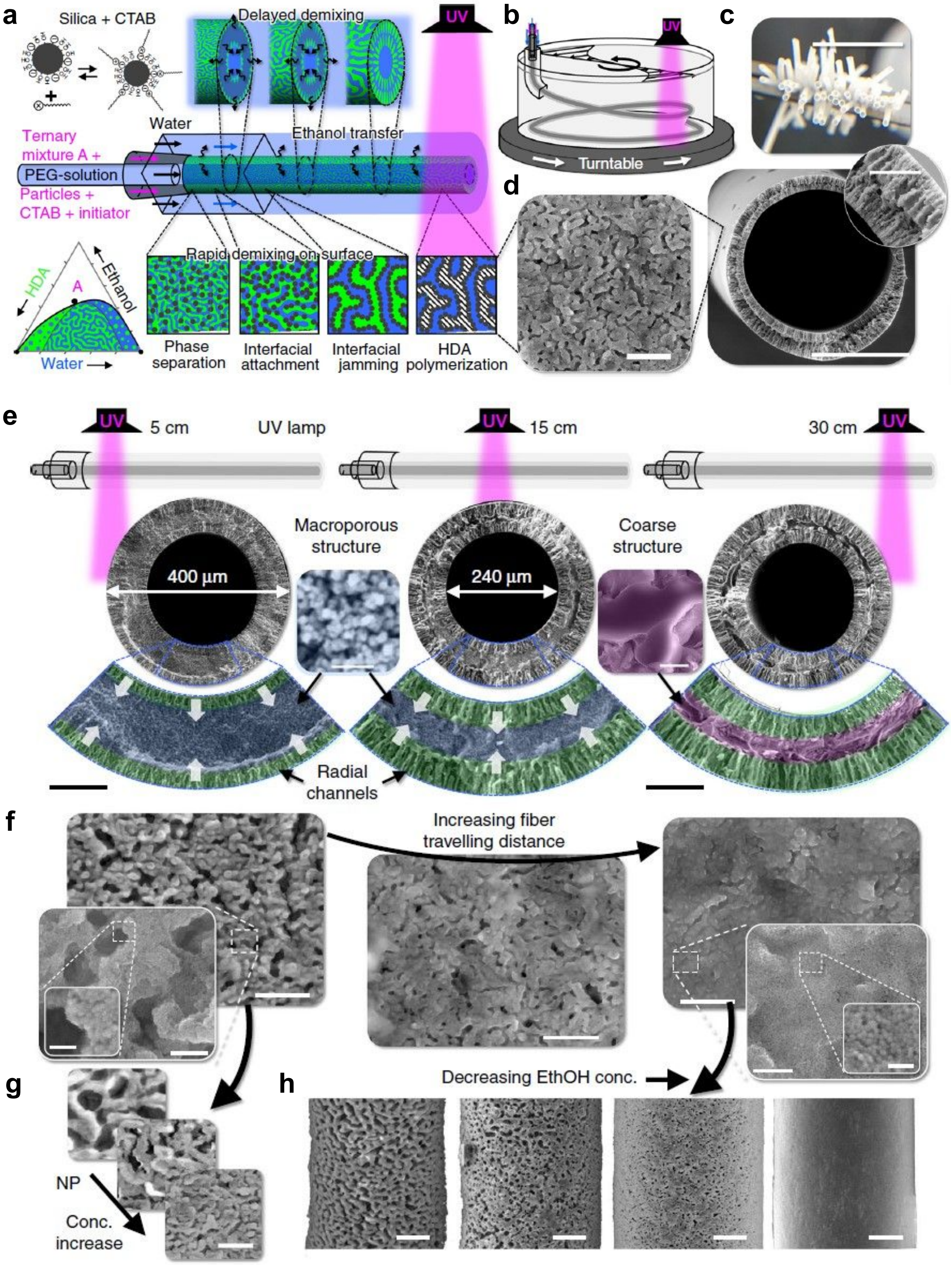
a
Silica + CTAB
Delayed demixing
UV
Water
Ternary mixture A +
PEG-solution
Particles +
CTAB + initiator
Ethanol transfer
HDA
A
Ethanol
Water
Rapid demixing on surface
Phase separation
Interfacial attachment
Interfacial jamming
HDA polymerization
b
UV
Turntable
c
d
e
UV
5 cm
UV lamp
UV
15 cm
30 cm
UV
Macroporous structure
Coarse structure
400 µm
240 µm
Radial channels
f
Increasing fiber travelling distance
g
NP
Conc. increase
h
Decreasing EthOH conc.

Figure 12: Formation of hollow fibers using the STRIPS method. (a) Schematic illustration of hollow fiber generation. Accordingly, the presence of ternary fluid containing silica nanoparticles in a doped monomer solution and the water phase containing bore and weeping fluids lead to hollow fiber formation. The jamming of nanoparticles at the interface locks in the bicontinuous liquid water/monomer scaffold, yielding hollow fiber upon irradiation with UV light. (b) Collection of formed and aligned threads in a water bath equipped with a rotating cylinder. (c) Formed hollow fibers; the scale bar is equal to 0.5 cm. (d) SEM images of the internal (scale bar: 200 µm, insert equal to 20 µm) and surface (scale bar: 5 µm) of the formed hollow fibers. (e) Controlling the morphology of fibers by changing the distance of the UV irradiation source; the black scale bars are equal to 50 µm. (f) SEM image from the surface morphology of fibers; scale bar is 5 µm, inserts 1 and 2 are 500 nm and 100 nm, respectively. (g) UV-irradiated fiber surface from a 5 cm distance containing different silica nanoparticle loadings, from top to bottom, 0.26, 0.32, and 0.38 weight of silica nanoparticles over dry fiber ($g_{silica}/g_{dry\ fiber}$) under constant 40 mM CTAB concentration. (h) Formed fiber surface as a result of different ethyl alcohol concentrations in a flowing water stream with 0.24 $g_{silica}/g_{dry\ fiber}$ at 33 mM CTAB concentration; the scale bar is equal to 20 µm. Reproduced with permission.[98] Copyright 2017, Nature Publishing Group.

3.2.4.4 NPS-based Bijels

Using NPS assemblies, Russell and co-workers developed a scalable and facile approach for generating macroscopic Bijel assemblies with a tunable internal feature size in sub-micrometer scale (<5 µm).[11] In such a system, the jammed emulsions are tortuous, showing interconnected constructs of two immiscible liquids that are kinetically arrested by colloidal nanoparticles, irreversibly bonded to the oil/water interface. Instead of spinodal decomposition, this type of Bijels with sub-micron domains can be generated via homogenization. As a result, the system arrests the bicontinuous assembly at the liquid decomposition point through electrostatic interaction between the ligand dispersed in toluene (PDMS-NH_2, with molecular weights of 1000 and 3000 g mol^{-1})

and carboxylated nanoparticles in the aqueous phase, occurring at the liquid-liquid interface. This process locks in the non-equilibrium bicontinuous toluene/water system through NPSs jamming at the interface (Figure 13). Interestingly, the coined approach is simple and scalable, capable of generating bicontinuous arrangements upon vigorous shaking of the oil/water system, where the domain size (1-10 μm), stability, and structure of the Bijels can be altered by customizing the constituent components, i.e., nanoparticles, polymeric ligand, and liquids. This shows significant potential for the development of reconfigurable bicontinuous liquids on an industrial scale, which can be reshaped as desired with an external field.

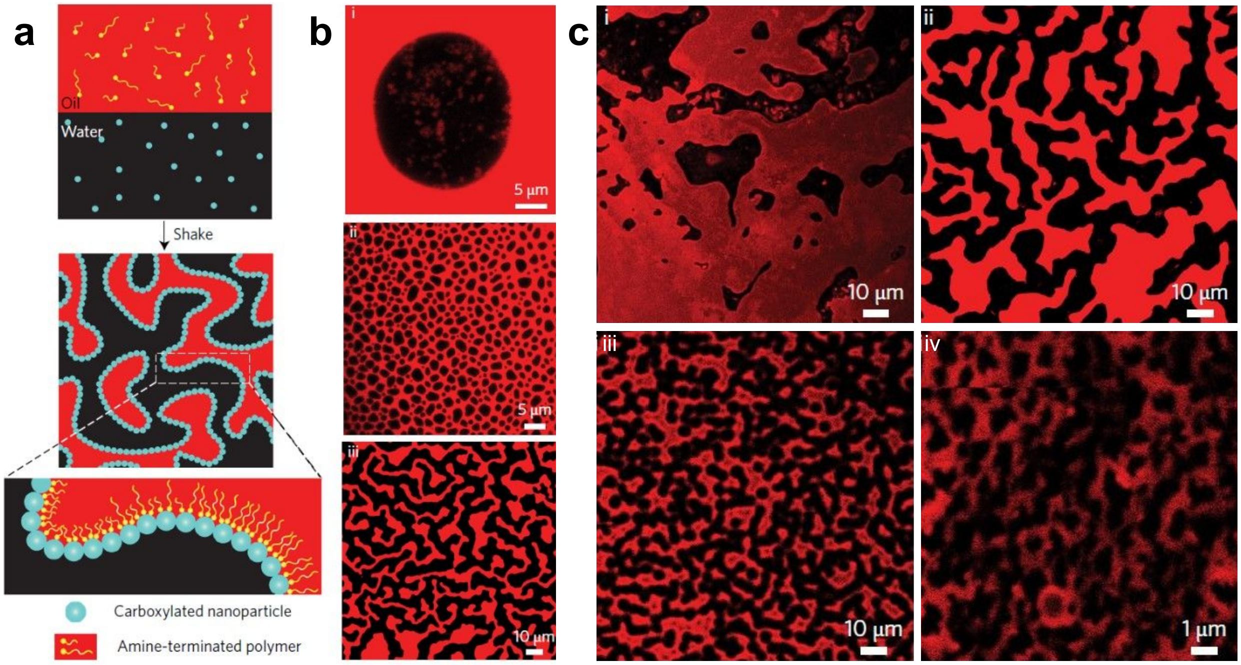

Figure 13: Bijel formation via NPS assemblies; (a) schematic illustration of Bijel formation by NPSs jamming at the oil/water interface. (b) Stabilized emulsion system based on PDMS-NH_2 dissolved in toluene with molecular weights of (i) 1000 g mol^{-1} and (ii) 3000 g mol^{-1} plus an aqueous phase containing 1 mg ml^{-1} carboxylated nanoparticles. (iii) Bicontinuous arrangement of toluene/water system arrested via NPS assemblies with equimolar PDMS-NH_2 with a molecular weight of 1000 and 3000 g mol^{-1} at nanoparticle concentration of 0.5 mg ml^{-1}. (c) Formed NPS assemblies with nanoparticle concentrations of (i) 0.1 and (ii) 0.5 mg ml^{-1} at a fixed PDMS-NH_2 concentration. Arrangement of the bicontinuous network at a fixed nanoparticle concentration of

1 mg ml^{-1} and variable PDMS-NH_2 concentrations of (iii) 0.161 and (iv) 16.1 mmol L^{-1}. As can be seen, a change in the nanoparticle or ligand concentration can significantly affect Bijel's arrangement. (a-c) Reproduced with permission.[11] Copyright 2017, Nature Publishing Group.

3.3 Structuring liquids through interfacial supramolecular assemblies

Supramolecular assembly presents an innovative approach to liquid structuring, moving beyond other methods like nanoparticle assembly that depend on only electrostatic or host-guest interactions.[12, 99] This method involves forming a network at the interface, with the distinct benefit of creating an interfacial assembly that can resist both compression and expansion—capabilities not possible with NPS-structured liquids.[2, 24] The dynamic nature of the network's junction points, which can break and reform, enables the formation of stress-free interfacial assemblies, allowing the structured liquid to be expanded. In general, these dynamic and interfacially driven assemblies rely on a diverse range of non-covalent interactions, including hydrogen bonding, hydrophobic interactions, and π-π stacking, which are important to emphasize in this review.[100] These interactions are foundational to the construction and stabilization of liquids, enabling them to be engineered with enhanced mechanical properties and stability.[101-104]

To elucidate the behavior of liquids structured by supramolecular materials, an analogy with a puzzle is shown in Figure 14. Here, the pieces of the puzzle, which interlock on a plane via a "lock and key" mechanism (mimicking intermolecular interactions), represent supramolecular materials (Figure 14a). In this scenario, the interconnected network of supramolecular materials can resist external forces and induce structural stabilities similar to those of solids, just like a complete puzzle where moving a single piece becomes much harder compared to its loose form. In contrast, without such interlocking mechanisms, the pieces, i.e., small organic molecules at an interface without non-covalent interactions, would easily displace (Figure 14b).

In the following, we delve into various non-covalent interactions that play a crucial role in the creation of supramolecular materials at the liquid interface. Also, we explored the connection between the intrinsic properties of these supramolecular materials and the characteristics of the resulting structured liquids, alongside the impact of different non-covalent interactions. Table 2 presents a comprehensive list of molecules, ligands/surfactant options, and choices of liquids, along with key insights from studies focused on supramolecular assembly. These studies will be explained in detail in the following subsections.

Table 2: A comprehensive list of molecules, ligands/surfactant options, and liquid choices in supramolecular assemblies

Liquid Construct	**Type of Assembly**	**Ligand/surfactant**	**Remarks**	**Ref.**
Structured liquid at toluene/water interface	Hydrogen Bonding	POSS-8A	The assembly of amine-functionalized POSS molecules at the toluene/water interface can be controlled by altering the pH, the concentration of POSS used, and the number of amine groups attached to each POSS molecule.	105
Structured liquid at toluene/water interface	Hydrogen Bonding	P[5]AA	The assembly of P[5]AA at the liquid-liquid interface depends on pH.	106
Structured Pickering emulsion	Hydrogen Bonding	Cell-C_8	Non-ionic surfactants such as Cell-C_8 can form a crystalline monolayer at the interface between organic solvents and water.	107
Structured Pickering emulsion	Hydrogen Bonding	CEL-C_6	The CEL-C_6 nanocellulose can assemble and jam at n-undecane/water interface.	108
Structured liquid at toluene/water interface	Electrostatic Interaction and π-π Stacking	PS-NH_2/H_6TPPS PS-NH_2/MnH_4TPPS PS-NH_2/MA	Different interfacially active molecules displayed varying effectiveness in stabilizing the interface and decreasing the interfacial tension between two liquids. This diversity can be explained by examining their molecular structures and the interactions they create at the oil/water interface.	12
Structured liquid at toluene/water interface	Electrostatic Interaction	PDMS-NH_2/ H_6TPPS	Interfacially active molecules like H_6TPPS, MnH_4TPPS, and MA are dissolved in the aqueous phase and	12

	and π-π Stacking	PDMS-NH_2/ MnH_4TPPS PDMS-NH_2/MA	interact with a nonpolar domain containing PDMS-NH_2/oil to form supramolecular polymer surfactants (SPS).	
All-liquid 3D-printed structures	Electrostatic Interaction and π-π Stacking	POSS-$NHC_2H_4NH_2$ /$H_4TPPS_2^-$	The assembly of H_4TPPS_2 at the oil/water interface, combined with its interaction with POSS-$NHC_2H_4NH_2$, leads to the formation of SPSs.	[13]
Assembling of microfluidic droplets	Host-Guest Interaction	P_1/CB[8]/P_2	A combination of hydrophilic and hydrophobic copolymers coupled with CB[8] was used to develop structured microcapsules through host-guest Interaction.	[109]
Free-standing assembled monolayer film	Host-Guest Interaction	Np-Trx/ CB[8]/MV-NDI	2D SOFs have been developed at a liquid-liquid interface by employing a donor and acceptor-enhanced host-guest interaction mechanism.	[110]
Supramolecular Microcapsules	Host-Guest Interaction	MV^{2+}/CB[8]/naphthol	A flexible host-guest system has been developed to utilize microfluidic droplets as templates for producing porous microcapsules, whose functionality can be customized.	[111]

A complete list of used abbreviations in this table is provided in Table S1 within the supporting information.

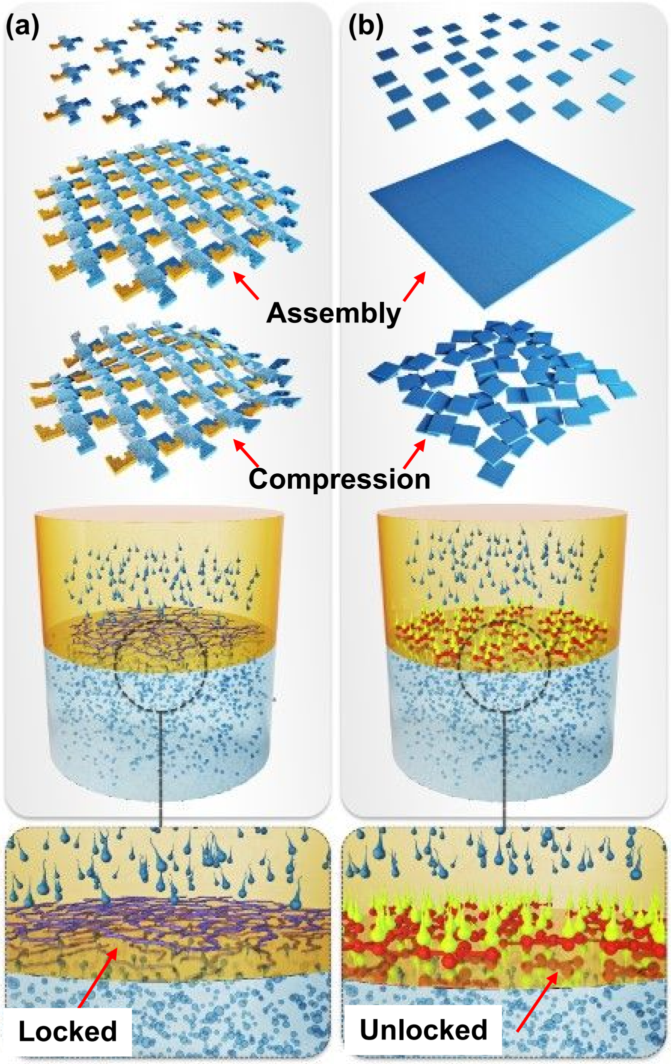

Figure 14: (a) A puzzle-like assembly consists of pieces that interlock with one another. (b) A puzzle-like assembly is composed of pieces that do not interlock and are easily detached from the interface upon applying an external force.

3.3.1 Supramolecular assemblies via hydrogen bonding and van der Waals forces

Hydrogen and van der Waals bonds stand out as exceptionally suitable non-covalent interactions for assembling supramolecular polymers owing to their unique combination of high strength and reversibility. Moreover, the strength and reversibility of these bonds can be controlled through the strategic design of bonding groups within the monomers and used materials. This enables the construction of reconfigurable supramolecular connections at the oil/water interface, which are used in many applications in designing structured liquids.[103, 112]

The role of hydrogen bonds in developing structured liquids has been recently demonstrated via interfacial complexation and jamming of amine-functionalized polyhedral oligomeric silsesquioxanes (POSS-nA) at the oil/water interface.[105] In this work, the assembly and jamming of POSS-nA molecules at the interface created a robust film that stabilized liquid droplets into non-equilibrium shapes (Figure 15a). The results also highlighted the role of pH, POSS-nA concentration, and functionalization degree in modulating interfacial tension, revealing how these factors influence the formation of interfacial supramolecular films. At acidic conditions (pH 4), POSS-8A exhibits strong electrostatic repulsion due to its protonated amine groups, which prevents the particles from aggregating at the interface (Figure 15b). This phenomenon is attributed to the discrete macroanionic nature of POSS-8A, carrying positive charges balanced by counter-anions, which leads to repulsive interactions among POSS units, hindering their close packing and assembly compression. As the pH increases, the study notes a transition in the behavior of POSS-8A. Beyond the pKa value of the amine groups (around pH 9), the protonation of amine groups decreases, allowing for increased hydration and stabilization of POSS-8A at the interface through intermolecular hydrogen bonding (Figures 15c-d). This results in a significant reduction of the equilibrium interfacial tension, indicating a stronger assembly and interfacial activity of amine-functionalized POSS at higher pH levels. The interfacial tension decreases further as the pH value increases, underscoring the importance of pH in modulating the assembly and stability of POSS molecules. Furthermore, through dynamic interfacial tension (IFT) measurements of aged aqueous droplets of POSS upon contact with a pure toluene solution, the influence of different levels of amine functionalization was examined. A comparison between POSS-4A, POSS-6A, and POSS-8A reveals that a higher degree of functionalization results in lower interfacial tensions and more stable assemblies.

In another study, Varshney et al.[106] developed reconfigurable structured liquids based on interfacial assembly and jamming of pillar[5]arene carboxylic acid (P[5]AA). The mechanism of this assembly can be explained based on hydrogen bonding between supramolecular species that can undergo successive jamming and unjamming states upon changing the pH (Figures 15e-g). Interestingly, P[5]AA functions as a macrocyclic anion at elevated pH levels, where electrostatic repulsion between anions reduces interface stability, reflecting minimal interfacial activity. Conversely, at acidic pH levels of 2-4, P[5]AA assumes its protonated form (–COOH), enabling intermolecular hydrogen bonding and supramolecular assembly, which significantly enhances interface stability and lowers IFT to about 16 mN/m.

Figure 15g showcases the transition from a jammed to an unjammed state in an aqueous droplet containing P[5]AA. Initially conducted at pH 10, a 20 ml aqueous solution of P[5]AA was introduced into 20 mL of toluene, forming a pendant droplet without any observable wrinkles during volume compression. However, the introduction of 2 ml (1M) of trifluoroacetic acid (TFA) into the oil phase induced the formation of wrinkles upon volume reduction, attributable to hydrogen bonding interactions at acidic pH. Remarkably, the wrinkles disappeared, and the droplet reverted to its equilibrium shape upon the addition of an excess of triethylamine (4 ml; 1M TEA), which elevated the solution's pH and disrupted the hydrogen bonding. The cycle of hydrogen bond-mediated assembly/jamming and disassembly/unjamming of P[5]AA aggregates was visually represented and quantified through surface coverage measurements after a 30-minute aging period of the droplet, following alternating additions of acid and base. Furthermore, pH-responsive molecular diffusion within a pendant droplet stabilized by P[5]AA aggregates was investigated, showcasing controlled release mechanisms dependent on the droplet's state. This was evidenced by the release patterns of a dye and the visual transition between locked and unlocked states of pendant droplets containing Rh6G dye. Consequently, this experiment highlights the potential of supramolecular assemblies to function as intelligent, responsive systems through deliberate manipulation of environmental conditions. This feature suggests these structured systems could serve as intelligent delivery systems, a topic that is thoroughly explored in Section 5 of this review article.

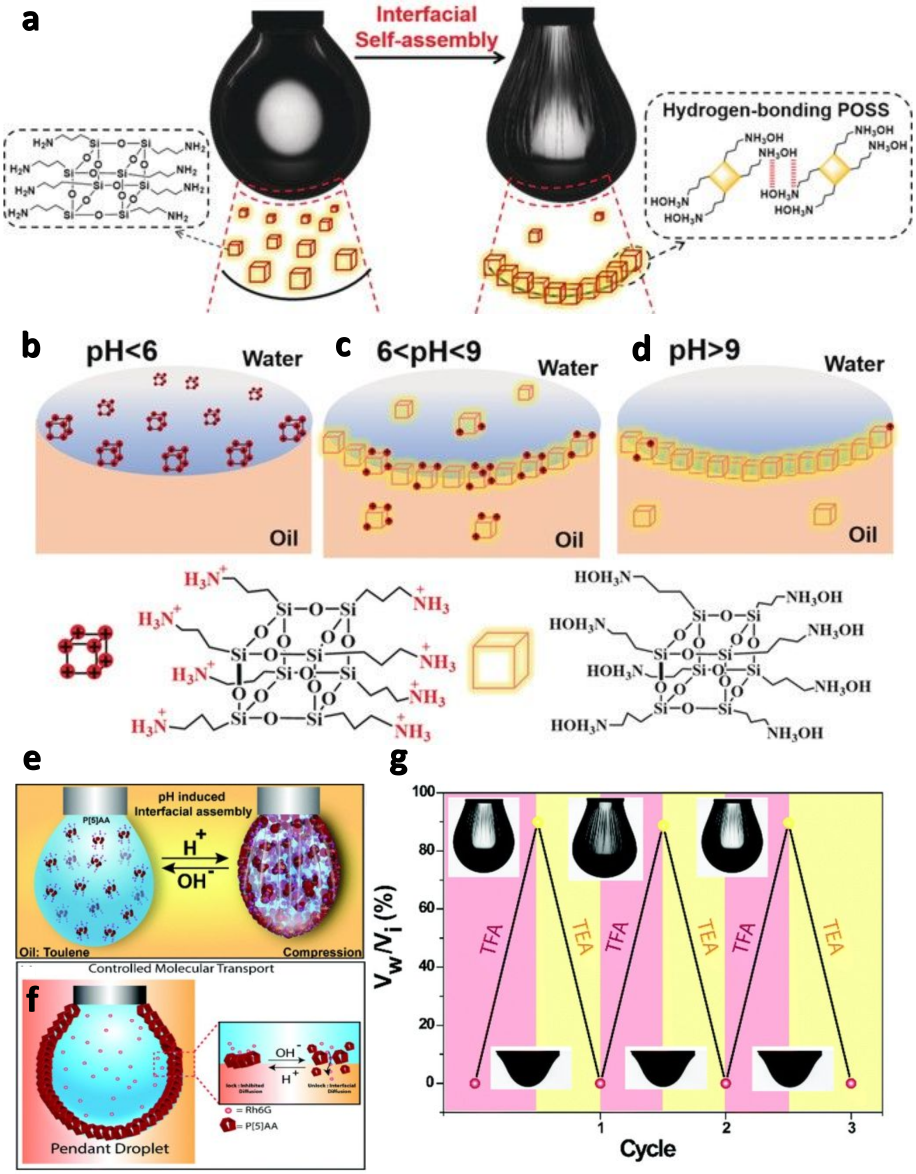

Figure 15: (a) Interfacial assembly and Jamming of POSS-8A molecules at liquid-liquid interface. (b-d) The assembly of POSS-8A is pH-dependent. (a-d) Reproduced with permission.[105] Copyright 2019, Wiley-VCH. (e-f) The assembly and jamming of P[5]AA at the oil/water interface is pH-dependent. (g) By adjusting the pH, the assembly of P[5]AA at the liquid-liquid interface can cycle between a jammed and an unjammed state. (e-g) Reproduced with permission.[106] Copyright 2021, Royal Society of Chemistry.

In another study, Hata and colleagues demonstrated that non-ionic crystalline surfactants, specifically n-octyl cello-oligosaccharide (Cell-C8), can assemble and jam at liquid-liquid interface, as shown in Figure 16a.[107] The self-assembly of Cell-C8 is driven by intermolecular hydrogen bonding and van der Waals forces, showcasing remarkable mechanical and chemical stability under various conditions, including different solvents, high ionic strengths, and extreme pH levels.

Similarly, the interfacial jamming capabilities of nanocelluloses without the addition of any ligand to the system were studied.[108] For this aim, rectangular sheet-like synthetic nanocelluloses composed of cello-oligosaccharides were synthesized and functionalized with various moieties, including ethyl (CEL-C2), butyl (CEL-C4), and hexyl groups (CEL-C6), as well as without alkyl groups (CEL-OH). Despite their nonionic nature and the presence of alkyl groups, these synthetic nanocelluloses were water-dispersible. This was attributed to their flat surfaces being coated with terminal saccharide residues, ensuring effective hydration.

Interestingly, among all samples, CEL-C6 with longer alkyl chains was the only one capable of adsorbing and jamming at the n-undecane/water interface through hydrogen bonding and van der Waals forces (Figure 16b). In this regard, upon contacting a pendant drop containing an aqueous phase of CEL-C6 in a nonpolar domain, visible wrinkles formed at the interface, showcasing the solid-like behavior of the interfacially driven skin (Figure 16c). This behavior can be attributed to the unique structural properties of the hexylated nanocelluloses. First, due to its sheet-like structure, CEL-C6 has an exceptional surface area that pushes these materials to the interface to reduce the energy differences between two immiscible liquids. Second, CEL-C6 has a dual hydrophilic/hydrophobic nature that makes it capable of interacting with both immiscible phases at the liquid-liquid interface, further reducing the interfacial tension. Consequently, these findings hold promise for the advancement of all-liquid devices utilizing nanocellulose-based materials.

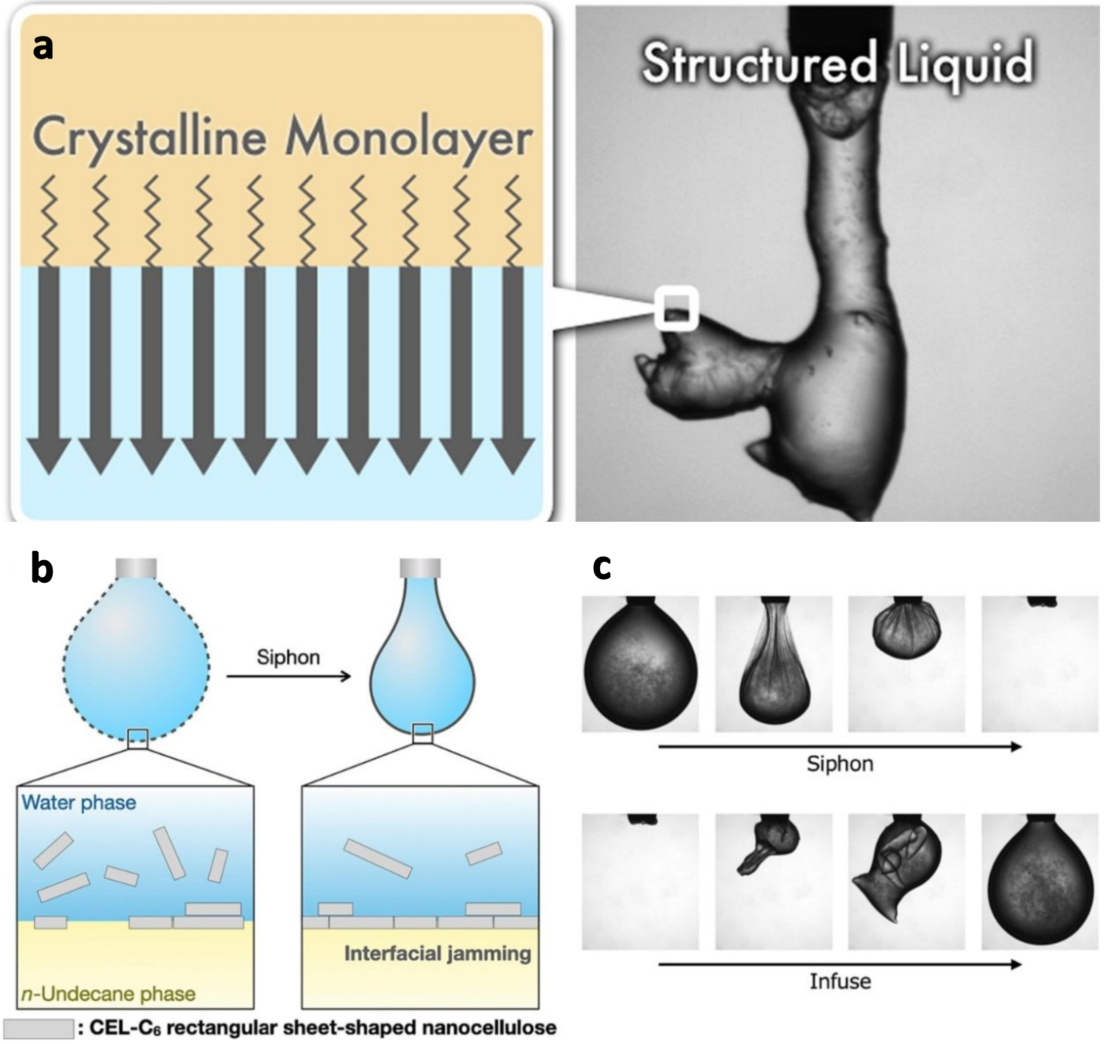

Figure 16: (a) The assembly and jamming of Cell-C8 at the liquid-liquid interface can stabilize the interface by forming a solid-like monolayer of supermolecules at the interface. (a) Reproduced with permission.[107] Copyright 2021, Elsevier. (b) A schematic illustration showing how the buckling phenomenon occurs due to the interfacial jamming of CEL-C6 at the n-undecane/water interface. (c) A sequence of images indicating changes in the shape of a pendant droplet filled with Cell-C6 as it is gradually siphoned off and then refilled. (b-c) Reproduced with permission.[108] Copyright 2024, Elsevier.

3.3.2 Supramolecular assemblies via electrostatic interaction and π-π stacking

In supramolecular chemistry, π−π stacking refers to a type of non-covalent interaction observed between organic compounds that feature aromatic groups. This interaction arises from the overlapping of p-orbitals within π-conjugated systems, becoming more pronounced with an increase in the number of π-electrons.[103] On the other hand, electrostatic interactions, which can be attractive or repulsive, play a crucial role in the formation of supramolecular materials. These interactions occur between molecules with opposite charges and are frequently employed in techniques such as layer-by-layer deposition to construct supramolecular structures.[113, 114]

While π−π stacking and electrostatic forces might not match the strength of hydrogen bonding, their combination with each other or with other non-covalent forces has proven remarkably effective in fabricating supramolecular materials. This synergistic approach leverages the unique contributions of each interaction type to create more stable and functional supramolecular structures. In this context, a recent study explored three molecules capable of forming structured liquids through π−π stacking and/or electrostatic forces, aiming to demonstrate how these intermolecular interactions contribute to stabilizing the liquid-liquid interface.[115] The selected molecules were 5,10,15,20-tetrakis(4-sulfonatophenyl)porphyrin (TPPS), the manganese(III) chloride derivative of TPPS (MnTPPS), and mellitic acid (MA), as depicted in Figures 17a-c. However, as anticipated, these molecules showed different performances in stabilizing the interface and reducing the interfacial tension between two liquids (Figures 17d-f). This variation can be elucidated based on their molecular structures and the resulting interactions at the oil/water interface.

For example, when an aqueous phase containing H_6TPPS meets the oil phase containing amine-terminated hydrophobic polymers (PS-NH_2), supramolecular polymer surfactants (SPSs) start forming at the interface. This process, powered by intermolecular electrostatic attractions and π-π stacking, leads to a decrease in interfacial tension and enables the liquids to maintain non-equilibrium shapes. In contrast, a similar molecule, MnH_4TPPS, acts more like a conventional surfactant by reducing interfacial tension without shaping liquids. This difference is partly attributed to one of the porphyrin surfaces in MnH_4TPPS being covered by a chloride ion, diminishing intermolecular interactions. Moreover, the size of the molecule plays a pivotal role in SPS formation. For instance, MA, with its weaker π-π stacking and a single benzene ring, lacks the necessary size to facilitate adequate intermolecular interactions for SPS formation (Figures 17g-i).

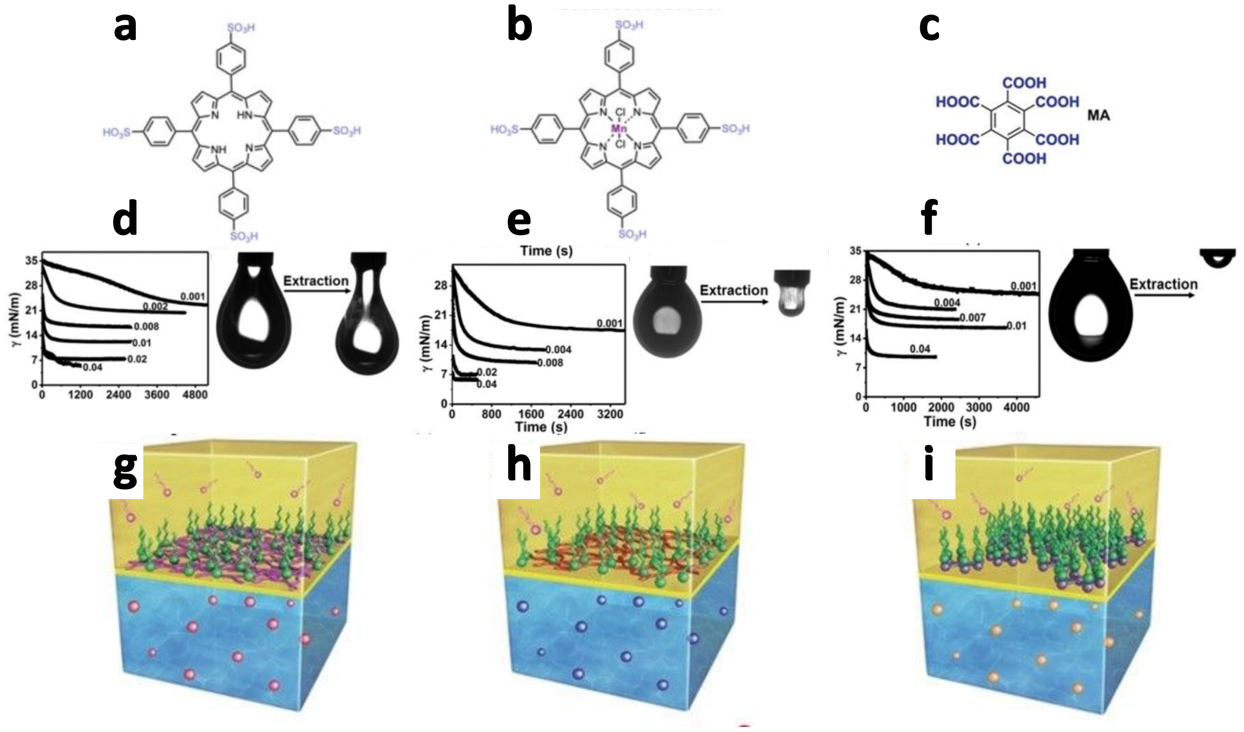

Figure 17: (a) H_6TPPS, (b) MnH_4TPPS, and (c) MA chemical structures. Interfacial tension measurements and contraction relaxation tests were conducted on aqueous pendant drops containing (d) H_6TPPS, (e) MnH_4TPPS, and (f) MA in an external nonpolar domain of PS-NH_2/toluene. Schematic illustration of interfacial assembly and jamming of systems containing a

nonpolar domain of PS-NH_2/toluene and an aqueous solution of (g) H_6TPPS, (h) MnH_4TPPS, and (i) MA against. (a-i) Reproduced with permission.[115] Copyright 2019, Wiley-VCH.

In another investigation, the interfacial assembly and jamming of supramolecular polymer surfactants (SPSs) were examined through the color-changing properties of H_6TPPS, which vary based on its aggregation state at the interface.[13] As detailed in Figure 18, an aqueous solution of H_6TPPS is injected into an oil solution containing aminoethylaminopropyl isobutyl polyhedral oligomeric silsesquioxane (POSS-$NHC_2H_4NH_2$) dissolved in silicone oil. Upon contact, POSS-$NHC_2H_4NH_2$, acting as a potent surfactant, forms a monolayer at the interface to lower interfacial tension. H_6TPPS, once dissolved in water and transformed into H_4TPPS^{2-} along with H^+ ions, migrates to the interface, where it electrostatically interacts with POSS-$NHC_2H_4NH_2$ to create in-situ SPS (H_4TPPS^{2-}POSS-$NH_2^+C_2H_4NH_3^+$). This interaction prompts the formation of J-aggregates of H_4TPPS^{2-}, which display a green color caused by edge-to-edge interactions, wherein the cationic nitrogen atoms neutralize the negatively charged SO_3^- groups. This green state marks the initial phase of pattern formation, as shown in Figures 18b-d. Subsequently, as H_4TPPS^{2-} accumulates at the interface, it releases more protons to form H_2TPPS^{4-}, which exhibits a light red color and interacts electrostatically with additional POSS-$NH_2^+C_2H_4NH_3^+$, transitioning into a different SPS structure (H-aggregates of H_2TPPS^{4-}(POSS-$NH_2^+C_2H_4NH_3^+)_2$). This dynamic color change from J-aggregates to H-aggregates offers a visual mechanism to track the evolving structure and assembly of SPSs at the liquid-liquid interface, enabling real-time monitoring of the electrostatic interfacial dynamics.

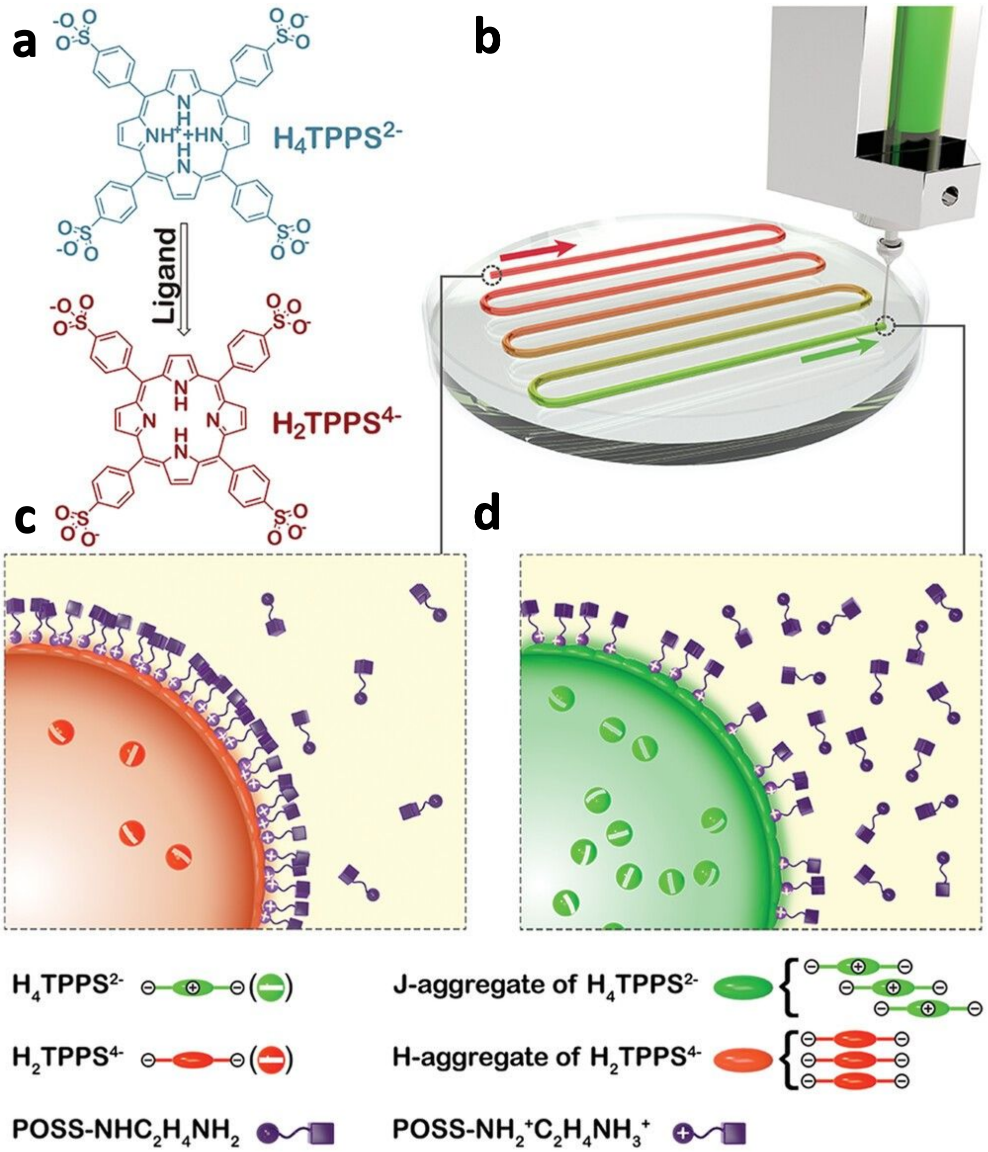

Figure 18: (a) H_4TPPS^{2-} transitions to H_2TPPS^{4-} through interactions with POSS-$NHC_2H_4NH_2$. (b-d) An overview of the 3D printing process and underling mechanisms that can visualize the assembly of J- and H-aggregates with different colours. (c) A schematic illustration of the interfacial assembly of SPSs at the liquid-liquid interface (H_2TPPS^{4-}(POSS-NH_2^{+}C2$H_4NH_3^{+}$)$_2$), showcasing a red-colored interface due to the formation of H-aggregates of H_2TPPS^{4-}. (d) A representation of the interfacial assembly of SPSs (H_4TPPS^{2-}POSS-$NH_2^{+}C_2H_4NH_3^{+}$), illustrating a green-colored interface as a result of J-aggregates of H_4TPPS^{2-} formation. (a-d) Reproduced with permission.[13] Copyright 2021, Wiley-VCH.

3.3.3 Supramolecular assemblies via host-guest interaction

Host-guest chemistry revolves around the concept of molecular recognition, where molecules selectively and specifically bind to each other via non-covalent interactions such as hydrogen bonding, van der Waals forces, π-π interactions, and electrostatic forces.[116, 117] This smart assembly facilitates the formation of highly structured and functional systems. Key to this field are macrocyclic compounds like pillar[n]arenes,[118] cucurbit[n]urils,[119] and cyclodextrins (CDs),[120] which serve as hosts in these interactions, forming complexes with various guest molecules. These complexes function through a lock-and-key mechanism, where the host (lock) has a cavity that specifically recognizes and binds to the guest (key), which can be organic compounds, macromolecules, metal ions, or nanoparticles. The dynamic and reversible nature of host-guest interactions equipped supramolecular materials with unique properties, such as self-healing and responsiveness to stimuli like pH, temperature, and redox conditions. Hence, the design of host and guest molecules can be finely tuned with specific functional groups to achieve desired behaviors and functionalities.[103, 121]

Zheng et al.[109] reported a novel method for the host-guest interfacial assembly of supramolecular dendritic microcapsules within microfluidic media. Interestingly, they utilized a combination of hydrophilic and hydrophobic copolymers. The process involves the controlled co-assembly of these copolymers at the chloroform/water interface within a microfluidic droplet, which is then followed by host-guest complexation with cucurbit[8]uril (CB[8]). This results in the reversible crosslinking of the functionalized copolymers, leading to the formation of a polymeric skin at the interface, encapsulating the droplets, and forming monodisperse, supramolecular polymer-only microcapsules. Figures 19a-b detail the mechanism and outcomes of this process, illustrating the encapsulation of water-soluble molecules (specifically Congo Red (CR)) by a dendritic copolymer

(H1), and their transfer into an organic solvent. This is achieved through a microfluidic device where an aqueous phase of CB[8] and water-soluble poly(HEMA-co-StMV-co-FOA) (P1) overlaps with a stream of chloroform containing the dendritic copolymer H1. The result is the formation of chloroform-in-water microdroplets, where the interfacial assembly leads to the formation of a microcapsule skin, as evidenced by bright field and fluorescence microscopy (Figures 19c-d). The successful encapsulation and structuring are further validated through fluorescence images, which confirm the entrapment of CR within the microcapsule wall. However, in the absence of CB[8], P1 and H1 failed to assemble at the interface, resulting in the formation of dense polymer beads of H1 upon solvent evaporation. This innovative approach not only showcases the feasibility of fabricating microcapsules via interfacial supramolecular host-guest polymerization but also highlights the efficiency of dendritic polymers in encapsulating small molecules. The utilization of microfluidic devices for this process underscores the precision and control achievable in the spatial organization and chemical functionalities of the resultant microcapsules, promising a wide range of applications from drug delivery to material encapsulation.[122, 123]

Classical emulsification techniques often produce colloidal microcapsules with a wide size distribution. To narrow this distribution, researchers have increasingly turned to microfluidics for microcapsule production. In this regard, a one-step fabrication method for creating supramolecular microcapsules using microfluidic droplets was proposed to simplify and scale the production of microcapsules without sacrificing functionality or encapsulation efficiency (Figure 19e).[111] Utilizing a host-guest system comprising polymer-gold (Au) nanoparticle composites and CB[8] ternary complexes, this approach allows for the generation of porous, dynamically stable microcapsules. In detail, microcapsules form as the oil phase strips away from a water phase containing CB[8], methyl viologen (MV)-functionalized Au nanoparticles, and naphthol-functionalized polymers. The Au nanoparticles migrate to the oil/water interface, where they facilitate host-guest interactions with the complementary polymers. This leads to the microcapsule's membrane formation, which can be used as cargo (Figures 19f-h). Also, these uniformly sized microcapsules can be easily collected after the evaporation of the water droplets and retain their spherical shape during rehydration (Figures 19i-j). The core content and shell composition of the microcapsules can be precisely controlled, marking a significant step in various applications, including drug delivery, diagnostics, and electronic displays.

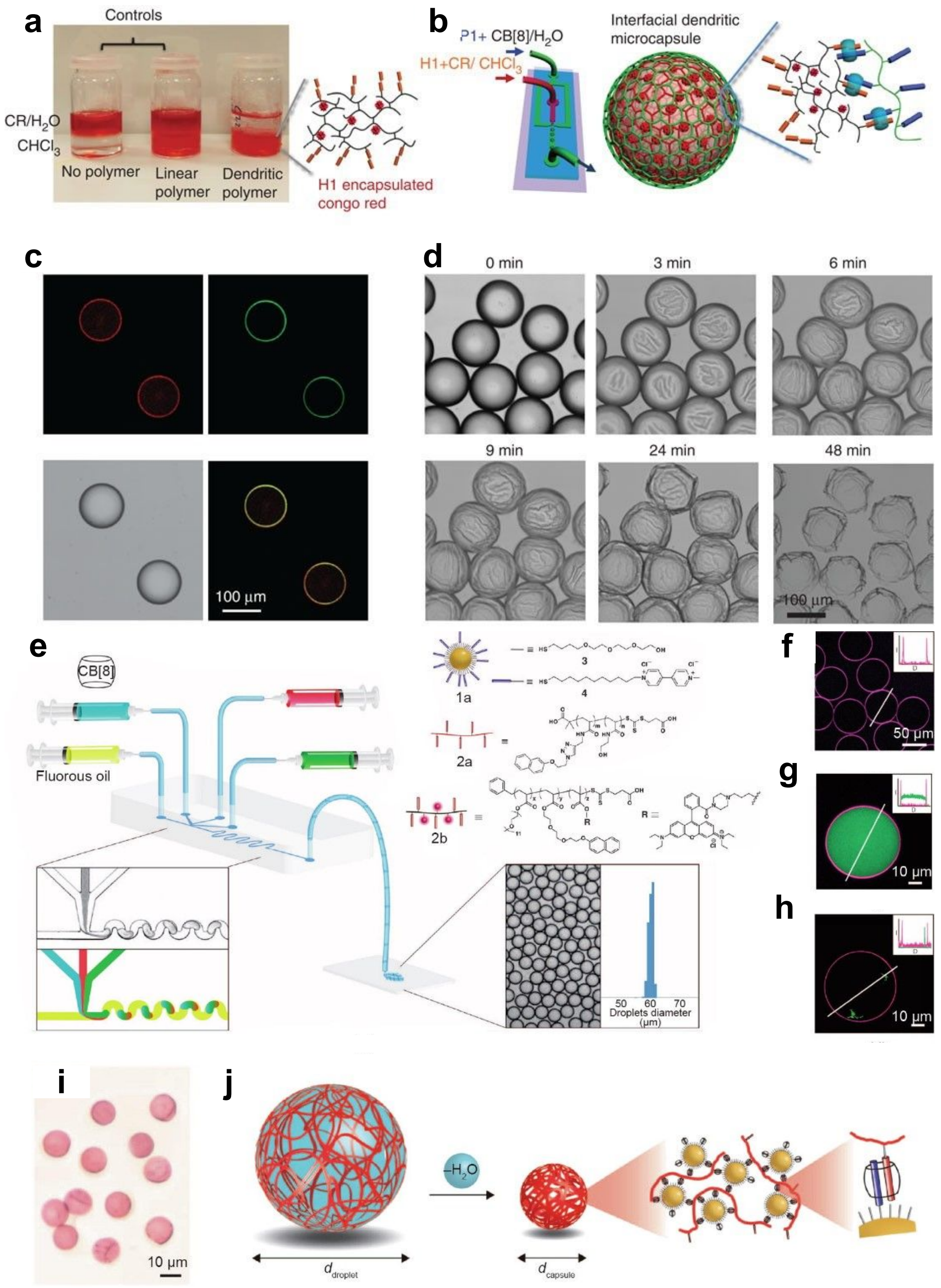

Figure 19: (a) A visual representation demonstrating the encapsulation of water-soluble CR by the dendritic copolymer, H1, followed by its transfer into an organic solvent. (b) A diagram illustrating the process of microdroplet formation through a microfluidic device, which includes an aqueous phase with CB[8] and P1 overlapping with a stream of chloroform. This chloroform contains the

dendritic copolymer H1 with encapsulated CR, leading to the formation of chloroform-in-water microdroplets. (c) Optical and fluorescence microscopy images reveal the formation of uniform microdroplets, showing the interfacial assembly consisting of an inner H1 layer (with entrapped CR) and an outer P1 layer (labeled with fluorescein). (d) Bright-field microscopy images capture the creation of the microcapsule shell as the chloroform within the microdroplet evaporates, leading to a collapsed capsule-like structure. (a-d) Reproduced with permission.[109] Copyright 2014, Nature Publishing Group. (e) Diagrams illustrating the process of microdroplet creation through microfluidic devices. (f) Images from laser scanning confocal microscopy showing empty microcapsules with component 2b assembled at the interface. Confocal microscopy images displaying microcapsules containing (g) fluorescein isothiocyanate-labeled dextran (FITC-dextran) and (h) encapsulated Escherichia coli cells. (i) Optical images of the microcapsules. (j) Schematic demonstration of the dehydration process applied to the microcapsules. (e-j) Reproduced with permission.[111] Copyright 2012, American Association for the Advancement of Science.

Equally interesting, an approach to creating two-dimensional supramolecular organic frameworks (2D SOFs) via a host-guest interaction mechanism at a liquid-liquid interface was advanced recently.[110] In this work, large-area, free-standing monolayers with excellent internal order were achieved by integrating a tris(methoxynaphthyl)-substituted truxene (Np-Trx) donor and a naphthalene diimide (MV-NDI) acceptor with CB[8] (Figure 20a). To better understand the fabrication procedure, Figures 20b-e illustrate the stepwise process of self-assembly and deposition for creating a 2D SOF. Initially, an aqueous solution with preassembled components is prepared, followed by the addition of a solvent containing the donor molecule. Over time, the two-phase system facilitates the assembly at the liquid-liquid interface. Finally, the solutions are drained to isolate the assembled structure. These schematics demonstrate the intricate methodology employed to achieve the highly ordered, monolayer 2D SOF, showcasing the interaction between the components throughout the assembly process.

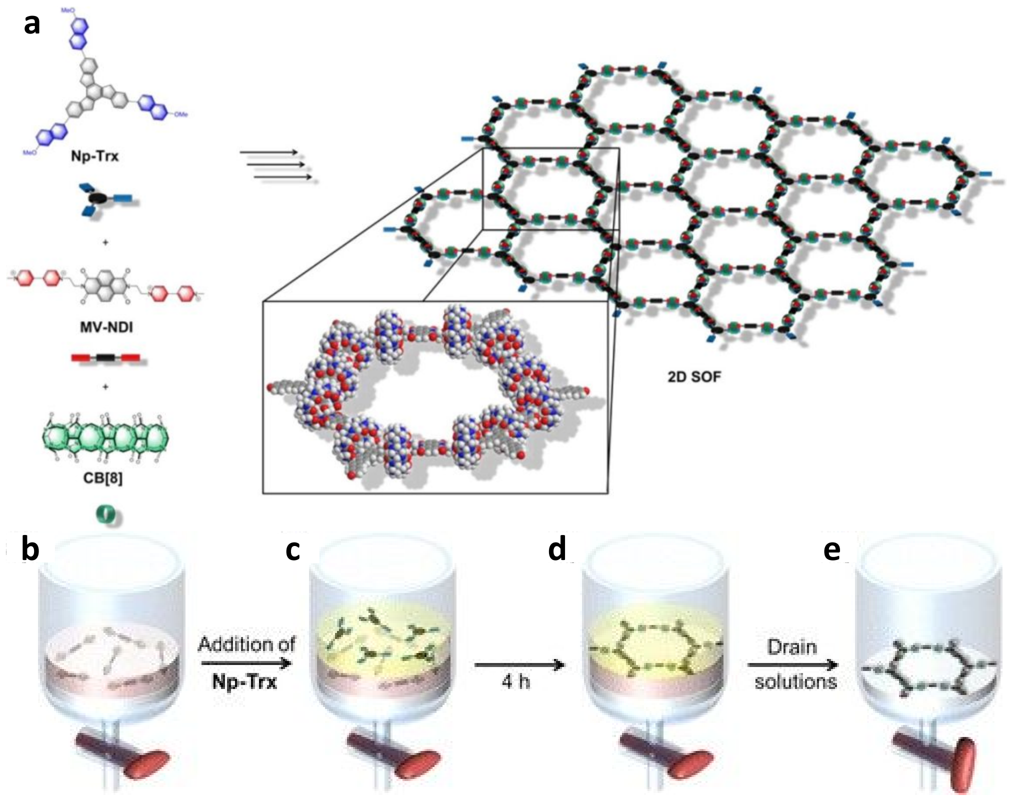

Figure 20: (a) Schematic illustration of the assembled system containing Np-Trx, MV-NDI, and CB[8]. (b-e) Step-by-step assembly of these structured systems at the toluene/water interface. (b) This process begins with an aqueous solution containing preassembled MV-NDI and CB[8]. (c) The two-phase system is then formed by the addition of an Np-Trx/toluene phase to the aqueous phase. (d) The self-assembled structure is then formed at the interface after a 4-hour assembly period. (e) The final, isolated assembled structure is obtained after draining the solutions through a valve located at the bottom of the trough. (a-e) Reproduced with permission.[110] Copyright 2015, American Chemical Society.

4 Reconfigurability of structured liquids

Reconfigurable structured liquids represent one of the most captivating topics in the field of interfacial assembly, where the rearrangement of nanoparticles or supramolecular assemblies at the liquid-liquid interface can be managed by external or internal stimuli. In this regard, external stimuli such as light and magnetic/electric fields serve as crucial parameters for manipulating the assembly of nanoparticles or macromolecules at the liquid-liquid interface. Simultaneously, internal stimuli derived from interactions within the system, such as alterations in pH or the utilization of Redox potential, also prove instrumental in reshaping structured liquids.[1, 14, 124, 125] In the subsequent section, we delve into the most intriguing perspectives of responsive structured liquids, seamlessly bridging the discussion from external to internal stimuli. These insights draw upon the latest studies, providing a comprehensive view of the evolving landscape in this field.

4.1 External stimuli

4.1.1 Photo-responsive structured liquids

The classic photoisomerization of molecules, i.e., photo-controlled molecular recognition, is a powerful tool for developing photo-responsive structured liquids.[124, 126, 127] In this regard, at least one of the active materials that assemble at the interface to form NPSs can go through photo-controlled molecular recognition and terminate/reform the NPS species at the liquid-liquid interface. An example of such photo-responsive structured liquids was recently developed based on the photo-controlled interaction of α-cyclodextrin (α-CD) and azobenzene (Azo) at a liquid-liquid interface.[128] In this study, the NPS assemblies were formed based on the interaction of α-CD-modified Au nanoparticles, i.e., an aqueous phase, and the oil-soluble Azo-terminated polymeric ligands in toluene, i.e., Azo-terminated polystyrene (Azo-PS, Mw =3.3 K) and Azo-terminated poly-L-lactide (Azo-PLLA, Mw =3.6 K) (Figure 21a). The results show that the incorporation of both Azo-PLLA and Azo-PS results in the formation and assembly of NPS, which offer sufficient binding energy to hold α-CD-modified Au nanoparticles in a jammed state. However, Azo-PLLA-based NPS assemblies' formation is much faster and stronger compared to that of Azo-PS-based assemblies due to the hydrogen bonds formed between Azo-PLLA and water/αCD. Specifically, α-CD-modified Au nanoparticles/Azo-PLLA NPSs can become saturated and achieve nearly full coverage (approximately 100%) within just 600 seconds.

The photo-responsiveness of Azo-PLLA and Azo-PS-based NPSs and their assemblies was assessed through expansion/contraction tests of pendant drops. As depicted in Figure 21a, under visible light irradiation, NPSs in both systems effectively jammed the oil/water interface, evident in the formation of stable wrinkles at the liquid-liquid interface upon droplet contraction. However, when exposed to UV light at a wavelength of 365 nm, the wrinkles gradually disappeared, and the droplet underwent relaxation, indicating the unjamming of the NPS assembly at the liquid-liquid interface. Here, before UV irradiation of Azo-PLLA-based samples, the jammed NPSs were firmly held at the interface due to interfacial host-guest interactions between trans-Azo-PLLA and αCD, along with hydrogen bonding between Azo-PLLA and water/αCD. However, under UV light, trans-Azo-PLLA underwent photoisomerization to form cis-Azo-PLLA, which could not interact with α-CD, resulting in an unjammed state at the liquid-liquid interface.

A similar study used the host-guest interactions between Azo-PLLA and α-CD-modified Au nanoparticles at the liquid-liquid interface to make structured photo-responsive microcapsules.[74] Notably, under UV irradiation, the Azo-PLLA/α-CD-modified Au NPSs could become unjammed, leading to the subsequent release of the cargo contained within the microcapsules into an external oil phase. As a proof of concept, the authors loaded these microcapsules with Rhodamine B (RhB) and quantitatively examined its release using fluorescence imaging (Figures 21b-c). The results illustrated a time-dependent dissociation of RhB that could be further controlled/programmed by alternately exposing the samples to UV and visible light irradiation.

In another study, a photo-responsive host-guest interfacial assembly of alginate-modified β-cyclodextrin (Alg-β-CD) and azobenzene-functionalized alkyl chains (AzoC12) in the presence of cosurfactants, namely polyvinyl alcohol (PVA) and Span 60 was introduced.[129] In this work, Pickering emulsions were prepared by combining an aqueous phase containing PVA and Alg-β-CD with an oil phase containing AzoC12 oil and Span 60. The resulting soft supra-colloidal aggregates were then obtained through emulsion-solvent evaporation (Figure 21d).

The supramolecular Alg-β-CD/AzoC12 polymer systems demonstrated exceptionally high interfacial activity, achieving an interfacial tension of ~0.7 mN/m. This strong assembly is due to the robust interaction between β-CD and Azo at the oil/water interface. However, this elevated interfacial activity could be suppressed by UV irradiation. Before irradiation, the Azo moieties of trans-AzoC12 demonstrated a strong interaction with the hydrophobic moieties of Alg-β-CD through host-guest interactions. However, upon UV irradiation, trans-AzoC12 underwent photoisomerization to form cis-AzoC12, resulting in the cessation of host-guest interactions, as evidenced by interfacial tension measurements and TEM investigations (Figures 21e-g).

Photo-responsive assemblies at the liquid-liquid interface have also been used for controllable heterogeneous catalysis. In this regard, Li et al.[130] introduced a novel light-responsive Pickering emulsion, leveraging Pd-supported silica nanoparticles, a water-soluble azobenzene-based ionic liquid surfactant (ILS) - specifically [C4AzoC2DMEA]Br, [C4AzoC4DMEA]Br, [C4AzoC6DMEA]Br, or [C4AzoC8DMEA]Br - along with n-octane and water. The experimental results showed that the initially stable Pickering emulsions experienced destabilization, leading to a full phase separation between water and oil when subjected to UV irradiation with stirring. However, subsequent irradiation with visible light after homogenization effectively restored the stable emulsions. This observed phase behavior is attributed to the adsorption of the azobenzene ionic liquid surfactant on the surface of nanoparticles and the light-responsive activity of the ionic liquid surfactant. The developed Pickering emulsion serves as a versatile microreactor, facilitating catalytic reactions, product separation, and the recycling of both emulsifiers and catalysts.

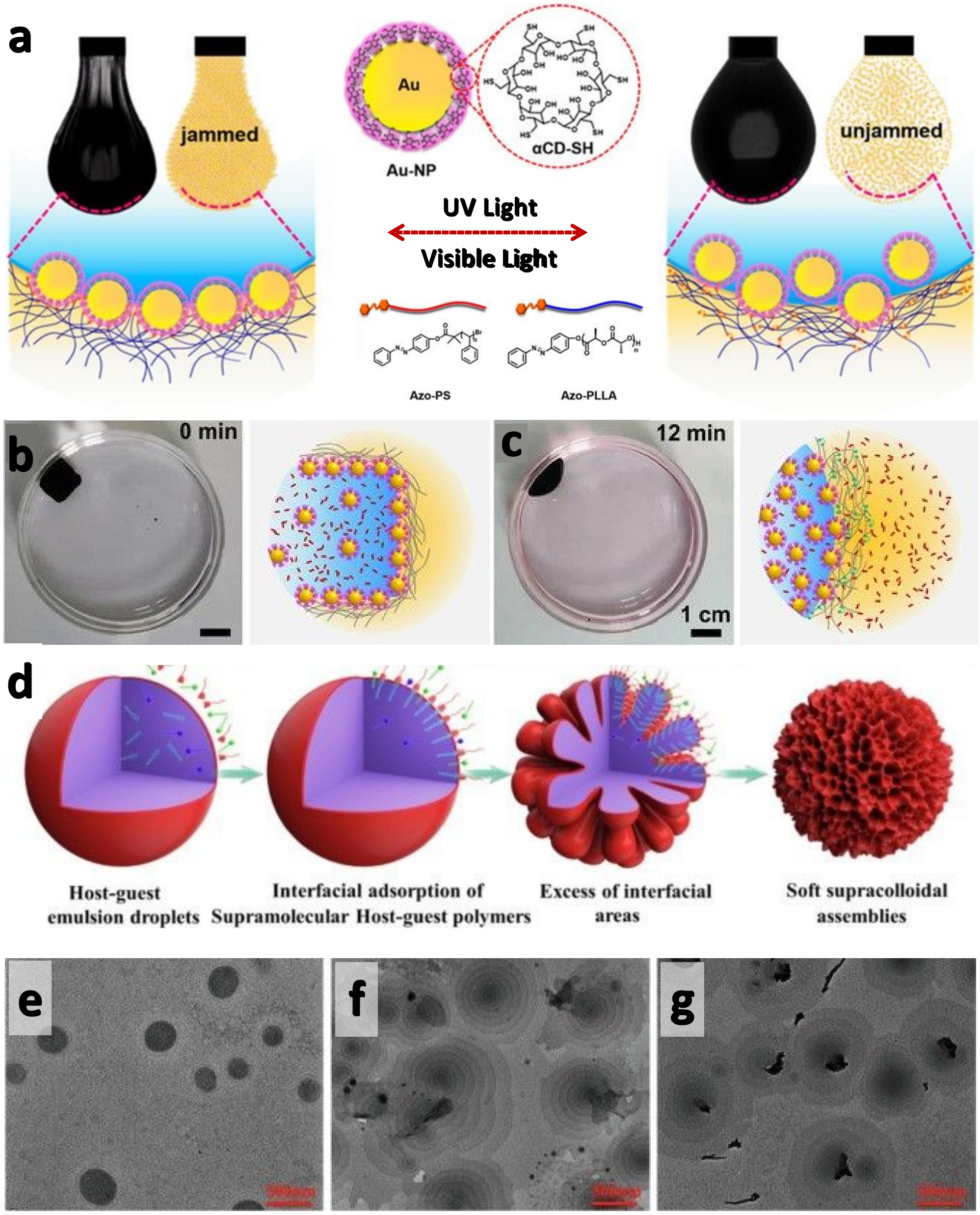

Figure 21: Photo-responsive structured liquids. (a) Photo-responsive structured liquids based on α-CD-modified Au nanoparticles and the oil-soluble Azo-terminated polymeric ligands. Under visible light, the jamming of NPSs at the oil/water interface forms stable wrinkles during droplet contraction, while UV irradiation at 365 nm causes wrinkles to vanish due to the unjammed state of NPSs. (a) Reproduced with permission.[128] Copyright 2020, American Chemical Society. Optical image and schematic illustration of photo-responsive microcapsules based on Azo-PLLA/α-CD-modified Au NPSs (b) Under visible light and (c) after 12 min UV exposure. The

capsules were loaded with RhB, and after the unjamming process, the release of RhB was visible. (b-c) Reproduced with permission.[74] Copyright 2021, Wiley-VCH. (d) Photo-responsive host-guest interfacial assembly of Alg-β-CD and AzoC12 in the presence of cosurfactants, i.e., PVA and Span 60. TEM images of Alg-β-CD/AzoC12 assemblies (e) before UV-irradiation, (f) under UV-irradiation, and (g) after visible light-irradiation. (d-g) Reproduced with permission.[129] Copyright 2023, Elsevier.

4.1.2 Thermo-responsive structures

The idea of developing temperature-responsive structured liquids and emulsions is particularly interesting as the temperature can be readily cycled in real-life scenarios, and such a system causes next to no changes in the chemical composition of materials.[121, 124] The most common way to achieve thermal-responsive systems at the liquid-liquid interface is to functionalize nanoparticles with thermal-responsive polymers, e.g., Poly(N-isopropylacrylamide) (PNIPAM) and its copolymers, that showcase lower critical solution temperature (LCST).[124, 131-133] Such functionalized nanoparticles are generally interfacially active at room temperature. However, when the temperature surpasses the LCST, the thermally responsive polymers become dehydrated, and the system destabilizes as a result of particle fluctuations at the liquid-liquid interface.

In this regard, thermo-responsive core-shell nanoparticles with a starch core and thermo-responsive polymer brush shell were introduced to stabilize Pickering hexane/water emulsions.[134] To synthesize thermo-responsive nanoparticles, the starch nanoparticles were first seeded with bromine (Br-SNP) and then grafted by PNIPAM through surface-initiated single electron transfer living radical polymerization (SI-SET-LRP) to get SNP-g-PNIPAM. The interfacial tension measurements showcased that pure starch nanoparticles seeded with bromine have no interfacial activity. However, after PNIPAM grafting, the resulting core-shell nanostructures significantly reduced the IFT between hexane and water and stabilized the Pickering emulsions. This Pickering system was stable at room temperature; however, it became completely unstable at temperatures higher than LCST due to the formation of nanoparticle clusters. Interestingly, the system was cycled to re-form stable Pickering emulsions by reducing the temperature below LCST, when the nanoparticle aggregates disappeared and SNP-g-PNIPAM regained their interfacial activity.

In another study, temperature-sensitive Janus silica nanoparticles featuring one silanol and one PNIPAM side were developed to stabilize a thermally responsive oil/water Pickering emulsion.[135] The efficacy and thermal responsiveness of these Janus silica nanoparticles in stabilizing tetradecane/water and crude oil/water systems were assessed compared to symmetric PNIPAM-modified silica nanoparticles. Strikingly, Janus nanoparticles exhibited a higher transition temperature (~50 °C) at which a stable emulsion deteriorated, attributed to their superior hydrophilicity arising from the presence of silanol on one side. Beyond this temperature, the disruption of hydrogen bonds and the dehydration and collapse of PNIPAM chains result in the de-emulsification of the system.

More interestingly, Yu et al.[136] synthesized dual-responsive colloidal supramolecular microcapsules with both thermo- and photo-responsive properties by employing a droplet-based microfluidic approach. The microcapsules were formed by combining Methyl viologen-bearing colloidal particles (MCP) grafted with thermal-responsive PNIPAM, along with cucurbit[8]uril, and the photo-responsive Azo-terminated PVA (Azo-PVA). When the system's temperature exceeds the LCST of PNIPAM, the microcapsule's shell collapses, which creates larger inter-particle gaps and facilitates the release of the encapsulated cargo. Simultaneously, the incorporation of AP imparts photo-responsiveness to the microcapsules. Upon exposure to UV light, the photoisomerization of Azo units induces the detachment of supramolecular complexes from the interface, resulting in cargo release.

It is worth noting that the abovementioned studies were all designed based on the LCST of thermally responsive polymers, where the resulting emulsions remain stable at room temperature but undergo de-emulsification at elevated temperatures beyond the LCST. However, Ranka et al.[137] reported a system that operates in the reverse direction, with the developed thermally responsive emulsions remaining stable at high temperatures and degrading at room temperature. In their study, a stable emulsion system was created using silica nanoparticles stabilized by schizophrenic di-block copolymers comprising poly(N-isopropyl methacrylamide) (PNIPMAM) as the LCST block (42 °C) and poly(sulfobetaine methacrylamide) (PSBMA) as the upper critical solution temperature (UCST) block (16 °C). At room temperature, both blocks exhibited hydrophilic and water-soluble characteristics, causing the decorated nanoparticles to have a high affinity for water molecules, display no surface activity, and fully disperse into the water phase. However, at an elevated temperature of 65 °C, the N-alkyl methacrylamide on the LCST block underwent dehydration, competing with the hydration of the polyzwitterionic block on the UCST block. This dynamic interplay resulted in the formation of interfacially active nanoparticles capable of stabilizing an oil-in-water emulsion at higher temperatures, as illustrated in Figure 22a. Such a system holds potential for various applications, including enhanced oil recovery, where an emulsion system can be formed at elevated temperatures in oil reservoirs to effectively absorb oil. However, upon reaching the surface and experiencing reduced temperatures, the de-emulsification process occurs, facilitating oil-water separation without incurring additional costs for the emulsifier/oil/water separation process.

4.1.3 Electric-field responsive structures

As discussed before, the solid particles tend to adsorb at the liquid-liquid interface to minimize the interfacial energy between two immiscible liquids. When these particles reach the interface, they tend to interact with each other through capillary forces and electrostatic interactions. If the particles are uncharged, the well-known phenomenon of capillary-induced self-assembly can lead to the formation of solid particle clusters at the liquid-liquid interface, especially with particle sizes >10 μm. However, the presence of charged particles, due to various functional groups, significantly diminishes their ability to form a densely packed layer at the interface, as electrostatic repulsion forces come into play.[124]

In this regard, strategies such as applying an external electric field or introducing deep potential walls through electric screening have proven effective in suppressing the electrostatic repulsion forces between charged particles at the interface of two immiscible electrolyte solutions.[124] Su et al.[138] explored this theory, having designed a liquid-liquid system with mercaptosuccinic acid (MOA)-stabilized Au nanoparticles at the water/1,2-dichloroethane (DCE) interface. Their work demonstrated that the concentration of nanoparticles at the liquid-liquid interface could be reversibly controlled by applying a potential bias. Further strengthening this theory, Janjua et al.[139] conducted research on the assembly of micro-to-nanoscale particles with diverse shapes, e.g., rods, cubes, and spheres, at both liquid-liquid and air-liquid interfaces. They effectively tuned the assembly by changing the strength and frequency of the applied electric field. Together, these studies highlight the intricate interplay between capillary and electrostatic forces, offering insights into controlling particle behavior at liquid interfaces.

Bera et al.[140] also demonstrated that the interaction among nanoparticles at the liquid-liquid interface can be adjusted by applying a voltage across the interface. Their experimental system included 2 nm Au nanoparticles coated with positively charged trimethylammonium-terminated ligands (TTMA-Au nanoparticles) and two electrolyte solutions: water containing sodium chloride (NaCl) and dichloroethane containing bis(triphenylphosphoranylidene) ammonium tetrakis pentafluorophenyl borate (BTPPATPFB) (Figure 22b). In the first step, they performed interfacial tension measurements under different voltages. When the electric potential difference ($\Delta\phi^{w-o} = \phi(w) - \phi(o)$) between the aqueous (w) and organic (o) solutions remained negative, the calculated interfacial tension was similar to that of a pure water/organic system. This suggests that the nanoparticles tended to remain in the bulk phase, unable to reach the liquid-liquid interface to minimize interfacial energy. However, when a slightly positive $\Delta\phi^{w-o}$ was applied, for instance, +30 mV, the calculated interfacial tension markedly decreased due to nanoparticle assembly at the liquid-liquid interface. Such a voltage-dependent assembly of TTMA-Au nanoparticles was further validated using the grazing-incidence small-angle X-ray scattering (GISAXS) technique, as illustrated in Figures 22c-d. The findings revealed that, regardless of the applied electric potential, the particles consistently formed a hexagonal arrangement at the 2D interface. However, the distance between nanoparticles and the in-plane correlation length depend on the applied voltage and can be effectively controlled.

More recently, Russell and co-workers utilized an external electric field to manipulate the configuration of structured liquids formed by assemblies of NPSs at the liquid-liquid interface.[41] Within their system, an aqueous droplet containing carboxylated polystyrene nanoparticles was suspended in a bath containing silicon oil and PDMS-NH_2. Within this system, PDMS molecules diffused into the interface, converting the previously negative charge of the oil/water interface to a positive one by forming PDMS-NH_3^+ layers. This shift lowered the interfacial energy, thereby promoting the migration of functionalized polystyrene nanoparticles towards the interface. The carboxylic functional groups of the polystyrene nanoparticles were then deprotonated and electrostatically bonded to protonated amine groups of PDMS-NH_3^+. This process created ligand/nanoparticle assemblies at the interface, which, upon jamming, stabilized the water droplets and formed a solid-like skin around the droplet.

Upon applying an external electric field with a strength of 4.6 kV cm^{-1}, the water droplets deformed, adopting an ellipsoid shape with a larger surface area (see Figure 22e). With an increased surface area, more NPSs formed at the interface, expanding the solid skin around the droplet to cover the entire structure. Upon the removal of the electric field, the water droplet could not return to its original shape, as the newly expanded skin pinned the droplet to its ellipsoid shape. Interestingly, this ellipsoid shape remained stable over time, up to one month, and the droplet could not revert to its original form (Figure 22f). Additionally, it should be noted that in the absence of PDMS-NH_2 as a ligand, the deformed droplet returned to its original spherical shape after the removal of the external electric field, underscoring the role of NPS assemblies and jamming in stabilizing liquids in highly non-equilibrium configurations.

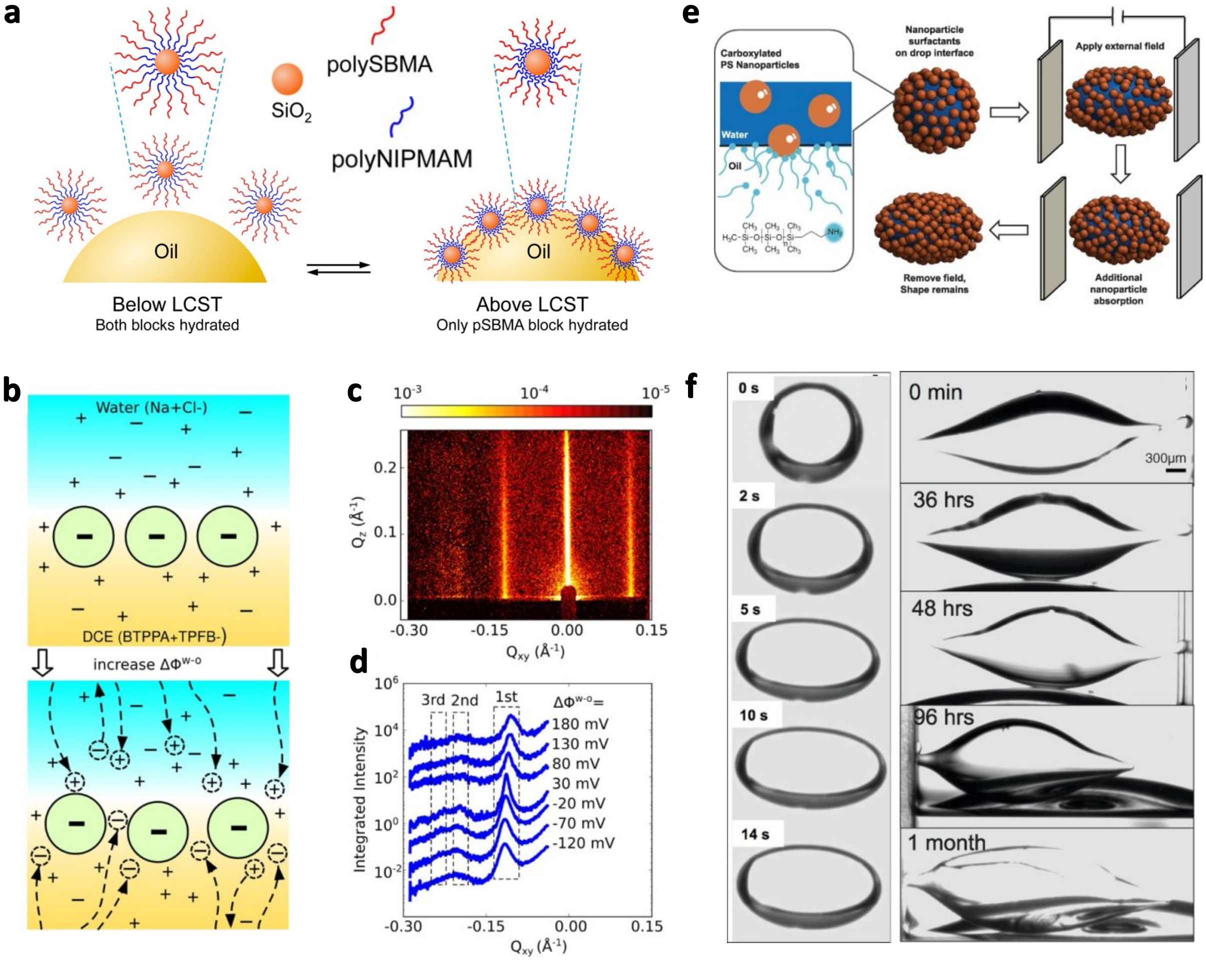

Figure 22: Thermo- and electric-field- responsive structured liquids. (a) Thermo-responsive Pickering emulsions based on silica nanoparticles stabilized by schizophrenic di-block copolymers comprising PNIPMAM as the LCST block and PSBMA as the UCST block. (a) Reproduced with permission.[137] Copyright 2017, American Chemical Society. (b) Controlling the assembly of positively charged TTMA-Au nanoparticles between two electrolyte solutions by applying a voltage across the interface. The electrolyte solutions are an aqueous suspension of NaCl and dichloroethane containing BTPPATPFB. The nanoparticles tended to remain in the bulk phase without applying voltage. However, with a slightly positive electric potential difference, the nanoparticles assemble at the liquid-liquid interface. (c-d) GISAXS analysis confirms the assembly of nanoparticles at the liquid-liquid interface upon applying different electric potentials at the interface. (b-d) Reproduced with permission.[140] Copyright 2014, American Chemical Society. (e) Using an applied electric field to deform structured liquids consisting of carboxylated polystyrene nanoparticles/PDMS-NH$_2$ NPSs. Upon applying an

electric field, the structured droplets deformed and adopted an ellipsoid shape with a larger surface area. (f) This ellipsoid shape remained stable over time. (e-f) Reproduced with permission.[41] Copyright 2013, American Association for the Advancement of Science.

4.1.4 Magnetic-field responsive structures

In general, magnetic materials can be categorized into three types: ferromagnetic, paramagnetic, or diamagnetic. Among all, ferromagnetic materials are the focus for developing responsive constructs, as they are highly responsive to magnetic fields and can retain their magnetization even after the external magnetic field is removed. However, in colloidal dispersions of ferromagnetic materials, the magnetic particles lose their magnetization upon removal of the external magnetic field, and the dispersion predominantly exhibits paramagnetic behavior. Such behavior is even more obvious in the colloidal dispersion of magnetic nanoparticles, where Brownian motion can easily displace nanoparticles and change their arrangement.[124, 141, 142] Nevertheless, if the magnetic nanoparticles are interfacially active, they can assemble and even jam at the liquid-fluid interface. In this scenario, the resulting emulsion or structured liquids can retain their magnetization even after the removal of an external magnetic field. This category of soft magneto-responsive materials is referred to as ferromagnetic liquid (FML) and has been the subject of several exceptional research and review articles.

Russell and his colleagues were pioneers in the creation of ferromagnetic structured liquids by utilizing the concept of NPS assembly and jamming at a liquid-liquid interface.[143] In their study, a suspension of carboxylated Fe_3O_4 in water was immersed in an inorganic phase containing POSS-NH_2 and toluene, resulting in the formation of structured ferromagnetic liquids. During immersion, the deprotonated carboxylic groups of magnetic nanoparticles and protonated amine groups of POSS-NH_2 electrostatically interacted, forming NPSs at the liquid-liquid interface. As the concentration of NPSs at the interface increased, i.e., achieved by increasing the magnetic nanoparticles' concentration in the bulk aqueous phase or reducing the pH, the NPSs effectively jammed at the interface, transforming the ferrofluid droplet into a structured ferromagnetic liquid droplet.

The transition from paramagnetic to ferromagnetic behavior was investigated through the analysis of magnetic hysteresis loops for identical ferrofluid droplets with and without POSS-NH_2 (Figure 23a). The magnetization, represented by the magnetic moment per unit volume (Ms), remained consistent between both samples, given the comparable total number of magnetic nanoparticles. However, the sample exhibiting interfacial jamming of magnetic NPSs displayed finite magnetic remanence (indicated by Mr, the residual magnetization in a material after the external magnetic field is removed) and coercivity (represented by Hc, the magnetic field strength required to demagnetize a material), which are key attributes of ferromagnetic materials. To further elaborate on this phenomenon, the study explored the influence of magnetic nanoparticle concentration in the bulk phase, pH variations, and droplet size. The results revealed that upon jamming, the resulting structured liquids exhibited ferromagnetic traits, a behavior further amplified by enhancing the surface coverage of magnetic NPSs at the liquid-liquid interface.

To further elaborate on this idea, the study mentioned above also focused on developing ferromagnetic liquid cylinders with a 2:1 aspect ratio through microfluidic injection of the aqueous phase containing functionalized magnetic nanoparticles into a toluene/POSS-NH_2 bath. Intriguingly, when subjected to a gradient magnetic field generated by the aluminum solenoid, the produced liquid cylinder demonstrated displacement within an all-liquid medium (Figure 23b). Additionally, as illustrated in Figure 23c, these ferromagnetic liquid cylinders exhibited behavior akin to solid magnets, showcasing N-N, S-S, and N-S dipole interactions. Notably, magnetized liquid cylinders that were initially separated by 1 mm were observed to attract each other through N-S dipole interactions, a phenomenon that holds potential in fields where the flowability of structured liquids and magnetic-like behavior resembling traditional solid magnets are crucial—such as in liquid robots, energy-dissipative assemblies, and programmable liquid constructs.

In another study, researchers used a structured liquid composed of oleic acid (OA)-coated Fe_3O_4 nanoparticles dispersed in mineral oil, combined with an aqueous suspension of amine-functionalized silica nanoparticles. This innovative mixture was utilized to develop a novel ferromagnetic liquid (FML).[5] In the absence of a magnetic field, OA-coated Fe_3O_4 nanoparticles assemble at the interface; here, OA undergoes deprotonation and acts as a ligand, electrostatically interacting with the protonated amine group of silica nanoparticles to form a solid-like interface at the liquid-liquid contact line. Upon applying an external magnetic field, the interface deforms, and additional assemblies of silica/magnetic nanoparticles occur at the interface, expanding the solid skin. This expanded skin retains the structured shape even after the removal of the magnetic field, and the deformed structure cannot return to its original shape (Figure 23d).

Interestingly, this category of magneto-responsive structured liquids was utilized as a carrier to trap, transport, and release other oil-based droplets immersed in the water phase (Figure 23e). It is worth noting that these droplets are inherently miscible with mineral oil, which is the main constituent of the developed magnetic structured liquids. However, due to the hydrophilic nature of capped groups of silica nanoparticles, which are densely packed at the interface of these structured liquids, the oil cargo cannot mix with the magnetic liquid constructs. Therefore, this class of magneto-responsive structures can be considered a novel category of all-liquid robots that can be used to transfer inorganic oil-based contaminants in water-based mediums.

Zhang et al.[144], on the other hand, developed magnetic-magneto all-oil reconfigurable structured liquids. Their system consists of a cationic/Lewis acidic dispersion of Fe_3O_4 in N, N-dimethylformamide (DMF), and a complementary Lewis basic PDMS-NH_2 polymer (5% w/w) as a solution in PDMS oil. The Lewis acid-Lewis base pairing of the PDMS-NH_2 and cationic Fe_3O_4 was reported to produce mesoscopic polymer surfactant at the liquid-liquid interface and significantly reduce the interfacial tension between two immiscible phases (Figure S8a). The assembly of these polymer surfactants at the interface was irreversible, as evident in the contraction test of a pendant drop. In this case, upon contracting a droplet of DMF/Fe_3O_4 in a bath of PDMS-NH_2/oil, obvious wrinkles were formed at the interface that remained stable over time. However, by the addition of a competitive zwitterionic ligand, i.e., 2-(3-butyl-1H-imidazol-3-ium-1-yl)acetate, to DMF, the system was able to return to its liquid state, as evidenced by the dissipation of wrinkles upon the contraction test of a pendant drop (Figures S8b-c). The authors reasoned that the transition from solid-like to liquid-like behavior at the interface is due to the reversible binding of the zwitterionic ligand to cationic Fe_3O_4, which was competitive with the binding of PDMS-NH_2 (Figure S8c).

The magnetic responsiveness and relaxation of surfactant assemblies upon applying an external magnetic field were also investigated in the same study. In this regard, placing the pendant droplet between two magnets of opposite polarity resulted in the displacement of the assembled structure in space, causing the encapsulated fluid to expand along the axis of the magnetic field. As a result, the interface was compressed along the axis normal to the field, and the interfacial tension was increased. For instance, when the concentration of the zwitterionic ligand was 2.5

mg/ml, the interfacial tension was increased from 4 to 5.6 mN/m upon applying the magnetic field. However, the interfacial characteristics of the droplet were returned to its original state when the external magnetic field was removed (Figure 23f).

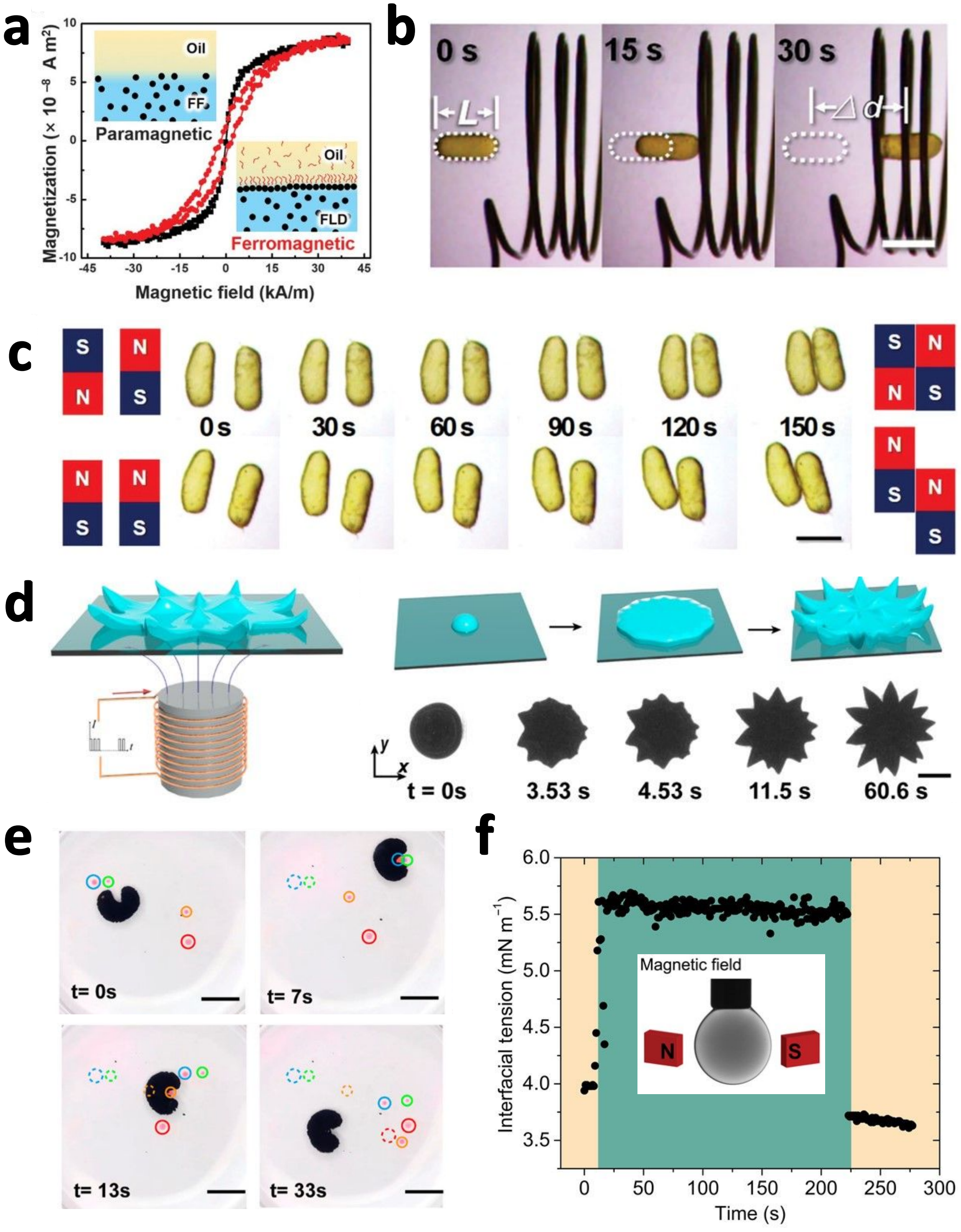

Figure 23: Magnetic-field responsive structured liquids. (a) The transition from paramagnetic to ferromagnetic behavior for the structured system containing carboxylated Fe_3O_4/POSS-NH_2

NPSs. (b) The developed ferromagnetic liquids can respond to a gradient magnetic field produced by an aluminum solenoid. (c) These ferromagnetic liquid cylinders also showcase N-N, S-S, and N-S dipole interactions similar to solid magnets. (a-c) Reproduced with permission.[143] Copyright 2019, American Association for the Advancement of Science. (d) A schematic illustration of a ferromagnetic liquid containing OA-coated Fe_3O_4 nanoparticles/amine-functionalized silica nanoparticles exposed to an external magnetic field. (e) This magneto-responsive structured liquid can be used as a carrier to trap, transport, and release other oil-based droplets immersed in the water phase. (d-e) Reproduced with permission.[5] Copyright 2022, American Chemical Society. (f) The magnetic responsiveness and relaxation of surfactant assemblies consisting of Fe_3O_4 and a zwitterionic ligand, i.e., 2-(3-butyl-1H-imidazol-3-ium-1-yl)acetate in DMF, and a complementary Lewis basic PDMS-NH_2 in PDMS oil. (f) Reproduced with permission.[144] Copyright 2018, American Association for the Advancement of Science.

4.2 Internal stimuli

4.2.1 pH-responsive structures

As discussed earlier, the assembly and jamming of NPSs at the liquid-liquid interface represent one of the most potent approaches for developing structured liquids. This process relies on the electrostatic interaction between nanoparticles and a complementary ligand at the interface. In this context, NPSs featuring electrostatic interactions between acidic groups of nanoparticles, such as carboxylic functional groups, and amine groups of ligands can undergo a reversible transition between protonated and deprotonated states in response to changes in pH. Therefore, these acid/base internal stimuli can be employed to control the state of structured liquids, transitioning from jammed to unjammed and introducing responsiveness to this class of soft functional materials.[14, 124, 145]

Russell and his colleagues were pioneers in developing pH-responsive structured liquids that capitalize on the reversible transition between protonated and deprotonated states of nanoparticles/ligands at a liquid-liquid interface.[8] Their system comprised an aqueous dispersion of carboxylated polystyrene nanoparticles within a nonpolar domain containing toluene/PDMS-NH_2. At a pH of approximately 5 or higher, the carboxylic functional groups of nanoparticles undergo deprotonation, engaging in electrostatic interaction with protonated amine groups of the ligands to establish stable NPSs at the liquid-liquid interface. However, reducing the pH to near or below the effective pKa of carboxylic functional groups prevents their deprotonation. This impedes the electrostatic interaction responsible for NPS formation, leading to the ejection of nanoparticles from the interface. The pH responsiveness of NPSs is intriguingly demonstrated by applying an external electric field (Figures 24a-b). Under this field and at high pH, droplets containing carboxylated nanoparticles deform into an ellipsoid with an aspect ratio of 1.78, as discussed in the previous section on the electric-field responsive structures. Upon removing the external field, the aqueous phase retains its ellipsoidal shape and does not revert to its spherical form. However, at lower pH values than the pKa of carboxylic functional groups, the droplet can be reconfigured to its spherical shape after removing the electric field. In this lower pH range, NPSs are terminated, and nanoparticles are pushed away from the interface, allowing the droplet to return to its original spherical shape with the lowest possible surface area.

The impact of pH on the formation and strength of NPSs was also emphasized in a liquid modeling project.[9] In this investigation, NPS formation relies on the electrostatic interaction between protonated amine-terminated polystyrene (PS-NH_3^+) and deprotonated sulfate-functionalized cellulose nanocrystals (CNC-OSO_3^-) at the liquid-liquid interface. At a pH of around 3, the assembly and jamming of NPSs are robust enough to yield all-liquid objects that replicate the shape and details of the mold within an external oil phase. However, with an increase in pH, the surface coverage of CNC at the interface diminishes, leading to deformation and a loss of fidelity in the molded structures.

In another study, pH-responsive oil-in-water Pickering emulsions were presented based on negatively charged SiO_2 nanoparticles and a zwitterionic carboxyl betaine surfactant as a stabilizer (Figures S9a-c).[146] Under acidic conditions, the ligand assumes a cationic state, adsorbing onto SiO_2 nanoparticles to stabilize the emulsions. However, with an increase in pH beyond 8.5, the ligands undergo a conversion to the zwitterionic state and subsequently desorb from the surfaces of the nanoparticles, leading to demulsification, as shown in Figure S9d.

Developing charge-reversible surfactants provides another avenue for fabricating pH-responsive emulsions. In a recent study, such a surfactant, namely $(CH_3)_2N\text{-}(CH_2)_{10}COONa$, was synthesized and coupled with silica nanoparticles to stabilize a smart pH-responsive n-octane-in-water emulsion.[147] Three scenarios for this system were considered based on pH (Figure 24c). At a high pH of 9.3, the surfactant adopts an anionic carboxylate state. This anionic state, coupled with negatively charged silica nanoparticles, co-stabilizes low-viscous oil-in-water emulsions. Conversely, under a low pH condition of 4.1, the surfactant transforms into a cationic form, creating amine salt that can render the previously negatively charged silica nanoparticles hydrophobic and stabilize a viscous oil-in-water Pickering emulsion. Furthermore, at a neutral pH (7.5), the surfactant undergoes conversion to a zwitterionic form. In this state, it weakly hydrophobized the silica particles, stabilizing oil-in-water Pickering emulsions characterized by large droplet size. Moreover, demulsification can be swiftly triggered by pH adjustments. As a result, this system exhibits the capability for intelligent and precise control of stability, viscosity, and droplet size in emulsions.

In another study, Luo et al.[148] devised Janus zwitterionic nanoplates capable of transitioning between a locked and unlocked state at oil/water interfaces by adjusting surface charges through pH changes. To achieve this, they initially functionalized negatively charged kaolinite nanoparticles with a cationic polymer, specifically poly[2-(dimethylamino)ethyl methacrylate] (PDMAEMA), followed by grafting with hydrophobic poly(lauryl methacrylate) (PLMA). These chemical moieties promote intermolecular attraction among nanoparticles in the locked state through the interaction of oppositely charged groups. Conversely, a robust electrostatic repulsion occurs when PDMAEMA polymers are fully protonated at low pH, representing the unlocked state.

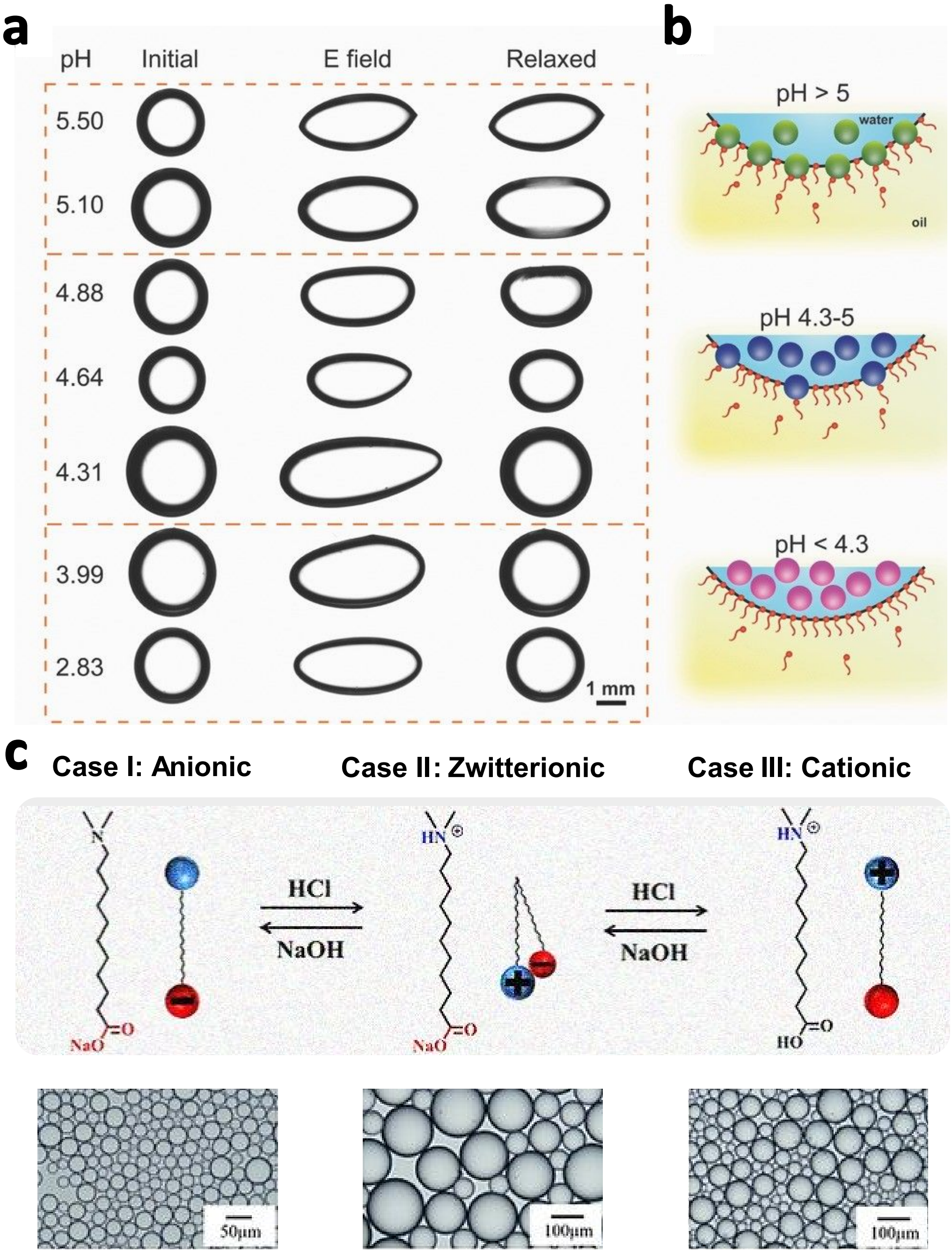

Figure 24: pH-responsive structured liquids. (a-b) The pH responsiveness of NPSs, i.e., PS-NH_2/CNC-OSO_3H, is demonstrated by applying an external electric field. (a-b) Reproduced with permission.[8] Copyright 2016, Wiley-VCH. (c) Various states of charge-reversible $(CH_3)_2N$-$(CH_2)_{10}COONa$ surfactants result in precise control over stability, viscosity, and droplet size in n-octane-in-water emulsions. (c) Reproduced with permission.[147] Copyright 2021, Wiley-VCH.

4.2.2 Redox-responsive structures

Redox reactions, also known as oxidation-reduction reactions, involve the transfer of electrons between reactants. In the context of structured liquids, nanomaterials or macromolecules with specific functional groups capable of undergoing oxidation or reduction present an opportunity to leverage redox potential as an internal stimulus. This capability allows for the dynamic control of assembly states at the liquid-liquid interface, transitioning between jammed and unjammed states.[2, 124] Despite being a relatively recent focus in interfacial assembly studies, redox-reconfigurable structured liquids and emulsions exhibit promising potential for future research, driven by their controllability and responsiveness. This potential gains further significance considering the well-explored landscape of redox reactions and material selections in areas like drug delivery and cancer therapies.[149, 150] In this regard, commonly utilized redox-responsive structures, including thioether, disulfide bond, selenium bond, and ferrocenyl, have been extensively examined in prior studies, laying a foundation for their seamless integration into the evolving field of structured liquids.[124]

Sun et al.[151] were pioneers in the development of redox-responsive structured liquids, focusing on the interfacial interaction between an electron-deficient acceptor dissolved in water and an electron-rich donor dissolved in toluene at a liquid-liquid interface. In their approach, a charge transfer interaction involving methyl viologen (MV^{2+} dissolved in water) and naphthalene-terminated poly-L-lactic acid (NT-PLLA dissolved in toluene) was employed to create an interfacial skin at the liquid-liquid interface (see Figure S10a). During the compression and relaxation test of a pendant drop, visible wrinkles formed at the interface, indicating the jammed state of these assemblies. However, the introduction of sodium dithionite ($Na_2S_2O_4$) as a reductant led to MV^{2+} accepting an electron and transforming into a radical cation in an electron-rich state, denoted as $MV^{+\bullet}$. In this reduced state, $MV^{+\bullet}$ is no longer an electron acceptor, preventing interaction with NT-PLLA and resulting in a relaxed and unjammed state at the liquid-liquid interface (see Figure S10b). Nevertheless, the reduced $MV^{+\bullet}$ can be oxidized and converted back to MV^{2+} by using sodium hypochlorite (NaClO) as the oxidant. As a result, the interfacial interactions between MV^{2+} and NT-PLLA can be revived, facilitating the reassembly and jamming of MV^{2+}/NT-PLLA at the liquid-liquid interface (Figures S10a-b).

Shortly after, the same research group developed redox-responsive all-liquid constructs based on ferrocene-terminated PLLA (Fc-PLLA) and β-cyclodextrin (β-CD) functionalized Au nanoparticles.[152] Normally, uncharged Fc is bound into the cavity of β-CD and forms NPSs through host-guest interaction at the toluene/water interface (Figure 25a). However, by oxidizing Fc into the ferrocene cation (Fc^+), host-guest interaction is disrupted, and NPSs are disassembled at the interface. As a result, the structured liquids lose their structure and adopt a more liquid-like behavior. This jamming/unjamming transition can be repeatedly cycled with the sequential addition of NaClO as the oxidant and $Na_2S_2O_4$ as the reductant. Interestingly, this redox-responsive host-guest interaction at the liquid-liquid interface was also combined with the concept of liquid-in-liquid printing to fabricate NPS-stabilized aqueous tubules in toluene (Figures 25b). As shown in Figures 25c-d, these aqueous tubules can be loaded with a cargo, here Rhodamine B, that can be released upon oxidizing Fc in a reconfigurable manner.

More recently, Yang et al.[153] have introduced reconfigurable structured liquids through the interfacial assembly and jamming of CNC-based NPS. Their approach hinged on electrostatic interactions between $CNC\text{-}OSO_3^-$ and ferrocenium-terminated polystyrene ($PS\text{-}Fc^+$) at the oil-water interface (see Figure 25e). Importantly, Fc^+ is responsive to various stimuli, including redox potential, pH, and voltage, offering multiple routes to control the assembly of NPS at the interface and cycle them from a jammed to an unjammed state. The pH-dependent interfacial activity of PS-Fc mirrors that observed with amine-functionalized ligands discussed in previous sections. In acidic conditions, PS-Fc undergoes protonation, facilitating its assembly at the interface and reducing the interfacial tension. However, increasing the pH through the addition of NaOH induces deprotonation, which significantly suppresses the interfacial activity of PS-Fc. This leads to the subsequent disruption of NPSs at the liquid-liquid interface. (Figure S10c). On the other hand, the redox responsiveness of CNC-OSO_3^-/ PS-Fc^+ NPS was analyzed by reducing the Fc^+ group to the Fc group using hydrazine hydrate (N_2H_4) as the main reduction agent. Furthermore, the easily achievable and repeatable electrochemical stimulus was also employed to reconfigure these structures, presenting a novel way to control and recycle structured emulsions (see Figure S10d).

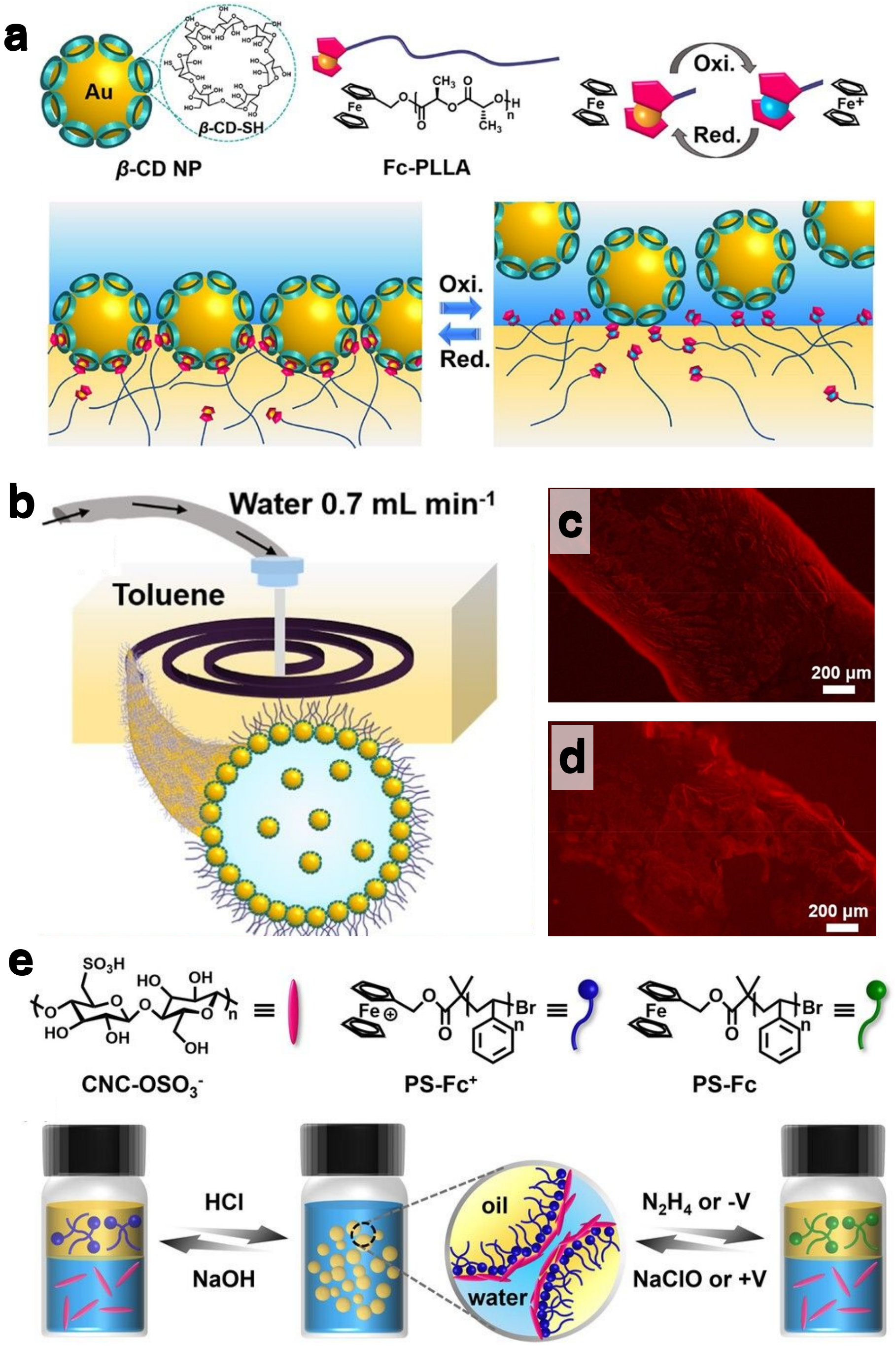

Figure 25: Redox-responsive structured liquids. (a) Redox-responsive all-liquid constructs based on Fc-PLLA and β-CD-functionalized Au nanoparticles. (b) This redox-responsive host-guest interaction at the liquid-liquid interface was also integrated with the liquid-in-liquid printing approach to make aqueous tubules stabilized by NPSs within toluene. (c) These aqueous tubules have the capacity to encapsulate a cargo, such as Rhodamine B. (d) This cargo can be selectively

released through the oxidation of Fc in a reconfigurable manner. (a-d) Reproduced with permission.[152] Copyright 2021, American Chemical Society. (e) Reconfigurable structured liquids based on the interfacial assembly and jamming of CNC-based NPS. This system is responsive to various stimuli, including redox potential, pH, and voltage, offering multiple routes to control the assembly of NPSs at the interface and cycle them from a jammed to an unjammed state. (e) Reproduced with permission.[153] Copyright 2023, Wiley-VCH.

5 Applications

5.1 All-liquid systems

5.1.1 All liquid electronics

The development of highly conductive structured liquids using MXene and intrinsically conductive polymers like PEDOT:PSS has opened up numerous opportunities in the fabrication of all-liquid electronics. This emerging field presents a viable alternative to traditional solid-based electronics and sensors, offering new possibilities for innovation and design. Such a research trend was first realized by developing 3D liquid-in-liquid printing of aqueous suspension of MXenes, i.e., $Ti_3C_2T_x$, into a nonpolar silicon oil bath containing n-butylamine ($CH_3(CH_2)_3NH_2$).[76] The electrostatic interaction between positively charged ligands and negatively charged MXene nanosheets was reported to stabilize liquid threads and fabricate highly conductive 3D complex geometries that are not achievable through traditional metal-based conductors or even direct ink writing of synthetic materials (Figures 26a-c).

Later on, capitalizing on 3D liquid-in-liquid printing of MXene-based aqueous suspension in a nonpolar domain containing butylamine and toluene, Zettl and co-workers demonstrated the first reported all-liquid on-and-off switches and sensors.[15] In their work, they demonstrated that a stabilized aqueous stream of MXene can be used to connect to electrodes and conduct electricity, similar to what we see for normal metal-based connectors. However, the liquid connectors can easily be cleaved to turn off the circuit and then get back into the initial state by only adding a few droplets of MXene aqueous suspension to repair the MXene tubular wires (Figure S11a). It is worth noting that although the idea of all-liquid circuits seems impractical and in its infant stage, such a system provides an opportunity to reconfigure electronic systems indefinitely and even provides a pathway to recycle electronics easily at the end of their life.

In another interesting study, Yan et al.[16] explored the interfacial assembly of polyelectrolytes to develop structured-liquid batteries. The interfacial assembly was achieved in a biphasic system containing two aqueous phases: one containing dextran and poly(sodium 4-styrenesulfonate) (PSS−Na) and the other containing PEG and poly (diallyldimethylammonium chloride) (PDADMA−Cl). As active materials, cationic methyl viologen was added to the dextran phase to form the anolyte, while the catholyte was designed by the addition of ferrocyanide to the PEG phase (Figure S11b). Upon reduction, methyl viologen forms a radical cation, whereas, upon oxidation, ferrocyanide changes its oxidation state but remains anionic. This dual behavior enables the developed batteries to store energy and release it on demand effectively.

To regulate the formation of ion pairs and slow down the rate of crossovers within the cell, NH_4Cl was added to the system. This adjustment allowed the liquid batteries to maintain functionality over hundreds of cycles. Crucially, the power output of these designed batteries was comparable to that found in biological circuits and sensors, highlighting the significant potential of this interfacially driven energy storage system for future applications.

5.1.2 Environmental remediation using all-aqueous structured liquids

The use of structured liquids for absorption, separation, and catalytic reduction of environmental pollutants is still in its infancy, with many possibilities yet to be explored. In this context, recent advancements, such as the development of aqueous liquid robots designed to capture and catalytically reduce environmental pollutants, highlight the potential of this emerging field.[18] These liquid robots typically consist of a biphasic system containing two aqueous phases, with one phase referred to as the aqueous ink (10 wt % 10,000 g/mol Dextran and 5 wt % 8,000 g/mol PEG) being printed inside an external bath (25 wt % 8,000 g/mol PEG).

To stabilize the liquid threads of the ink in the external bath, nanoparticles or polymers with complementary functional groups were added to each phase, resulting in interfacial complexation that stabilized these non-equilibrium shapes. Specifically, the addition of negatively charged carboxyl-functionalized polystyrene (PS-COOH) nanoparticles to the ink and positively charged poly(allylamine hydrochloride) (PAH) to the bath phase was reported to stabilize these nanoequilibrium shapes and enable all-aqueous liquid-in-liquid printing. In this context, the tubules' walls consist of tiny colloidosomes, resembling blood vessels lined with endothelial cells (Figures 26d-f). These colloidosomes are formed through the stabilization of interfacial phase-separated small droplets using oppositely charged nanoparticles and polyelectrolytes.

Notably, this method is versatile, as various nanoparticles with different functionalities were employed to stabilize these all-aqueous systems. Moreover, the system can serve as a carrier for various materials to perform diverse reactions in-situ within the printed structures. For example, the interfacial complexation of Fe_3O_4 nanoparticles and GO nanoflakes with abundant carboxylic functional groups demonstrated the fabrication of magnetoresponsive all-aqueous constructs capable of gripping, transporting, and releasing objects in an external aqueous medium.

Furthermore, the addition of TiO_2 to the ink phase of these magnetoresponsive liquid constructs led to the development of a programmable liquid robot capable of absorbing and catalytically removing rhodamine B, an environmental pollutant. In this scenario, the fabricated liquid robots can move to a specific location using an external magnetic field, absorb the pollutants, and, upon exposure to UV light, degrade the pollutants due to the catalytic activity of TiO_2 (Figure 26g).

The all-aqueous liquid robots discussed here offer an effective and environmentally friendly approach to water purification. Additionally, it can initiate target reactions as needed in limited spaces, such as biomedical applications like targeted photothermal therapy for tumor cells within confined areas in vivo.

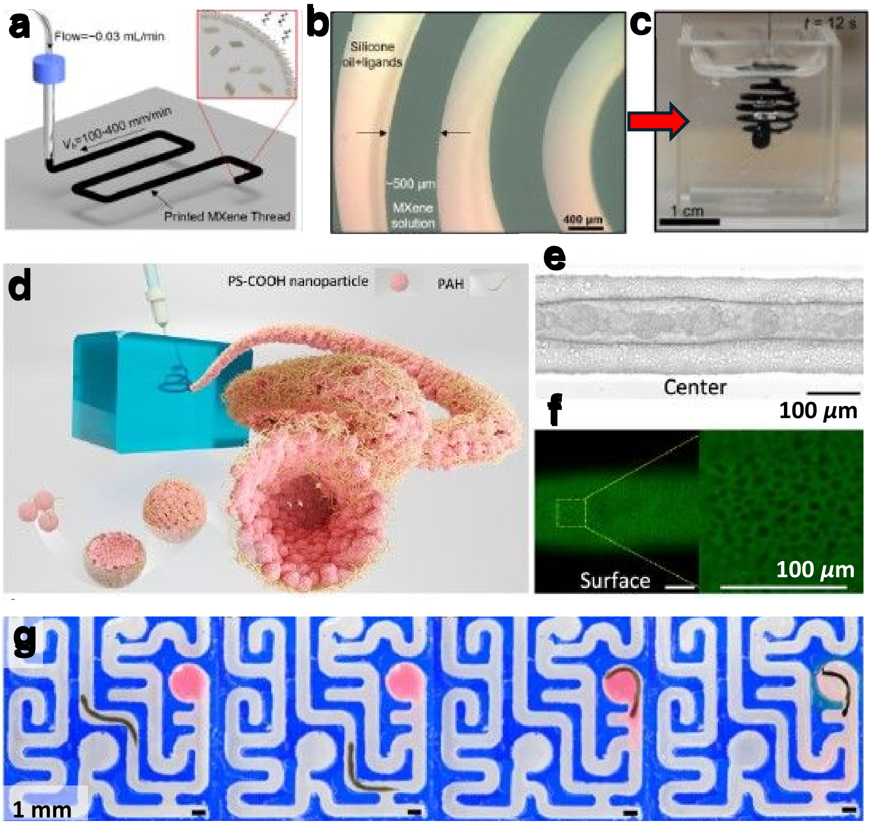

Figure 26: (a) The electrostatic interaction between deprotonated ligands (positively charged) and negatively charged MXene nanosheets stabilizes conductive liquid threads, and (b-c)

fabricates complex geometries that can be used for all liquid electronics. (a-c) Reproduced with permission.[76] Copyright 2019, American Chemical Society. (d-f) The electrostatic interaction of negatively charged PS-COOH nanoparticles with positively charged PAH stabilizes the aqueous stream of Dextran/PEG into an aqueous bath of PEG. The printed tubules' walls consist of tiny colloidosomes. (g) Water-in-water printing is versatile, and various nanoparticles, including GO and Fe_3O_4 with magnetic characteristics and TiO_2 with photocatalytic activity, were integrated into this printing approach. The resulting magnetoresponsive liquid constructs were used to absorb and catalytically remove rhodamine B, an environmental pollutant. In this scenario, the fabricated liquid robots can move to a specific location using an external magnetic field, absorb the pollutants, and, upon exposure to UV light, degrade the pollutants due to the catalytic activity of TiO_2. (d-g) Reproduced with permission.[18] Copyright 2022, American Chemical Society.

5.1.3 All-liquid microreactors

Structured liquid microfluidic devices and reconfigurable droplet systems have recently been utilized to develop all-liquid microreactors for conducting chemical reactions with high efficiency and control. A recent study detailed the creation of these reactors through 3D liquid-in-liquid printing, where an aqueous suspension of nanoclay was introduced into a nonpolar bath containing amine-functionalized PDMS (as described in section 3.2.3).[10] In this system, anionic nanoclays enable the anchoring of cationic molecules, enzymes, and nanoparticles to the walls of the all-liquid microfluidic channels, presenting a range of possibilities for chemical reactions and separations. For example, using this approach, various cationic species, including horseradish peroxidase (HRP), cationic dyes like rhodamine 6G and methylene blue, and CTAB-modified Pt nanocrystals, were selectively attached to the inner walls of printed channels, while anionic chemical species passed through the liquid channels without adhering to the walls (Figures 27a-c).

Capitalizing on this strategy, all-liquid microfluidic devices containing cationic HRP were also utilized for a variety of reactions.[10] For instance, when a solution containing 3,3′,5,5′-tetramethylbenzidine (TMB) and hydrogen peroxide (H_2O_2) was passed through the fabricated channels, the TMB molecules oxidized and transformed into a yellow-colored diimine product, easily traceable in the microchannels (Figure 27d). In another instance, a solution of phenol, 4-aminoantipyrine (4-AAP), and H_2O_2 was pumped through the microfluidic device, leading to the oxidative coupling of phenol and 4-AAP, producing a red-colored quinone-imine conjugate that could also be visually tracked in the liquid channels (Figure 27e). Considering the success of these reactions, all-liquid microfluidic devices with exceptional reconfigurability can be envisioned for future applications in designing chemical logic and learning platforms.

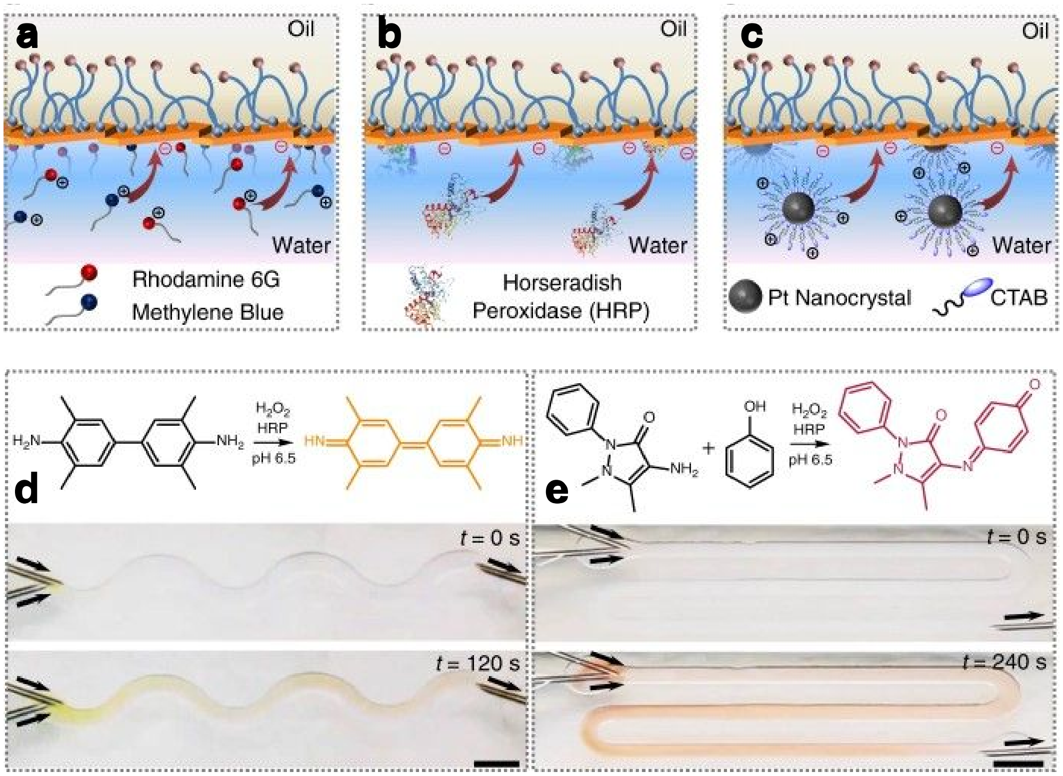

Figure 27: (a-c) Various cationic species can be selectively anchored to the walls of all-liquid microfluidic channels composed of amine-functionalized PDMS/nanoclay NPSs. (d) The

oxidation of TMB in the presence of H_2O_2 yielded a yellow-colored diimine product. (e) The oxidative coupling of phenol and 4-AAP produced a red-colored quinone-imine conjugate that could also be visually tracked in the liquid channels. (a-e) Reproduced with permission.[10] Copyright 2019, Nature Publishing Group.

In another interesting study, Liu et al.[21] developed all-liquid microfluidic devices with multilayer walls for enzyme immobilization (Figure 28a). In their study, aqueous tubes of CNCs were first stabilized and printed inside a nonpolar bath containing POSS-NH_2. The pH of the aqueous suspension was set at 3 to ensure strong electrostatic interaction between the deprotonated CNC sulfate ester groups ($–OSO_3^−$) and protonated oligomeramine groups (NH_3^+) at the oil/water interface. This electrostatic interaction forms CNC-based NPS at the liquid-liquid interface, which, upon jamming, stabilizes the liquid threads in silicone oil, thus creating microfluidic devices.

Upon preparing CNC-based liquid channels, a continuous flow system was designed by connecting each side of a channel to a syringe pump. In such a system, fluid can be injected from one side of the channel and collected from the other side. Then, chitosan (CH) and hyaluronic acid (HA) layers were alternately deposited on the inner side of the channel to fabricate a microfluidic device with a multilayer wall. The deposition process involved first washing the channel with water (pH ~ 3) and then injecting a suspension of CH into the fabricated channel. In this case, the electrostatic interaction of the cationic CH and the anionic CNC layer was reported to deposit a layer of CH on top of the CNC interfacially driven layer. After the deposition of the CH layer, the microfluidic system was rinsed with water (pH ~ 7), and then a suspension of HA was injected into the channels to form an HA layer on top of the CH layer. This deposition process was repeated several times to generate microfluidic channels with walls containing alternating CH/HA layers.

The developed CH/HA multilayer provides an excellent platform for immobilizing the HRP enzyme. Prior to enzyme injection, the microchannels were washed with 2-(N-morpholino)ethanesulfonic acid (MES) buffer solution. Subsequently, a MES buffer solution containing HRP is injected into microchannels to optimize enzyme adsorption. Following this, the microchannel is washed with pure MES buffer solution to eliminate unattached HRP. To assess the immobilized HRP on the CH/HA multilayer, lissamine rhodamine B sulfonyl chloride-labeled HRP (LRSC-HRP) was synthesized, and its attachment to the inner wall of microchannels was examined by laser scanning confocal microscopy, as shown in Figures 28b-c.

Upon immobilizing HRP on the multilayer, the multilayer fluidic system was used as an enzymatic reactor, where o-phenylenediamine (OPD) was oxidized by H_2O_2 to form brown 2,3-diaminophenazine (DAP). In this reactor, HRP acted as a catalyst, influencing the kinetics and efficiency of the reaction (Figure 28d). Interestingly, increasing the number of deposited layers in the microchannels significantly enhanced the catalytic performance of HRP (Figures 28e-f). Overall, this strategy for designing all-liquid microfluidic devices is simple and widely applicable, addressing key impediments faced by all-liquid microreactors and opening new applications in the field of chemical biotechnology.

The aforementioned all-liquid microfluidic devices rely on a nonpolar bath, e.g., silicone oil, which limits their application in certain scenarios. To tackle this challenge, Xie et al.[154] developed all-aqueous microfluidic systems based on a stabilized water/water interface. In their study, an aqueous solution of dextran with poly(sodium 4-styrenesulfonate) (PSS) was printed in an aqueous bath of PEG containing poly(diallyldimethylammonium chloride) (PDADMAC). It is important to note that the dextran solution and PEG phase are immiscible and do not diffuse into each other. In this scenario, the interfacial complexation of oppositely charged PSS and PDADMAC was reported to generate a solid-like skin that stabilizes the aqueous suspension of dextran and suppresses Plateau-Rayleigh instabilities.

The developed all-aqueous printed channels were used as microreactors for chemical synthesis and separation. For instance, continuous compartmentalized reactions can be performed in these aqueous devices. In this scenario, a suspension of dextran containing urea, HRP enzyme, and H_2O_2 was directed through the printed microchannels, while urease and 2,20-azino-bis(3-ethylbenzothiazoline-6-sulphonic acid) diammonium salt (ABTS) were added to the external PEG bath (Figure S12a). In the first reaction, urease catalyzes the hydrolysis of urea into carbon dioxide and ammonia. To validate this reaction, the pH values of both aqueous phases were monitored. After continuous urea hydrolysis for 1 hour, the pH in the PEG phase increased from 4 to 8.5, while the pH in the dextran phase showed a smaller increase due to the diffusion of ammonia (Figures S12b-c). In a second reaction, ABTS was oxidized into $ABTS^+$ using H_2O_2 as the oxidizing agent and HRP as the catalyst. Here, the 415 nm peak of $ABTS^+$ in the ultraviolet-visible (UV-Vis) spectrum was only detected in the dextran solution, not in the PEG phase, confirming the compartmentalization of reactions (Figure S12d). Overall, the ability of these microfluidic devices to simultaneously perform compartmentalized and separate reactions represents a significant innovation not yet seen in other fluidic devices.

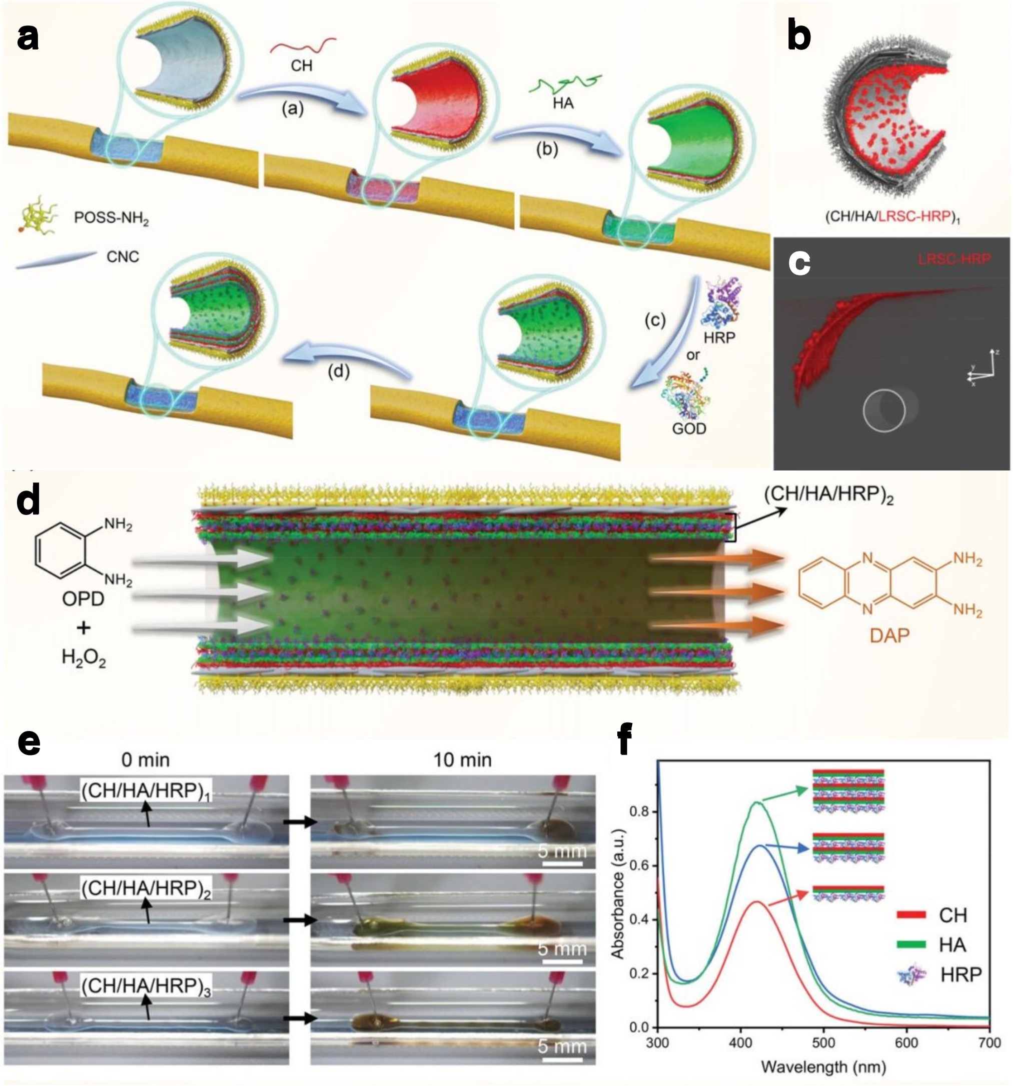

Figure 28: (a) Fabrication of all-liquid microfluidic devices with multilayer walls for enzyme immobilization. (b-c) Examination of LRSC-HRP enzyme immobilization on microchannel walls using laser scanning confocal microscopy. (d) Immobilizing HRP on the multilayer enabled the use of the multilayer fluidic system as an enzymatic reactor, where OPD was oxidized by H_2O_2 to form brown DAP. It is worth noting that HRP acted as a catalyst in this reactor, influencing the kinetics and efficiency of the reaction. (e-f) Increasing the number of deposited layers in the microchannels improved the catalytic performance of HRP significantly. (a-f) Reproduced with permission.[21] Copyright 2022, Wiley-VCH.

In addition to microfluidic devices, structured liquid droplets and bead systems also offer novel opportunities for designing all-liquid microreactors.[155] Yang et al.[20] explored this concept by developing multi-responsive structured liquid droplets that can be directed to specific locations with external stimuli, assemble on demand, and perform chemical reactions. These structured droplets were formed through electrostatic interactions between Au nanoparticles decorated with 11-mercaptoundecanoic acid (MUA) featuring a –COOH termination and oleic acid (OA) functionalized Fe_3O_4 or PbS nanoparticles. As explained before, the electrostatically driven assembly and jamming of these nanoparticles at the interface generated a solid-like skin that stabilized these structures in non-equilibrium shapes (Figure 29a).

In their experiments, the droplets were prepared using a water/ethylene glycol mixture, while the external bath consisted of a dispersion of Fe_3O_4 or PbS nanoparticles in 1,2-dichlorobenzene (DCB) or a mixture of toluene and DCB with a density of 1.05 g/ml. In these solvents, aqueous droplets were buoyant and localized slightly below the surface rather than rising and spreading to it. Furthermore, these droplets responded to an external magnetic field and formed ordered assemblies in high-field regions. However, due to the presence of a solid-like skin encasing the droplets, they remained distinct from each other without mixing or exchanging contents for at least several days. This characteristic ensures stability and containment in applications requiring controlled interactions.

More interestingly, these structured droplets were also light-responsive and could be moved by applying an external laser source, specifically using a 660 nm diode laser. Under laser irradiation, the fabricated droplets moved towards the beam and formed densely packed configurations, as illustrated in Figure 29b. Switching off the laser led to droplet disassembly within approximately 20 seconds. This cycle of assembly and disassembly could be repeated numerous times without observable changes in droplet behavior.

On the other hand, external stimuli such as electric fields and laser heating have been used to weld these droplets together, creating nonspherical shapes and allowing the contents of different droplets to mix. These techniques, combined with external magnetic and optical fields, facilitated the development of reconfigurable and programmable all-liquid microreactors. In these systems, various reactants can be loaded into separate droplets and mixed on demand to carry out specific reactions, enhancing the versatility and functionality of microfluidic platforms. Two experiments were performed to showcase this potential and highlight the importance of rapid mixing in all-liquid microreactors. In the first scenario, two droplets containing high-viscosity solutions of Congo red or HCl were moved toward each other and fixed using an external magnet. Upon irradiation with an external laser source and heating of the droplets, the contents of these droplets rapidly mixed together over a few minutes, as shown in Figure 29c. In the other experiment, two droplets carrying $CoCl_2$ and 2-methylimidazole were brought into contact by laser light and fused by an electric field, i.e., short pulses of an electric field produced by a Zerostat gun. Upon diffusion and mixing of the droplets' contents, zeolitic imidazole framework 67 (ZIF-67) was formed, depicted by the blue color in Figure 29d.

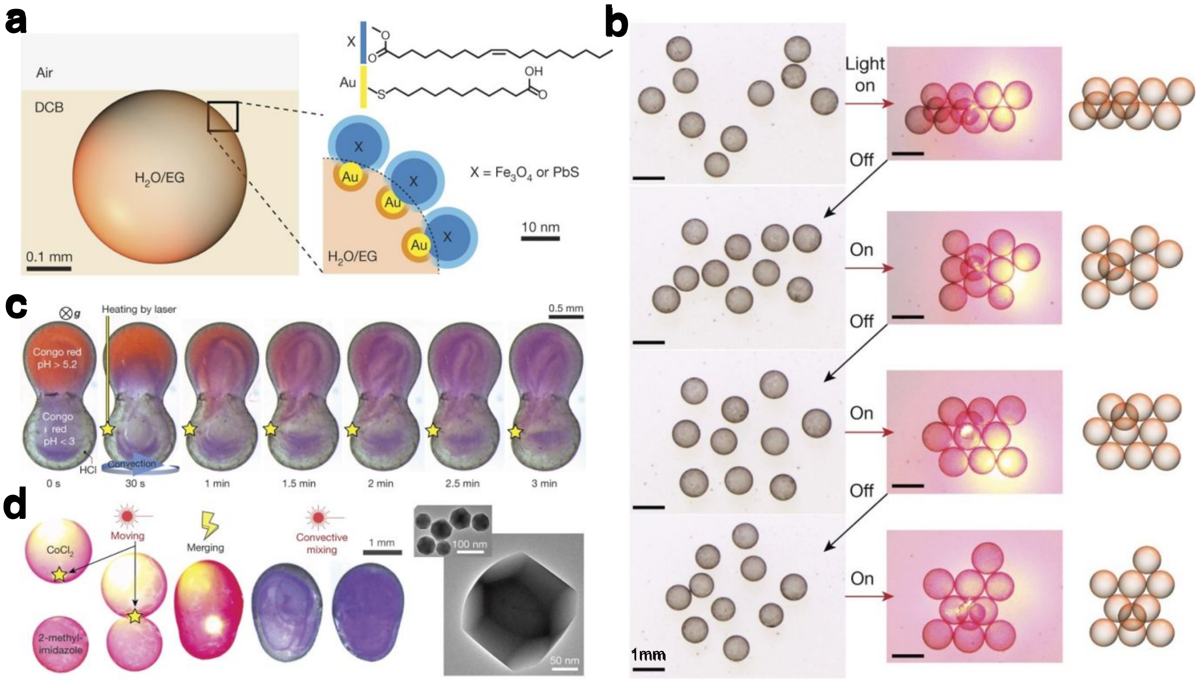

Figure 29: The developed structured droplets are stabilized through the electrostatic interaction of different nanoparticles with complementary functional groups at the liquid-liquid interface. (b) The developed structured droplets were light-responsive. Under laser irradiation, the droplets moved towards the beam and reversibly assembled into closely packed structures. (c) Two structured droplets containing high-viscosity solutions of Congo red or HCl were moved toward each other by an external magnetic field and then welded together by heating the contact point using a laser source. (d) Two droplets carrying $CoCl_2$ and 2-methylimidazole were brought into contact by laser light and welded by an electric field to form ZIF-67. (a-d) Reproduced with permission.[20] Copyright 2018, Nature Publishing Group.

In another intriguing study, Shi and colleagues demonstrated a multi-responsive and reconfigurable droplet network with significant potential for developing all-liquid microreactors.[17] In their system, an aqueous solution containing methyl viologen functionalized sodium carboxymethylcellulose (CMC-MV^{2+}) and CB[8] interacted with an oil phase consisting of azobenzene-terminated poly-L-polylactic acid (Azo-PLLA) and toluene. At the oil/water interface, the host CB[8] could bond with other guest molecules, MV^{2+} and Azo, stabilizing an aqueous droplet in the nonpolar phase. Interestingly, the CB[8] surfactants generated at the liquid-liquid interface have cavities inside their structures, allowing the exchange of materials between two different droplets that come into contact with each other (Figure 30a). As a result, compared to previous all-liquid microreactor systems, the droplets stabilized by CB[8] surfactants are more versatile. A simple manual compression of these droplets towards each other can initiate a reaction without the need for external stimuli, such as an electric field or heating with a laser, as described in the previous study.

The adaptability of this droplet network as a new generation of all-liquid microreactors has been demonstrated through various reactions, where droplets carrying different reactants are simply pushed toward each other to initiate the reaction. In the first example, two droplets containing ferric chloride ($FeCl_3$) and potassium thiocyanate (KSCN) were brought together, resulting in the formation of ferric thiocyanate ($Fe(SCN)_3$) with a deep red color (Figures 30b-c). In another example, this droplet system was used to synthesize ZIF-67 in-situ by connecting two droplets containing $CoCl_2$ and 2-methylimidazole (2-MI), respectively (Figures 30d-e). Furthermore, cascade reactions were also performed using this all-liquid microreactor system. For this purpose, a droplet containing glucose was contacted by another droplet containing HRP enzyme and glucose oxidase (GOD). When glucose and GOD react together, H_2O_2 forms in the system. The presence of H_2O_2 was visualized by adding another droplet containing o-phenylenediamine (OPDA) to the system. Due to the presence of H_2O_2, OPDA is oxidized to 2,3-diaminophenazine (DAP), and a yellow-green substance is produced in the droplets (as shown in Figures 30 f-g). Overall, such an all-liquid and reconfigurable microreactor system, which requires only a simple compression of droplets together to initiate a reaction, may find several applications in fields such as chemical synthesis, biotechnology, and drug discovery, offering a versatile platform for efficient and controlled reactions in a compact and flexible setup.

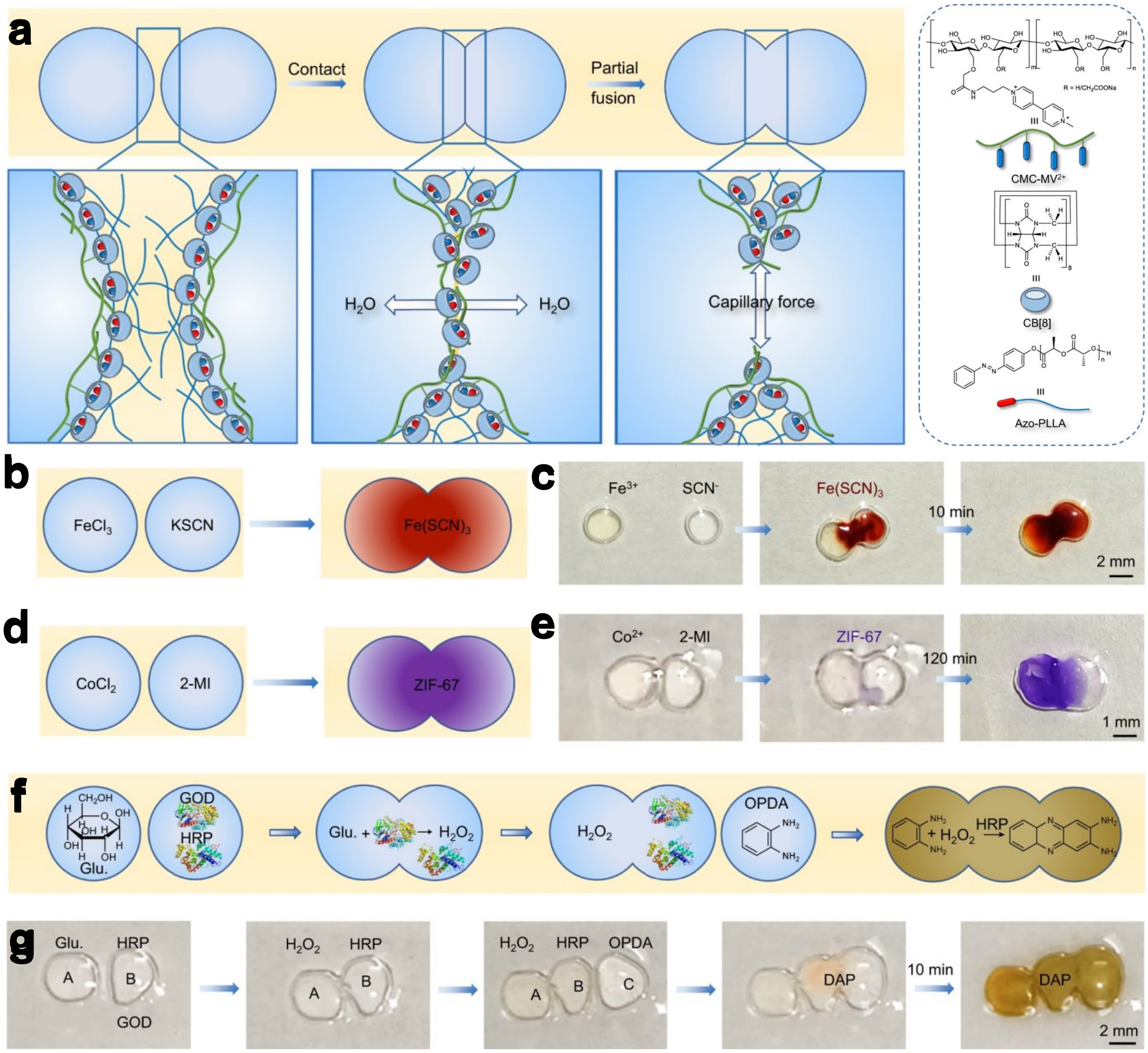

Figure 30: (a) The all-liquid microdroplets form through the interfacial complexation of CB[8], CMC-MV^{2+}, and Azo-PLLA at the oil/water interface. Upon a simple compression of these droplets together, their cargo can easily mix together and initiate a reaction. (b-c) Formation of Fe(SCN)$_3$ with a deep red color upon contacting two droplets containing FeCl$_3$ and KSCN, respectively. (d-e) Synthesis of ZIF67 in all-liquid microreactors. (f-g) Cascade reactions were performed by contacting three droplets with different cargos, i.e., droplet A containing glucose,

droplet B containing HRP enzyme and GOD, and droplet C containing OPDA. (a-g) Reproduced with permission.[17] Copyright 2024, Nature Publishing Group.

5.2 From liquid-liquid interface to functional thin film fabrication

The interfacial assembly of nanoparticles and macromolecules at a liquid-liquid interface, whether in a solid-like or dynamic assembly, offers a versatile pathway for developing functional thin films.[156] This versatility allows for the programming of both the packing order and functionality of the final constructs through careful selection of nanoparticles, macromolecules, ligands, and surfactants. This concept was recently utilized to fabricate soft membranes and complex 3D geometries based on the in-situ growth of bacterial nanocellulose (BNC) at the oil/water interface.[157] In the fabrication of BNC thin films, the culture medium containing essential nutrients for bacterial growth is embedded in the aqueous phase, while the oil phase (e.g., perfluorodecaline (F-decalin), silicon oil, dodecane) positioned above the culture medium, facilitates oxygen transport toward the aqueous phase. Consequently, the BNC membrane is produced at the oil/water interface by the microorganisms (Figures 31a-b). These developed thin films exhibit features similar to those fabricated at the air/water interface, with acceptable mechanical and structural characteristics. Notably, the use of oil in this method significantly suppresses water evaporation during the long fabrication process, reducing the chance of evaporation-induced shrinkage and surface wrinkles in the fabricated thin films.

The versatility of this interfacially driven fabrication method was further demonstrated by constructing multi-layer biscuit-like composites comprising two compact and ordered layers at the bottom and top, with a middle section dependent on the culture medium's characteristics. As depicted in Figure 31c, the cell designed for these experiments enables the culture medium to have two interfaces: one in contact with air and the other with the oil phase positioned beneath the culture medium. The interfacially driven films of BNC exhibit compactness and orderliness at both these interfaces. Interestingly, the natural movement of bacteria between these interfaces leads to the formation of interconnected and entangled cellulose nanofibers in the bulk phase, linking the interfacially driven films at the top and bottom interfaces. Consequently, the resulting material forms a biscuit-like hydrogel that can be air-dried to create multilayer constructs. Notably, the middle section of these fabricated structures can be loaded with different nanoparticles, such as magnetic $Fe_3O_{4,}$ to impart specific functionality to the final construct.

The same study also fabricated Janus membranes based on BNC with dual hydrophobic/hydrophilic characteristics on opposite sides.[157] For this purpose, a superhydrophobic electrospun membrane (polyvinylidene fluoride, PVDF) was used to separate the aqueous culture media and oil phase, as shown in Figures 31e-g. The BNC was reported to form a layer on the inner section of the PVDF membrane. Given the hydrophilic characteristics of BNC, the water contact angle for the inner part of this membrane was around 11°, while the contact angle on the outer side of the membrane was 125°. These findings, along with other soft constructs like BNC-based beads and 3D-printed architectures, underscore the pivotal role of interfacially driven assemblies as a potent tool for structural design in the realm of soft functional materials.

In another study, Zhao et al.[75] developed thin films of $Ti_3C_2T_x$ using the concept of nanoparticles` interfacial assembly. Notably, $Ti_3C_2T_x$ with numerous hydrophilic functional groups exhibits a strong affinity for water, resulting in weak assembly at the oil/water interface. To enhance assembly at this interface, this study employed a templating approach to functionalize one side of $Ti_3C_2T_x$ flakes with positively charged polystyrene chains. In this method, MXene nanosheets with negatively charged groups were initially assembled around positively charged polystyrene microspheres. Subsequently, the polystyrene core was removed using toluene, yielding Janus MXene nanoparticles with negatively charged functional groups on one side and positively charged polystyrene chains on the other. These Janus nanoparticles exhibited a strong affinity for the oil/water interface and, after being assembled and compacted using a Langmuir–Blodgett trough, were used to create well-ordered thin films.

Overall, the interfacial assembly of nanoparticles and macromolecules offers an intriguing avenue for developing functional thin membranes and films. For instance, to date, thin films of various materials, including carbon nanostructures,[158, 159] metal nanoparticles,[160] organic crystals,[161] quantum dots,[162] and composite multicomponent assemblies of nanoparticles and polymers,[163-165] have been developed at the liquid-liquid interface. Besides, this fabrication strategy has been employed for surface modification and chemical functionalization of different materials, as evidenced by the studies mentioned above. In this context, the concept of NPS assemblies presents opportunities to expand this field further. For example, developing structures with different characteristics on opposing sides, i.e., Janus constructs, can be particularly promising. Here, the functionality and surface characteristics on one side are defined by the nanoparticles used, while the chemistry of ligands or surfactants employed defines the opposite side.[75]

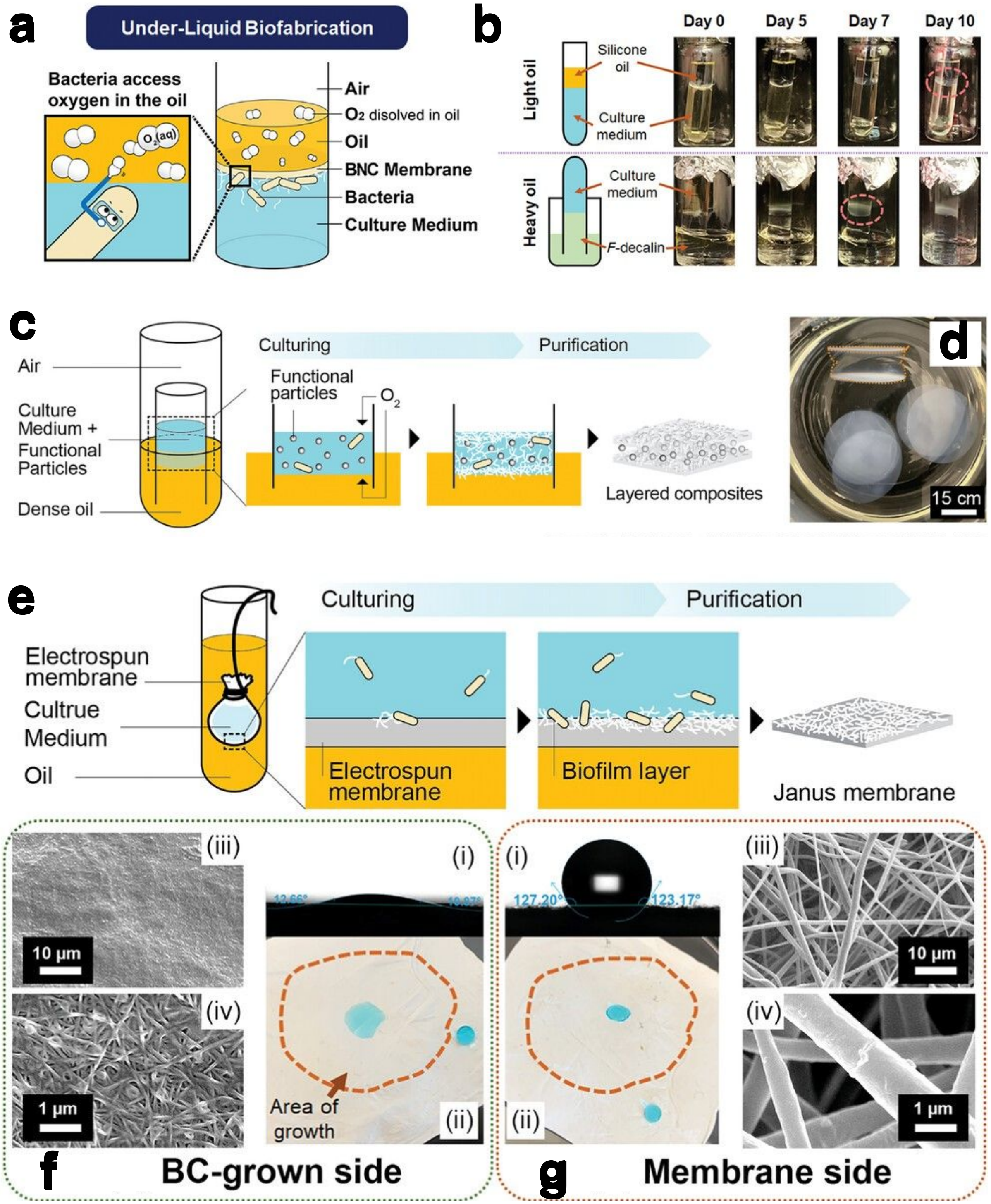

Figure 31: (a-b) Fabrication of BNC thin films at the liquid-liquid interface. The culture media and nutrients are dissolved in the aqueous phase, while the oil phase allows the diffusion of oxygen. (c) Constructing multi-layer biscuit-like composites comprising two compact and

ordered layers at the bottom and top, with a middle section that can be functionalized with active nanomaterials. The cell designed for these experiments enables the culture medium to have two interfaces: one in contact with air and the other with the oil phase positioned beneath the culture medium. (e) Schematic illustration of the setup used to fabricate Janus PVDF/BNC membrane. (f) The BNC side of this membrane is hydrophilic, while (g) the PVDF side is superhydrophobic. (i-ii) Showcase the water contact angle, while (iii-iv) demonstrate the SEM images of the prepared membrane. (a-g) Reproduced with permission.[157] Copyright 2019, Wiley-VCH.

5.3 Liquid-templated soft materials and aerogels

Using structured liquids as a template for developing mechanically stable functional aerogels is a relatively new topic in the field of soft materials. However, we believe this approach holds promise as a groundbreaking fabrication platform with diverse potential applications. Firstly, the interfacially driven skin that stabilizes structured liquids plays a crucial role in maintaining the integrity of the resulting aerogels. Furthermore, this skin imparts specific chemical characteristics to the final constructs. These properties are determined by the type of ligands, nanoparticles, or macromolecules incorporated into the original structured liquids, allowing for tailored functionality in the aerogels. For instance, the aerogels fabricated based on a liquid template that is stabilized by $Ti_3C_2T_X$/POSS NPS showcased exceptional hydrophobic characteristics and water stability.[69] It is worth noting that $Ti_3C_2T_X$ aerogels with numerous hydrophilic functional groups usually degrade in humid environments and cannot be submerged into aqueous media.[166, 167] However, by utilizing interfacial complexation techniques, researchers were able to create a structure with POSS molecules uniformly distributed at the surface of MXene flakes. This arrangement endows the final aerogels with hydrophobic characteristics and exceptional water stability. Consequently, this development allows the aerogel to be submerged in an aqueous environment without concerns about its structural integrity, opening up new possibilities for its use in various water-related applications.[69]

Furthermore, the use of structured liquid templates enables precise control over the porosity and density of the resulting aerogels. For instance, employing the liquid streaming approach, as detailed in earlier sections, we were able to engineer wormlike aerogels with dual micro-to-macro-scale porosities and remarkably low density.[40, 168] Notably, this aerogel fabrication technique is versatile; various worm-like aerogels with GO, magnetic GO/GO, $Ti_3C_2T_X$/GO, and CNF/GO were successfully fabricated using this method, all exhibiting ultra-low density and good mechanical properties.[3, 19, 40, 56] Notably, this method is both robust and cost-effective. The fabrication of liquid templates simply requires a basic pump to inject an aqueous suspension of nanoparticles into a hydrophobic medium containing a ligand. Additionally, the hydrophobic bath with ligands can be recycled multiple times, further demonstrating the cost-effectiveness and sustainability of this approach.

In addition, structured liquids offer a powerful means to integrate the intrinsic properties of nanoparticles into final structures in a customizable way. For example, the creation of worm-like conductive aerogels using $Ti_3C_2T_X$/GO takes advantage of the surfactant-like properties of GO.[19] When coupled with a ligand, GO stabilizes liquid-like threads, while incorporating $Ti_3C_2T_X$ imparts unique electrical conductivity to the structure, making it suitable for a variety of applications. Importantly, these aerogels do not require polymeric additives or crosslinkers, which typically increase the density of the final products significantly.

The platform also extends to Janus worm-like liquid templates and aerogels that feature distinct magnetic, conductive, or non-responsive domains, as detailed in Section 3.2.3. These aerogels showcase anisotropic distributions of nanoparticles at a macro-scale, a feature unattainable through other aerogel fabrication methods.[3] Janus constructs enhance versatility and customizability compared to traditional composites by enabling precise tuning of functionalities on each side. This results in multi-responsive soft materials with well-defined properties and potential applications, including EMI shielding and strain/pressure sensing. The Janus liquid approach is also set for broad application in areas such as dual encapsulation of cells and active matter, compartmentalization of chemical reactions, and multi-functional sensors, where integrating multiple functionalities into a single construct is of utmost importance.

In what follows, we will explore a few pioneering studies focused on the potential applications of liquid-templated aerogels. Our discussion will center on the inherent characteristics, including the chemistry of the interface and the controllable composition and porosities of these aerogels, which have led to breakthroughs in the field of soft functional materials.

5.3.1 Conductive liquid-templated aerogels for EMI shielding

Liquid-templated aerogels made from 2D nanomaterials like MXene and reduced graphene oxide have been used in EMI shielding applications because they combine high electrical conductivity, exceptionally low density, and high porosity in one package.[19, 40] Before delving into the unique performance of these aerogels for EMI shielding, it is important to briefly explain the mechanisms and concept of EMI shielding. Subsequently, we discuss why these aerogels represent a groundbreaking option for designing the next generation of EMI shields.

When an electromagnetic wave encounters a conductive porous structure, a part of the wave is reflected due to the impedance mismatch between the electrically conductive domain and free space. This reflected power is quantified by the reflection index (R), which ranges from 0 to 1. It is important to note that the reflectance index primarily depends on the electrical conductivity of the material, and reducing this index is a key focus in the development of effective EMI shielding. [169, 170]

In addition to reflection, a portion of the incident wave is absorbed by the porous constructs through interactions with electrically conductive materials and active electric/magnetic dipoles. This absorbed portion is measured by the absorption index (A), and the goal is to maximize this factor to create an absorption-dominant EMI shield, ideally achieving an "A" value of at least 0.5. Such high absorption levels are particularly achievable in porous materials due to a mechanism often referred to as "multiple internal reflections" or "internal scattering." This process involves multiple back-and-forth reflections within the shield, facilitated by interfaces with mismatching impedance in the porous material, which significantly enhances its absorption capabilities. Furthermore, a portion of the electromagnetic wave may pass through the structure, resulting in a transmitted wave. This transmission is quantified by the transmission index (T), and minimizing this index is a critical objective to enhance the shielding effectiveness of the structure.[169, 170]

It is important to recognize that current studies on the EMI shielding capabilities of porous materials evaluate performance based on the R, A, and T indexes to identify the primary shielding mechanisms. Additionally, these studies often utilize another parameter known as total shielding effectiveness (SE_T), measured in decibels (dB). The SE_T is crucial as it quantifies the shield's ability to protect against electromagnetic waves and is defined as the logarithmic ratio of the incident power to the transmitted power of the electromagnetic waves. An aerogel EMI shield is considered to exhibit exceptional EMI shielding characteristics if it has a high shielding effectiveness ($SE_T > 30$ or higher) and an absorption-dominant shielding mechanism ($A > 0.5$ or higher). The total density and thickness of the developed shields also play critical roles in evaluating shield performance. Reducing these factors can decrease the total cost of EMI shields and increase their adaptability to various shielding scenarios, enhancing their practicality.

With these parameters in mind, we can see why liquid-templated aerogels are an appealing option for designing the next generation of EMI shielding materials. These aerogels can be engineered to achieve high absorption indices and excellent shielding effectiveness while maintaining low density and customizable thickness, making them versatile and cost-effective solutions for diverse EMI shielding applications.[169, 171, 172]

Shi et al.[69] were among the first researchers to utilize liquid-templated aerogels of MXenes for EMI shielding. In their study, they reported the co-assembly of $Ti_3C_2T_x$ and $POSS-NH_2$ at the toluene/water interface, which stabilized oil-in-water Pickering emulsions. These emulsion templates were then concentrated through simple centrifugation and used as a template to fabricate lightweight, hydrophobic, isotropic MXene aerogels with outstanding mechanical properties (refer to Figure 32a). These aerogels served as a framework for developing conductive epoxy nanocomposites; the MXene aerogels were impregnated with epoxy precursors and allowed to cure. The resulting polymer nanocomposites, with a very low MXene filler content (0.40 vol% of $Ti_3C_2T_x$), exhibited SE_T of 34.5 dB, significantly surpassing conventional polymer nanocomposites of MXene. However, the EMI shielding mechanism of these aerogels primarily relied on reflecting electromagnetic waves due to their relatively high electrical conductivity of 195.3 S/m, leading to a substantial impedance mismatch at the interface of these structures.

More recently, we utilized worm-like aerogels of $Ti_3C_2T_X$/GO, reduced GO, reduced magnetic GO/GO, and carbonized CNF/GO to develop a new class of EMI shields.[3, 19, 40, 56] Our strategy focused on two key factors: 1) Keeping the electrical conductivity of these aerogels relatively low to allow incident electromagnetic waves to enter the structures with minimal reflectance. 2) Leveraging the dual micro-to-macro-scale porosities of worm-like aerogels, unique to these structures, to enhance internal scattering and absorption capabilities. This approach enabled us to achieve high SE_T values (>30 dB) and absorption-dominant characteristics ($A > 0.5$) for some of these samples. For instance, using worm-like templates of $Ti_3C_2T_X$/GO, ultra-lightweight aerogels with a density of 3-7 mg/cm^3 were obtained. When these aerogels served as the backbone for epoxy nanocomposites, unique polymer nanocomposites with extremely low filler content (0.3-0.7 wt%) and exceptional EMI shielding characteristics (SE_T of 31.7–51.4 dB and A ≈52–54% were achieved, indicating dominant absorption behavior) for the samples.[19] This highlights the potential of liquid-templated aerogels for large-scale and cost-effective fabrication of modern EMI shields for military and commercial purposes.

In another study, worm-like aerogels of GO/CNF were used to develop "electromagnetic traps" with enhanced absorption dominant EMI shielding characteristics.[56] In this system, conductive carbonized worm-like aerogels of GO/CNF were placed at the top of highly conductive metal tapes to create EMI shields with remarkably high SE_T values of 53–89 dB and absorbance exceeding 0.7. Several considerations were taken into account when designing electromagnetic traps (refer to Figure 32b). Firstly, the conductivity of the worm-like aerogels was maintained in the range of 10-40 S/m to ensure electromagnetic waves could penetrate the structures with minimal reflectance. Upon entering the shield, the waves' energy was absorbed due to interactions with electric/magnetic dipoles and materials with finite electrical conductivity. The presence of micro-to-macro-scale porosities further enhanced the dissipation of electromagnetic waves through internal scattering mechanisms, as previously explained. Moreover, as the wave path traversed through the aerogel and reached the conductive tape, it reflected back to the aerogel, dissipating and absorbing its remaining energy. This study clearly demonstrated the potential of worm-like aerogels with dual-scale porosities in designing absorption-dominant EMI shields with exceptional performance.

Janus aerogels of $Ti_3C_2T_x$/GO:mGO/GO, with non-interfering magnetic/conductive domains, are also utilized for developing absorption-dominant aerogel traps, exhibiting impressive performance with a SE_T of approximately 51 dB, SE_R of around 0.4 dB, and A = 0.91 (one of the highest reported absorbance values in the field of EMI shielding).[3] The system design and underlying mechanism are akin to what was reported for "electromagnetic traps" in a previous study, where the designed Janus aerogels were positioned atop a highly conductive copper tape. However, the inclusion of non-interfering magnetic/conductive domains in these aerogels further reduces reflectance, as the presence of magnetic stripes adjacent to conductive strips at the interface significantly further reduces the impedance mismatch. Moreover, the interface between magnetic and conductive domains within the aerogels contributes to internal scattering and enhances the absorption capability of these aerogels. These advantages, combined with the absence of thermal and chemical reduction requirements, position these Janus aerogels at the forefront of the EMI shielding field.

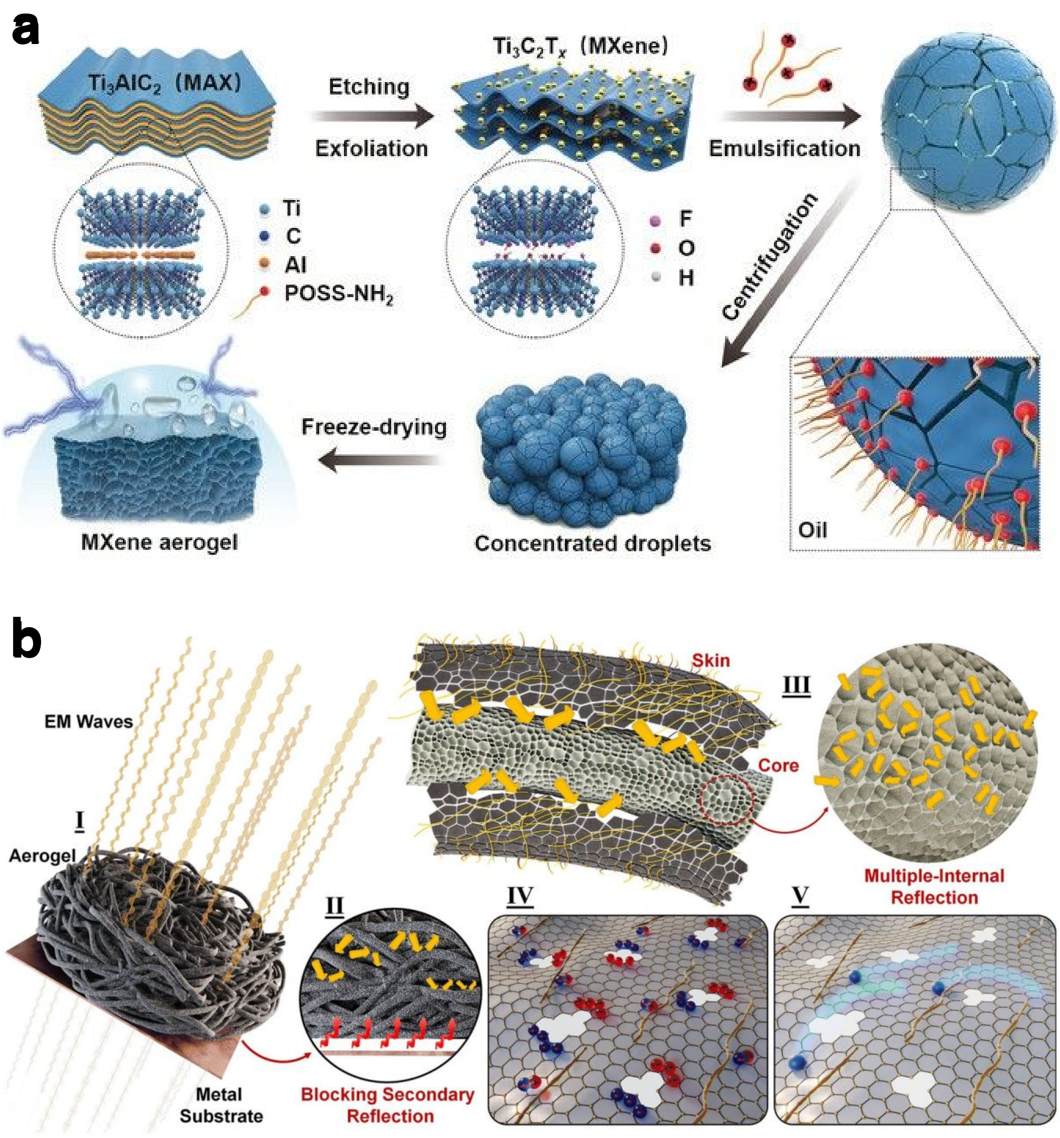

Figure 32: (a) Schematic showing the fabrication of MXene-based structured Pickering emulsions that were used for developing aerogel-based EMI shields through the liquid templating approach. (a) Reproduced with permission.[69] Copyright 2019, Wiley-VCH. (b) Underlying mechanisms that define the concept of "electromagnetic traps." (I) showcases the developed "electromagnetic traps." (II) shows that when electromagnetic waves pass through the worm-like aerogels and reach the conductive tape, they are reflected back toward the aerogels. (III) showcases the concept of internal scattering within and between filaments in worm-like aerogels. (IV) Losses due to interfacial and dipole polarization and (V) conductive losses caused by electron migration and hopping. In IV and V, the yellow rods signify the CNF, while the blue

and red dots indicate positive and negative charges, respectively. (b) Reproduced with permission.[56] Copyright 2024, The Royal Society of Chemistry.

5.3.2 Conductive liquid-templated aerogels for strain/pressure sensing

The potential of liquid-templated aerogels for designing strain/pressure sensors has not been fully realized in the literature. However, the presence of interfacially driven skin in the conductive aerogels fabricated through the liquid-templated strategy is reported to enhance the mechanical characteristics and flexibility of various worm-like aerogels. Therefore, this concept can be utilized to design highly sensitive pressure/strain sensors. In this regard, we used Janus aerogels comprising a non-responsive domain made of GO and a conductive domain made of $Ti_3C_2T_x$/GO to develop pressure sensors.[3] In these aerogels, the non-responsive part enhances mechanical characteristics, while the sensing capability is attributed to the conductive part. When these aerogels are compressed, the density of interconnected conductive sections in the Janus aerogels increases on micro- and macro-scales, resulting in an exponential rise in conductance. This mechanism has been used as the main sensing mechanism in these aerogels for monitoring various human activities, including facial muscle movements, talking, coughing, and even contraction and relaxation of joints and muscles.

It is important to acknowledge that while the developed Janus aerogels have a detection range limited to approximately 60% of compression strain, they may not be the most sensitive option available in the field of strain and pressure sensing. However, these aerogels offer significant advantages, notably their straightforward fabrication process. Unlike other sensors, the Janus aerogels do not require chemical or thermal reduction, nor do they need pre-treatment techniques such as freeze-casting to develop their structures. Additionally, the Janus platform is particularly appealing for creating functional, flexible aerogels. This method allows for customization where one side of the aerogel is tailored for electrical conductivity, while the other side maintains mechanical flexibility. This dual functionality makes Janus aerogels a compelling choice for applications requiring a balance of electrical performance and physical adaptability, enhancing their utility in diverse fields, including wearable technology and smart materials.[3]

5.3.3 Liquid-templated aerogels for oil absorption and water purification

Liquid-templated aerogels offer intriguing prospects for the fabrication of ultra-lightweight oil absorbers with numerous applications in water purification. The ability of these aerogels to absorb various hydrophobic solvents can be elucidated through two key factors: 1) In terms of NPSs-driven aerogels, the co-assembly of ligands and nanoparticles at the interface can tailor the hydrophobicity of the structure, enabling the fabricated aerogels to interact with nonpolar solvents and absorb them within their porous structure.[69] 2) Liquid-templated aerogels, such as worm-like structures, exhibit substantial internal surface area and remarkable porosities, further enhancing their capability to absorb nonpolar solvents.[40]

In this context, a study by Shi et al.[69] is noteworthy, where the interfacial assembly of $Ti_3C_2T_x$ and POSS-NH_2 at the toluene/water interface was utilized for fabricating structured Pickering emulsions, which were then transformed into hydrophobic aerogels with high porosity (Figures 33a-b). In this intriguing study, the hydrophobic characteristics of the aerogels stem from the hydrophobic nature of POSS molecules that uniformly distribute throughout the aerogel matrix without requiring additional surface modification or conventional chemical or thermal treatments typically used in designing carbon-based oil absorbers.

The surface wetting behavior of liquid-templated MXene-based aerogels was investigated by analyzing the water contact angle. While the pure MXene film (evaluated as a reference) displayed hydrophilicity with a contact angle of 42°, attributed to the presence of oxygen and fluorine terminal groups on the MXene surface, the liquid-templated MXene aerogels exhibited a substantial increase in the water contact angle to 123°, indicating the hydrophobic nature of this structure. This change can be attributed to the presence of hydrophobic POSS-NH_2 on the MXene surface. Additionally, these aerogels demonstrated exceptional capability for absorbing organic solvents such as toluene, n-hexane, and silicone oil. For instance, toluene absorption of up to 9000 wt.% was reported for these aerogels (see Figure 33c).

An intriguing example can be found in worm-like aerogels of reduced GO, which present an optimal solution for oil absorption in aqueous media.[40] In this study, worm-like aerogels of GO underwent thermal reduction at 800°C to carbonize the porous structure and render the aerogels hydrophobic. The abundant microscale porosities within the filamentous aerogels, coupled with macroscale porosities between the filaments, contributed to the remarkable oil absorption capacity that surpassed all previous studies on aerogel-based oil absorbers (Figure 33d). For instance, the resulting aerogels demonstrated an absorption capability of approximately 46,000 wt.% for chloroform, 34,000 wt.% for diesel oil, 26,000 wt.% for pump oil, and 20,000 wt.% for motor oil. Furthermore, these worm-like aerogels can release organic solvents after compression (Figure 33e). Moreover, they can effortlessly float on the surface of water, achieving rapid separation of oil from water in less than 5 seconds (Figure 33f). These characteristics render these aerogels particularly attractive for addressing oil spill cleanups.

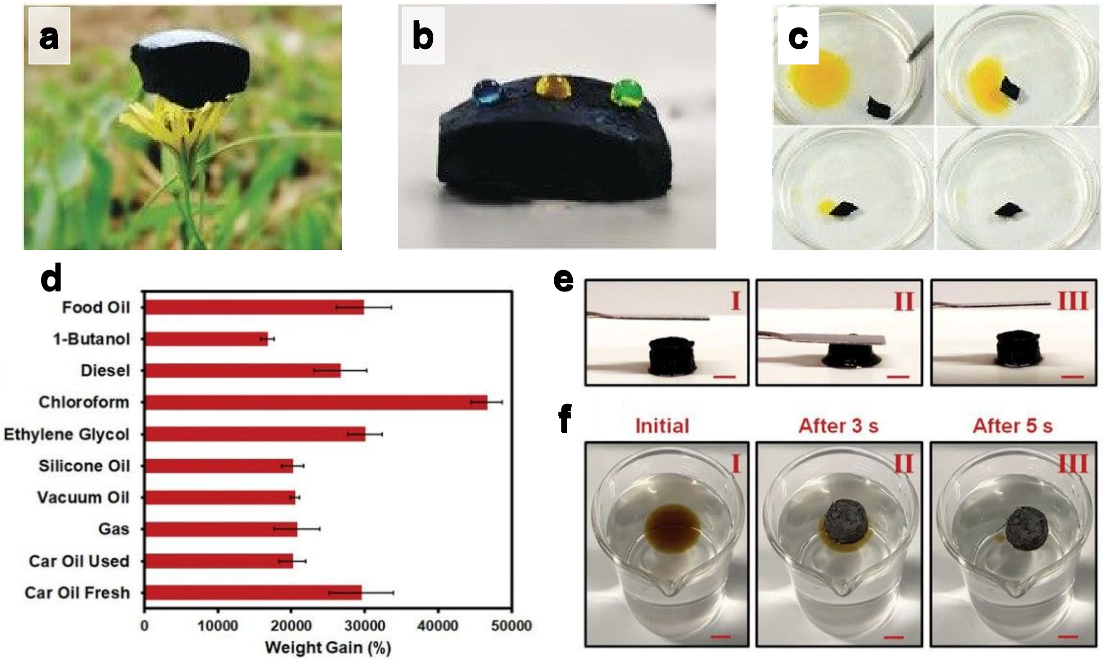

Figure 33: The developed MXene-based aerogel showcased (a) ultra-low density and (b) unique hydrophobic characteristics. (c) Photographs showcasing the oil absorption capability of developed MXene-based aerogels (the yellow phase is a mixture of n-hexene and azobenzene). (a-c) Reproduced with permission.[69] Copyright 2019, Wiley-VCH. (d) The capability of the carbonized worm-like aerogels of GO to absorb various non-polar solvents. (e) Upon compression, the carbonized worm-like aerogels readily release the absorbed oil. (f) The prepared worm-like aerogels can effortlessly float on the water surface and swiftly separate oil from water in around 5 seconds. (d-f) Reproduced with permission.[40] Copyright 2019, Wiley-VCH.

6 Behind characterization of nanoscale assemblies at liquid-fluid interfaces

Having introduced the dynamic and liquid-like assemblies of nanoparticles and even macromolecules at the liquid-liquid interface, along with their background mechanisms and applications, we turn our attention to the various characterization methods available to analyze this class of assemblies. In general, exploring the dynamic and static behavior of nanoscale assemblies at the liquid-fluid interface remains a largely unexplored frontier in existing reviews of structured liquids and emulsions. This comprehensive characterization involves the direct observation of nanoparticles and macromolecular assemblies at the interface, utilizing advanced techniques like in-situ or ex-situ electron microscopy and X-ray scattering/diffraction methods. Beyond this, the influence of nanoscale assemblies on the liquid-fluid interface, including effects like reduced interfacial tension or elastic deformation, provides a rich avenue for evaluating these systems. In the following sections, we delve into these critical aspects, highlighting the latest and most intriguing progress made in characterizing nanoscale assemblies at liquid-fluid interfaces.

6.1 Direct observation of nanoparticles and supramolecular assemblies at the liquid-fluid interface

Examining the dynamic and static behavior of nanoparticle/supramolecular assemblies at the liquid-fluid interface is crucial for understanding their packing and interactions, linking macroscale features of structured liquids to the nanoscale arrangement at the interface. In this regard, numerous studies have focused on employing diverse electron microscopy techniques, such as TEM, SEM, and AFM, as well as X-ray scattering/diffraction methods, to directly assess various assemblies at the liquid-liquid interface.[14, 173, 174] Generally, electron microscopy techniques offer exceptional resolution for analyzing the arrangement and packing order of assemblies, with state-of-the-art TEMs achieving the highest resolution, capable of highlighting even light atoms like hydrogen and carbons within the assemblies.[173, 175] Conversely, X-ray scattering and diffraction techniques are adept at probing periodic structures across multiple length scales, offering valuable insights into the packing order of nanomaterials and other species at the liquid-liquid interface. These techniques, such as small-angle X-ray scattering (SAXS) and wide-angle X-ray scattering (WAXS), have a significantly larger probing window compared to electron microscopy approaches. They can easily examine millions of particles at the interface, with the scope of investigation dependent on factors like particle concentration, beam size, and integration time. In contrast, electron microscopy techniques, such as TEM, typically cover far fewer particles but provide exceptionally higher resolution. This allows for detailed visualization of individual particles and their interactions at the interface, complementing the broader scope of X-ray techniques by providing microscopic detail.[173, 176-178] Therefore, these methods are complementary, and it is highly recommended to utilize both for the comprehensive characterization of interfacial assemblies whenever feasible.

The challenges associated with conducting in-situ characterization have prompted numerous research groups to opt for ex-situ evaluations of interfacial assemblies using diverse sampling techniques, including gel trapping of interfacial assemblies, freeze-fracture shadow-casting, and Langmuir–Blodgett compression.[26, 179-181] Despite facing obstacles such as alterations in packing order and structures due to capillary forces during drying or changes in the vertical position of nanoparticles post-sampling, ex-situ assessment of interfacial assemblies has proven valuable in providing information on wetting characteristics and contact angles of nanoparticles at the liquid-liquid interface.[14] For example, Reincke et al.[26] used the Langmuir–Blodgett technique to transfer a monolayer film of charged Au nanoparticles formed at the heptane/water interface onto a glass substrate before conducting TEM analysis for contact angle measurements. In another study, Mihali and Honciuc created Langmuir–Blodgett films of amphiphilic polystyrene (PS) nanoparticles at the air/water interface and assessed the nanoscale arrangement of the fabricated films using SEM.[179] However, the presence of strong capillary forces during both sampling and drying of the prepared Langmuir–Blodgett films significantly alters the configuration and structure of the interfacial assemblies, limiting the potential of this sampling technique as a quantitative method, especially when dealing with low aerial density of nanoparticles at liquid-fluid interfaces.

In another intriguing ex-situ exploration of nanoparticle behavior at a liquid-fluid interface, a gel trapping approach was employed, wherein nanoparticles dispersed at an air/water or oil/water interface were captured through the gelation of the aqueous phase using a non-surface-active polysaccharide.[180, 182] The gel surface was subsequently replicated using a PDMS elastomer and characterized via SEM and AFM approaches, providing valuable insights into the contact angle and vertical positioning of nanoparticles at liquid-fluid interfaces (Figure 34a). In another study, Isa et al.[181] introduced the freeze-fracture shadow-casting approach to capture the interfacial behavior of nanoparticles at a liquid-liquid interface (Figure 34b). In this method, an oil/water interface containing nanoparticles is rapidly frozen using a jet freezer and then fractured to expose immobilized nanoparticles. Here, the interface was considered a weak point that promotes fracture propagation, preferentially exposing the oil/water interface upon applying shear force. The prepared samples were then unidirectionally coated with metal and assessed with cryo-SEM to glean valuable information about the wetting characteristics of nanoparticles and their contact angles at the oil/water interface (Figures 34b-c). Notably, the accuracy of this method was cross-examined with the gel-trapping approach. However, as reported by Forth et al.[14], the solidification of the liquid raises concerns due to its potential to change the vertical position of the nanoparticles at the original interface.

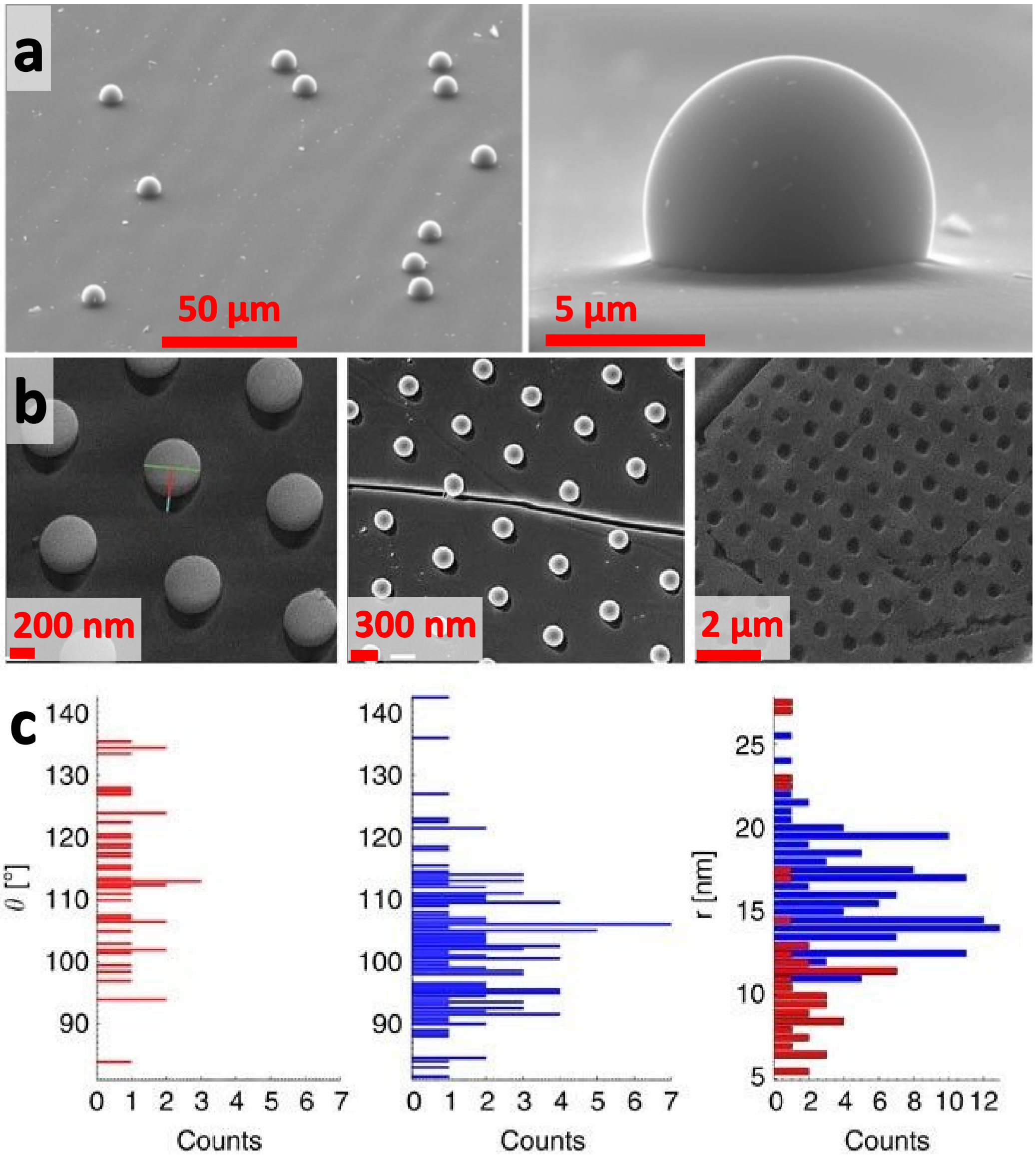

Figure 34: Ex-situ examination of nanoparticles behavior at a liquid-fluid interface. SEM views of different nanoparticles at the liquid-fluid interface were captured through (a) gel trapping approach and (b) freeze-fracture shadow-casting. These images provide information regarding the contact angle and wetting properties of nanoparticles. (a) Reproduced with permission.[180] Copyright 2003, American Chemical Society. (c) Distributions of measured contact angles and size distribution of nanoparticles captured through freeze-fracture shadow-casting. These results were based on 20 nm latex nanoparticles at the n-decane/water (red) and n-hexane/water (blue) interface. (b-c) Reproduced with permission.[181] Copyright 2011, Nature Publishing Group.

On the other hand, the in-situ examination of nanoparticle/macromolecule assemblies at a liquid-fluid interface holds greater value as it correlates the collective behavior of nano-scale assemblies with the macro-scale properties of the interface. Simultaneously, it offers a realistic measurement of the wetting characteristics of nanoparticles, including the contact angle at the liquid-fluid interface.[144, 183, 184] To this end, in-situ AFM has been used to capture the three-dimensional arrangement of responsive nanoparticles at a liquid-liquid interface. This approach was introduced by Costa et al.[185, 186], where a thin layer of nanoparticles aqueous suspension, i.e., typically less than 100 μm, was placed on a piece of mica and then covered by an organic solvent before in-situ AFM analysis. Subsequently, Russell and colleagues introduced an alternative sample geometry where the oil phase is positioned beneath the water phase, exemplified by an aqueous suspension of silica nanoparticles functionalized with carboxylic acid at the top and PDMS-NH_2/silicon oil at the bottom (Figure 35a).[49] This inventive arrangement yields multiple advantages, primarily mitigating evaporation of the organic/oil phase by its shielding with the water phase, thus offering increased flexibility in selecting the oil phase—encompassing choices such as organic solvents and silicone oil. Furthermore, the configuration facilitates the dispersion of surfactants and nanoparticles in distinct phases, ensuring that interactions between different species occur exclusively at the interface. Consequently, this modification significantly broadens the applications of in-situ AFM in the study of nanoscale assemblies at a liquid-liquid interface.

One of the most captivating studies on in-situ AFM evaluation of interfacial assemblies was conducted by Chai et al.[187] In this study, they investigated the dynamic assembly and jamming of NPSs at the oil/water interface, employing an aqueous suspension of carboxylated silica nanoparticles and PDMS-NH_2/silicon oil as the two immiscible phases. The researchers concluded that the rate at which nanoparticles attach to the oil/water interface is primarily determined by the available free space at the interface that incoming nanoparticles can occupy. During the initial unoccupied stage, attachment relies solely on the diffusion of nanoparticles to the interface, a process directly linked to the solid concentration of the aqueous phase. Notably, in-situ AFM also shows that nanoparticles can adhere to a densely packed interface through a displacement mechanism, wherein they displace previously attached nanoparticles present at the oil/water interface (Figures 35b-d).

This displacement process functions within a reaction-controlled attachment paradigm, where the existing assembly serves as an electrostatic barrier, governing the approach of nanoparticles to the interface.[187] The coordinated rearrangement and displacement mechanism are highlighted in Figure 35c, unfolding over a five-minute duration. This dynamic process is concisely summarized in Figure 35d, spotlighting the nanoparticle newly attached to the interface with a faded blue circle, while those exiting the viewing panel are denoted by faded red circles. These findings underscore the capability of in-situ AFM in characterizing the intricate behavior of nanoparticle assembly and interfacial jamming at liquid-liquid interfaces, suggesting the future adoption of this method for the analysis of various 1D and 2D nanoparticles at such interfaces. Additionally, there is potential to broaden the scope to include composite interfacial assemblies comprising different types of nanoparticles, thereby enriching our understanding of interfacial interactions.

Real-space imaging of nanoparticle behavior at the liquid-fluid interface can be visualized on a nanometer scale using liquid TEM and SEM techniques. [188-190] For instance, Kim et al.[188] examined the dynamic behavior of nanoparticles at the liquid-fluid interface by capitalizing on the nonvolatile nature of an ionic liquid, specifically 1-ethyl-3-methylimidazolium ethyl sulfate ([emim]-[EtSO4]). While SEM analysis typically requires a high vacuum, making the analysis of liquid samples complex, the ionic liquid exhibits vanishingly low volatility at ambient temperature, ensuring stability under high vacuum conditions. Consequently, nanoparticles can be dispersed in this hydrophilic ionic liquid with minimal impact on their motion, allowing for the in-situ evaluation of single-particle behavior at the air-liquid interface. This approach eliminates the need for a costly liquid sample holder for SEM analysis (see Figure 35e).

The same ionic liquid was also employed by Fink et al.[189] to assess the dynamic interfacial behavior of nearly monodispersed spherical nanoparticles at a nonvolatile ionic liquid-air interface. However, in this study, a custom-built liquid sample holder was utilized to regulate the areal fraction of nanoparticles at the liquid-fluid interface by employing sequential addition and withdrawal of liquid to adjust drop size during SEM analysis. The intriguing perspective provided by this research is illustrated in Figure 35f, where a jammed state of nanoparticles at the liquid-fluid interface can be unjammed by expanding the extruded droplet. Conversely, the system returns to a jammed state by removing liquid from the droplets and reducing the contact area of the droplet at the liquid-fluid interface. Beyond presenting visually compelling evidence of jamming phenomena, this investigation yields quantitative insights into the diffusion process of nanoparticles at the liquid-fluid interface—an aspect relatively novel in the realm of interfacial assembly.

On the flip side, liquid TEM offers enhanced resolution for observing the spatial arrangement of nanoparticles over time, albeit with a relatively narrower detection window compared to in-situ SEM. Lin et al.[190] demonstrated this capability by utilizing in-situ liquid TEM to capture the dynamic assembly of platinum nanoparticles forming flexible ring-like chains around ethylenediaminetetraacetic acid nanodroplets dispersed in a solution (Figures 35g-h). As illustrated in Figure 35h, this method is capable of analyzing the attachment, assembly, and rearrangement of nanoparticles at the liquid-liquid interface on a nanoscale. Additionally, this study highlighted interactions between different nanoparticle assemblies, revealing the formation of large ring-like nanoassemblies through collisions and merging of smaller rings. However, challenges such as the delicate handling of liquid-TEM cells, potential damage from the high-energy beams of the TEM setup to organic solvents, and the inevitable interaction of nanostructures with the walls of liquid-TEM cells still remain unanswered for liquid TEM, significantly impacting its performance in characterizing interfacial assemblies.

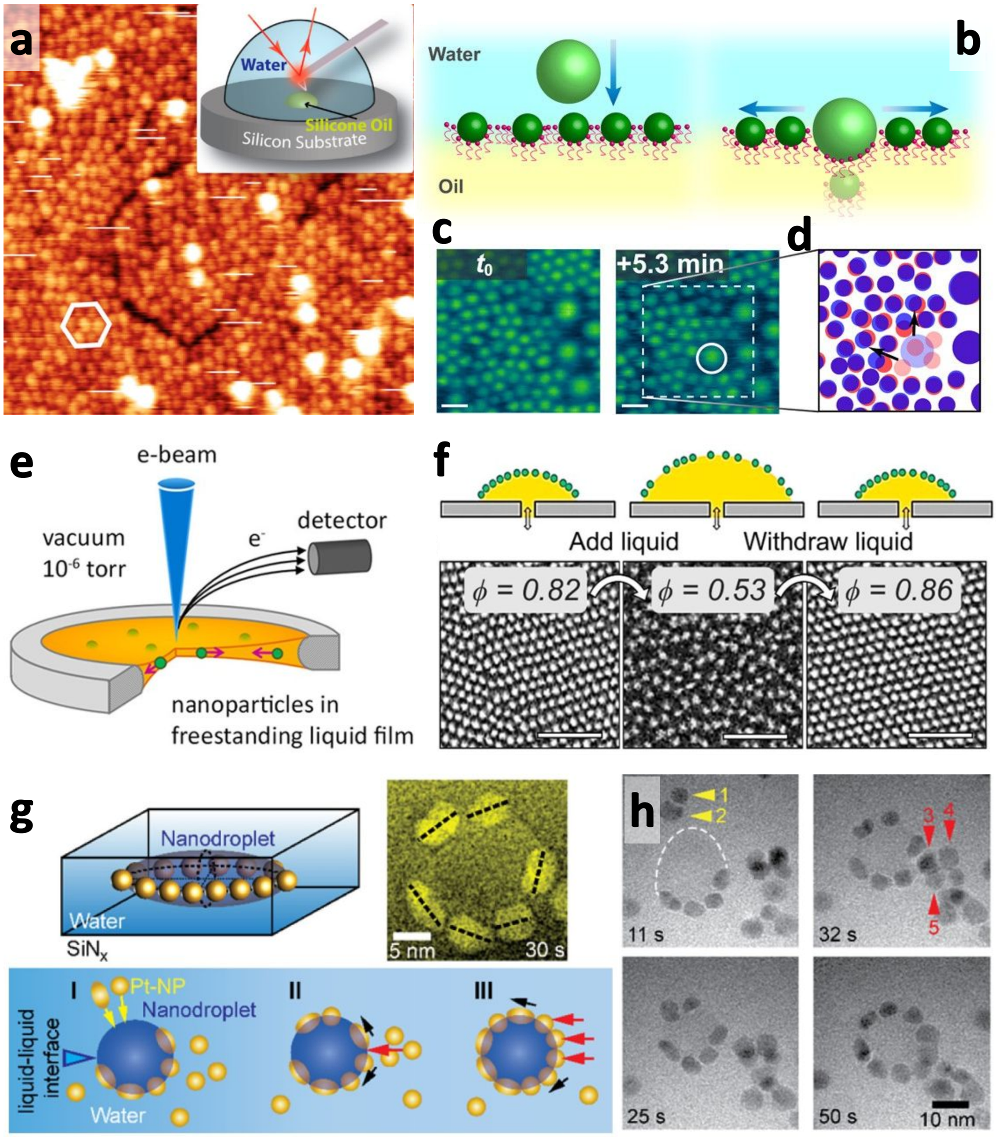

Figure 35: In-situ characterization of nanoparticles` behavior at a liquid-fluid interface using advanced electron microscopy techniques. (a) In-situ AFM image of NPSs assemblies at the silicone oil/water interface, i.e., the aqueous suspension of silica nanoparticles functionalized with carboxylic acid at the top and PDMS-NH_2/silicon oil at the bottom. (a) Reproduced with permission.[49] Copyright 2017, American Chemical Society. (b-d) In-situ AFM evaluation of dynamic assembly and jamming of NPSs at the oil/water interface. Here, an aqueous suspension of carboxylated silica nanoparticles and PDMS-NH_2/silicon oil were used as the two immiscible phases. (c) Time-dependent in-situ AFM images of NPSs assemblies at oil/water interface. (d) NPSs positions at the beginning of the test (t_0, red) and 5.3 min later (t_0 + 5.3 min, blue). (b-d) Reproduced with permission.[187] Copyright 2020, American Association for the Advancement of Science. (e) SEM images of polymer-grafted silica nanoparticles at the air–ionic liquid interface. (e) Reproduced with permission.[188] Copyright 2016, American Chemical Society. (f) Assessing the dynamic interfacial behavior of monodispersed spherical nanoparticles at a nonvolatile ionic liquid-air interface using a custom-made liquid SEM cell. SEM images showed the jammed/unjammed states of nanoparticles at the air-liquid interface upon applying sequential addition/withdrawal of liquid. (f) Reproduced with permission.[189] Copyright 2023, American Chemical Society. (g) Liquid cell TEM analysis of platinum nanoparticles attached to ethylenediaminetetraacetic acid/water interface. (h) This approach can capture the attachment, assembly, and rearrangement of nanoparticles at the liquid-liquid interface. (g-h) Reproduced with permission.[190] Copyright 2016, American Chemical Society.

While real-space imaging provides valuable information regarding the complex dynamic behavior of nanoscale assemblies at the interface, scattering-based methods prove to be a straightforward approach to evaluating the packing order of nanoparticles at the liquid-liquid interface, where the structural information of the assemblies is averaged over the footprint of the X-ray beam.[14, 173, 186, 191, 192] Grazing-incidence small-angle X-ray scattering (GISAXS) has been used to this end to characterize the in-plane packing order of nanoscale assemblies at the interface. Compared to SAXS, where nanoparticle assemblies are probed by an incident beam perpendicular to the sample surface, GISAXS uses X-ray beams that hit the sample surface at a small angle. By employing this approach, it becomes possible to adjust the penetration depth of X-rays within a range spanning from less than 1 nanometer to several hundred nanometers. This, in turn, allows for the customization of surface sensitivity according to specific requirements.[173]

In an interesting study by Huerre et al. [193], GISAXS was integrated with pendant drop tensiometry to dynamically explore the arrangement of ligand-grafted nanoparticles at the liquid-liquid interface (Figure 36a). Through this methodology, GISAXS provided insights into the interparticle distance and packing order, while the tensiometry technique assessed the surface pressure of the pendant drop. Consequently, this method establishes a correlation between interfacial stress and the microstructures of the monolayer at the liquid-liquid interface. Interestingly, their results revealed that the distance between nanoparticles at the liquid-liquid interface reached a constant value after around 2000 seconds, while the surface tension continued to decrease over a longer timescale, i.e., ~4000 seconds. This behavior may be attributed to the formation of particle rafts at the interface, where an increase in the number of particles leads to growing rafts, while the packing distance in the in-plane direction remains constant. Their study also delved into the surface pressure and packing order of nanoparticles at the liquid-liquid interface during the compression of formed monolayers. Remarkably, the changes in interparticle distances depended on the compression rate of the interface, with relatively low compression rates allowing further reduction of interparticle distances, as nanoparticles and ligands had sufficient time to rearrange.

X-ray photon correlation spectroscopy (XPCS) has also been employed to assess the dynamic assembly of nanoparticles at the liquid-liquid interface. For instance, Cui et al.[191] utilized this technique to examine the transition of nanoparticle assemblies from a liquid-like to a jammed state at the interface of water-in-toluene emulsions. In another study, Kim et al.[194] applied grazing incidence small angle XPCS (GIS-XPCS), a combination of GISAXS and XPCS, to analyze the interfacial assembly and jamming of NPSs (surface-grafted Au nanoparticles with carboxylic acid terminated by heptaethylene glycol ligands/POSS) at the silicon oil/water interface (Figure 36b). Their findings illustrated the dynamics of NPS jamming, where initially, nanoparticles were segregated to locally clustered interfaces. During this stage, the nanoparticles` relaxation within localized clusters was almost five orders of magnitude slower compared to the relaxation rate of free particles within the bulk material. This slow attachment to the interface persisted into the subsequent stage until the interface was nearly saturated, leading to local jamming, and the dynamics slowed even further until the system reached collective jamming through cooperative rearrangement.

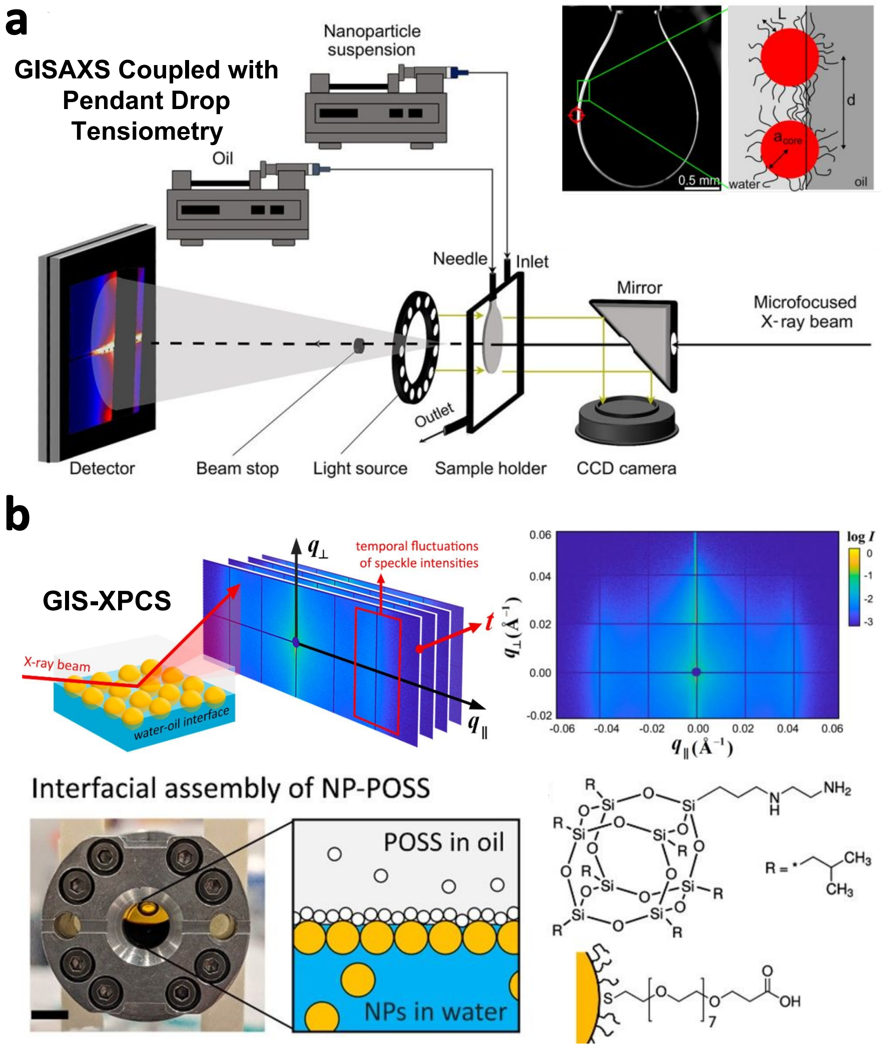

Figure 36: In-situ characterization of nanoparticles` behavior at a liquid-fluid interface using scattering-based techniques. (a) Integrating GISAXS with pendant drop tensiometry to dynamically examine the arrangement of nanoparticles at the liquid-liquid interface. (a) Reproduced with permission.[193] Copyright 2017, American Chemical Society. (b) GIS-XPCS for analyzing the interfacial assembly and jamming of NPSs, i.e., surface-grafted Au nanoparticles with carboxylic acid terminated by heptaethylene glycol ligands/POSS, at the silicon oil/water interface. (b) Reproduced with permission.[194] Copyright 2022, American Chemical Society.

6.2 Macroscopic evaluation of nanoscale assemblies at liquid-fluid interfaces

6.2.1 Interfacial tension measurements

Interfacial tension is the predominant analytical approach for investigating supramolecular and nanoparticle assemblies at the liquid-fluid interface. It represents a phenomenon wherein there exists an energy difference between molecules at a fluid interface compared to the bulk. In simpler terms, interfacial tension is elucidated by the energy required to form a unit area of interface between two immiscible fluids, measured typically in units such as Joule per square meter or, more commonly, Newton per meter.[14, 195, 196] In this regard, pendent drop tensiometry emerges as the foremost method for assessing the influence of nanoparticle and supramolecular assemblies on interfacial tension. This technique is particularly attractive due to its affordability, ease of use—especially in the context of liquid-liquid interfaces—and cost-effectiveness, requiring only small volumes (as low as 50 µl for each test) of challenging-to-synthesize nanomaterials or supramolecules.[14]

Within pendent drop tensiometry, the configuration of the liquid-liquid interface is dictated by gravitational and surface forces, as well as the boundaries that confine the droplet. Taking these factors into account, a pendent drop at equilibrium adheres to the Young-Laplace equation, establishing a connection between the Laplace pressure across the interface, the curvature of the interface, and the interfacial tension, as shown in the following equation.[14, 195]

$$\gamma\left(\frac{1}{R_1}-\frac{1}{R_2}\right) = \Delta P = \Delta P_0 - \Delta\rho g z$$

(1)

Where γ is the interfacial tension, R_1 and R_2 denote the principal radii of curvature at a distance of z from the droplet's apex, $\Delta\rho$ is the density difference between the fluids involved, and ΔP is the pressure difference between internal and external fluids, which is also known as Laplace pressure. ΔP can be re-written as a reference pressure ΔP_0 at $z = 0$ and a hydrostatic pressure of $\Delta \rho g z$. Leveraging the asymmetry inherent in a pendent drop, Equation (1) can be transformed into cylindrical coordinates and subsequently numerically solved. This solution yields the interfacial tension between two liquids based on the measured shape of the liquid-liquid interface.[195]

The adsorption of nanoscale assemblies, including nanoparticles and supramolecular clusters at the liquid-liquid interface, is known to reduce the measured interfacial tension between two immiscible liquids dramatically.[14, 24, 62] The primary contribution to this reduction comes from those nanoscale assemblies positioning themselves between the two immiscible liquids and screening them in a way that the required energy to form the interfaces reduces significantly. However, this phenomenon cannot be straightforwardly represented through the Young-Laplace equation, as this equation assumes the existence of a single isotropic surface tension, which is not valid for the case of nano-to-macro scale particle assemblies.[197, 198] In general, equation (1) loses its accuracy when dealing with solid interfaces or other surfaces with anisotropic stress. This is because we need to consider not just surface energy but also the mechanical characteristics of the material arranged at the interface. Hence, for pendent drop tensiometry, it becomes crucial to integrate a pressure sensor on the droplet side. This allows us to account for the intricate properties of interfaces that involve nanoscale assemblies.[14]

6.2.1.1 Determining the binding energy of nanoparticles at the liquid-liquid interface through interfacial tension measurements

Theoretically, in the absence of particle-particle interactions, the decrease in interfacial energy between two immiscible liquids upon introducing particles into one of the liquids is correlated with the binding energy per area $(\frac{\Delta E}{\delta A})$ for each particle at the liquid-liquid interface, as depicted in the following equation.[14, 199]

$$\gamma = \gamma_0 + N_s(\frac{\Delta E}{\delta A})$$

(2)

Here, ΔE represents the energy required for a single particle to bind to the interface, γ_0 and γ denote the interfacial tension between two immiscible liquids before and after the introduction of particles into one of the liquids (with $\gamma - \gamma_0$ representing the reduction in interfacial tension), and N_s stands for the number of particles adsorbed onto the interface.

In the context of spherical nanoparticles, Dinsmore and colleagues rearranged equation (2) to compute ΔE as follows:[199]

$$\Delta E = \frac{-(\gamma_0 - \gamma)\delta A}{N_s} = \frac{-(\gamma_0 - \gamma)\pi R^2}{\eta}$$

(3)

Where $\eta = \frac{N_s \pi R^2}{\delta A}$ is the area fraction of particles at the interface and R is the radius of the nanoparticles. To calculate ΔE accurately, measurements of γ_0 and γ at a known value of η are essential, and pendent drop tensiometry is employed for this purpose. The referenced study presumed that nanoparticles are densely packed at the interface with η = 0.91. In practice, the value of η can also be determined using in-situ techniques such as SAXS or GISAXS. These methods allow for a relatively precise determination of the average center-to-center distance between neighboring nanoparticles.[14]

The energy needed to detach a spherical particle from the interface to the adjacent bulk fluid, i.e., the binding energy, can also be expressed as a function of the particle's wetting characteristics. This perspective assumes a simplified scenario where no energy barriers are hindering the particles from reaching the fluid-fluid interface.[14, 200]

$$\Delta E = -\gamma_0 \pi R^2 (1 - |\cos\theta|)^2$$

(4)

Here, the angle θ, the angle θ, representing the contact angle at the interface, is measured relative to the aqueous phase.

Capitalizing on this equation, Zhang et al.[198] combined SEM analysis and pendant drop tensiometry to establish an estimated correlation between the area fraction of particles at the interface η and the measured fluid-liquid surface tension, as shown in the following equation.

$$\gamma = \gamma_0 \left[1 - \eta (1 - |\cos\theta|)^2\right]$$

(5)

Arguably, the most crucial finding in the aforementioned study is that equation (5) remains valid even at near-complete packing levels at the interface. This suggests that the particle-particle interaction has an insignificant impact on the reduction of interfacial tension, assuming the particles are highly attracted to the interface due to their wetting properties and face no barriers preventing their adsorption onto the interface.[198]

The binding energy of an individual particle to the interface can also be determined through dynamic surface tension measurements at a short timescale—specifically, by utilizing the initial 10 seconds of the recorded surface tension data, as expressed in the following equation:[201]

$$\gamma = \gamma_0 - 2N_A|\Delta E|C_0\sqrt{\frac{Dt}{\pi}}$$

(6)

In this context, γ represents the interfacial tension at time t, N_A is the Avogadro constant, C_0 is the initial bulk concentration of particles, and D is the diffusion coefficient dictating the adsorption rate at the oil/water interface. Notably, in this scenario, D is equivalent to the diffusion coefficient derived from the Stokes-Einstein relation.

Beyond assessing binding energy, dynamic surface tension measurements offer a means to evaluate the adsorption barrier of particles in comparison to a scenario with an unrestricted bare interface ($t \rightarrow 0$). This is achieved by analyzing the long timescale data ($t \rightarrow \infty$) from interfacial tension measurements. This highlights the effectiveness of dynamic surface tension measurement as a powerful tool for concurrently evaluating two essential parameters: the binding energy and adsorption barrier of particles.[14, 201]

The equations mentioned above solely consider the wetting properties of nanoparticles at the liquid-liquid interface, overlooking particle-particle interaction at the interface. Hence, a more comprehensive theoretical framework has been proposed to assess both these parameters in reducing interfacial tension (Figures 37a-b), as outlined in the following equation:[202, 203]

$$\gamma = \gamma_0 - \pi_{SA}(t) - \pi_{NP}(t)$$

(7)

Where γ denotes the interfacial tension at time t, $\pi_{SA}(t)$ stands for the surface pressure arising from particle-particle interaction, and $\pi_{NP}(t)$ represents the surface pressure resulting from the wetting of particles at the interface. These parameters are computed using the following equations, providing a realistic interpretation of interfacial tension reduction caused by the particles' interactions at the liquid-liquid interface.[202]

$$\pi_{NP} = |\Delta E| \times \Gamma$$

(8)

$$\pi_{SA} = -KT\Gamma_{c\to\infty}\left[\ln(1-\vartheta) - 0.5k\vartheta^2\right]$$

(9)

Where Γ represents the surface excess of nanoparticles at the interface, given by $\Gamma = \frac{\eta}{\pi R^2}$, $\vartheta = \frac{\Gamma}{\Gamma_{c\to\infty}}$ signifies the fractional coverage of the surface-active materials at the interface, and $\Gamma_{c\to\infty}$ denotes the maximum coverage at the interface. Additionally, the parameter K characterizes the interaction potential between particles in units of kT, typically on the order of ±1 for systems involving nanoparticles. A positive value for K indicates repulsive interactions, leading to an intuitive rise in surface pressure, whereas negative K implies attractive interactions and a reduction in surface pressure. The special case of $K = 0$ corresponds to noninteracting particles.[14, 202, 203]

6.2.2 Expansion/contraction of a pendant drop

As discussed before, pendant drop tensiometry is primarily employed for assessing surface tension, a parameter crucial for understanding molecular and nanoparticle assemblies at the liquid-fluid interface. Nevertheless, the same experimental arrangement can be repurposed to visualize the irreversible and solid-like adsorption of nanoparticles at a liquid-liquid interface through the expansion and contraction of a pendant drop. In this experimental setup, a droplet containing a surface-active material, such as nanoparticles or supramolecules, is suspended in another immiscible liquid. As the droplet undergoes contraction, its volume reduces, leading to a corresponding decrease in the interfacial area and the application of compressive forces to the interface.[14, 19] The imposition of such compressive forces on an interface containing adsorbed species can result in various phenomena. These may include the desorption of active materials,[204] the formation of surface wrinkles at the liquid-liquid interface that subsequently undergo relaxation and disappearance,[205] and ultimately, the creation of permanent wrinkles that signify the irreversible bonding of active materials at the interface (Figures 37c-e).[3, 14, 19] This multifaceted approach broadens the scope of pendant drop tensiometry, enabling the investigation of both reversible and irreversible assemblies within liquid-liquid interfaces.

The interaction of nanoscale assemblies at a liquid-liquid interface under the influence of compressive forces is intricately linked to the equilibrium between the compression rate, referred to as the strain rate $\dot{\epsilon} = \frac{dA/A}{dt}$, and the characteristic timescale of particle desorption represented by τ_{des}. If $\dot{\epsilon} \gg \tau_{des}{}^{-1}$, no wrinkles appear at the interface during contraction, and the shape of the pendant drop conforms to the Young-Laplace equation (Figure 37c).[204] In this scenario, the adsorption of surface-active species into the interface is reversible, and compression leads to the desorption of species, ultimately causing the relaxation of surface tension to an equilibrium value independent of area. On the other hand, when dealing with large nanoparticles having a radius of 5-10 nm, and in some cases with polymers or proteins, we may encounter a scenario where $\dot{\epsilon} \sim$

${\tau_{des}}^{-1}$. This is characterized by the formation of wrinkles at the interface, which, over time, undergo disappearance due to relaxation (Figure 37d).[205]

Ultimately, when surface-active species irreversibly bond to the interface ($\dot{\epsilon} << {\tau_{des}}^{-1}$), interfacial wrinkles persist indefinitely (Figure 37e).[14] In this context, the particles typically maintain a monolayer when compressed. However, if compressed to the point of solidification, they do not form a multilayer. Instead, the particle assembly buckles out of the plane, creating permanent wrinkles, which reveal a strong interfacial membrane at the liquid-liquid boundary. Recently, we applied such a scenario to elucidate the irreversible bonding of various nanomaterials, including pure or hybrid forms of GO, magnetic GO, MXene, and CNF, at a liquid-liquid interface.[3, 19, 40, 206] This involved the formation of NPSs through the interaction of these nanomaterials at the interface with an interfacially active ligand, i.e., POSS, effectively pinning the nanomaterials to the interface. Upon contraction of the pendant drop in the aforementioned systems, observable wrinkles emerged at the liquid-liquid interface. These wrinkles persisted over time for both large and small droplets, demonstrating the irreversible adsorption of nanoparticles onto the interface that improves the mechanical robustness of the interface.

6.2.3 Interfacial rheology

Interfacial rheology delves into the response of the liquid-fluid interface to deformation and flow. Within this context, the arrangement of nanoparticles and supramolecules at the interface introduces an additional contribution to surface stress that necessitates thorough examination. In essence, when we deform an interface, two concurrent events transpire. Firstly, the extent of the liquid-fluid interface is altered, and secondly, the materials assembled at the interface undergo deformation. Both of these processes result in energy dissipation, directly influencing the interfacial rheology and mechanical properties of the interface. The impact of these energy costs on the surface stress of a rheologically complex interface can be expressed using the following equation.[207, 208]

$$\sigma_s = \sigma(\alpha,T)I_s + \tau$$

(10)

In the given equation, $\sigma(\alpha,T)$ represents the interfacial/surface tension dependent on excess concentration (α) and temperature (T), I_s denotes the surface unit tensor, and τ signifies the additional surface stress. The incorporation of extra surface stress into equation 10 serves to account for energy costs that are not considered in the homogeneous bulk phase. This model, commonly referred to as the sharp interface model, proves most applicable to liquid-fluid interfaces characterized by a small and well-defined interface formed between two immiscible fluids. However, its applicability diminishes when dealing with slightly miscible fluids and unstructured interfaces lacking precise and sharp boundaries between the two fluids, as exemplified by water and slightly immiscible alcohols such as 1-butanol.[207]

The additional surface stress in equation 10 can be explained using the Boussinesq-Scriven model, particularly when dealing with a liquid-like and viscous interface, denoted as τ_v.[207, 209-211]

$$\tau_v = [(\kappa_s - \eta_s)\nabla_s . v]I_s + 2\eta_s D_S$$

(11)

Where κ_s signifies the interfacial/surface dilatational viscosity, η_s is the interfacial/surface shear viscosity, ∇_s corresponds to the surface gradient operator represented as $I_s . \nabla$ (where ∇ stands for the gradient operator), v depicts the velocity vector at the interface, and D_S is the surface rate-of-deformation tensor expressed as $D_S = (\nabla_s v.I_s + I_s.(\nabla_s v)^T)/2$.

The additional surface stress can also be calculated for solid-like elastic interfaces, i.e., denoted as τ_e based on the following equation:[207, 212]

$$\tau_e = \frac{K_s}{J}\ln(J)I_S + \frac{G_s}{J}\left(\frac{B_s}{J} - \frac{1}{2}tr\left(\frac{B_s}{J}\right)I_S\right)$$

(12)

Here, K_s denotes the dilatational modulus at the interface, while G_s represents the shear modulus at the interface. The relevant deformations are characterized by the left-Cauchy-Green interfacial strain tensor, denoted as $B_s = F_S {F_S}^T$. Here, F_S stands for the 2-dimensional interfacial deformation gradient tensor, defined as $F_S = \partial \mathrm{r}/\partial \mathrm{R}$, with r and R representing the position vectors in the deformed and reference configurations, respectively. Additionally, J signifies the relative area deformation, which can be expressed as $J = \det{(F_S)}$.

In practical applications, the models outlined in equations 11-12 require material properties (η_s, κ_s, K_s, G_s) or more intricate material functions. These parameters are measured under precisely defined kinematic conditions and serve as inputs for the models. Thorough explanations of these models, including their physical foundations and advanced methods for characterizing interfacial rheology, can be found in the comprehensive review by Jaensson and Vermant.[207]

6.2.3.1 Interfacial rheometry at constant area

To evaluate the mechanical properties of an interface, interfacial rheology tests can be performed on artificially flat interfaces instead of the complex, curved interfaces typically found in real-life applications.[207] This approach, known as interfacial shear rheometry, relies on measuring the response of a flat interface to deformation while maintaining a constant area. In practice, many devices proposed for interfacial shear rheometry mimic concepts used by conventional rheometers for evaluating bulk fluids. These setups, along with their operational principles and limitations, have been recently assessed in a review article presented by Jaensson and Vermant.[207]

The magnetic trap interfacial rod rheometer, otherwise known as the interfacial stress rheometer (ISR), is among the simplest geometries for evaluating the rheological properties of complex fluids, especially at fluid-fluid interfaces.[213-215] In this system, a slender rod or wire is suspended in the fluid using a magnetic field. The rod is often coated with a thin layer of magnetic material. By applying a magnetic field, the rod experiences torque or force, depending on the rheological properties of the surrounding fluid. The response of the rod to this force provides insights into interfacial rheology, including surface tension and elasticity. Over the last couple of decades, several studies have focused on developing mathematical theories that interpret the flow/velocity profile of ISRs to achieve conditions under which reliable interfacial rheology measurements can be obtained.[213-215] This comprehensive numerical and experimental investigation led to advancements in needle design, such as centralizing the magnetic component or incorporating magnetic micro-wires or nanorods. These modifications significantly boosted the devices' sensitivity.[207]

In this context, the magnetic button rheometer represents a significant advancement in sensitivity when compared to conventional magnetic trap interfacial rod rheometers. This configuration typically features a small circular disc or button-shaped geometry that can be rotated at the fluid-fluid interface, enabling the measurement of surface viscosities. Choi et al.[216] integrated this geometry with fluorescence microscopy, providing a means to visualize fluid interfaces undergoing deformation under applied stress. This innovative approach allows for the correlation of structure and rheology on a micron-scale in monolayer films. In their study, ferromagnetic micro-buttons with amphiphilic surface chemistry were intricately designed using photolithography techniques (see Figures 37 f-g). The material of interest is positioned on or around the micro-button, and electromagnets apply a known torque to rotate it at the interface. The buttonholes are then traced to record angular displacement over time. The outcome is a micron-scale rheometer capable of measuring surface viscosities of soft interfaces while simultaneously monitoring the evolution of the interfacial microstructure through fluorescence microscopy. Up to now, this rheometer has been used for evaluating the interfacial rheology in various biological or industrial relevant systems, e.g., phase-separated phospholipid monolayers, mixed monolayers of fibrinogen and dipalmitoylphosphatidylcholine as the main constituent of lung surfactants, and asphaltenes at the oil/water interface.[14, 216-218]

Despite these advancements, both magnetic button and magnetic trap interfacial rod rheometers are most effective for assessing systems characterized by low values of interfacial moduli and viscosities.[207] In response to this limitation, the double-wall geometry was devised to evaluate interfaces exhibiting higher moduli. This configuration typically features two concentric cylindrical walls, forming a ring-like structure. The enclosed space created between the outer and inner walls allows for precise measurements of rheological parameters at fluid interfaces. Vandebril et al.[219] integrated the double-wall geometry with a rotational rheometer to assess the rheological properties of complex fluid interfaces. They conducted both rotational and oscillatory experiments on viscous and viscoelastic air/water and oil/water interfaces, demonstrating the versatility of this approach. Similarly, a double-wall Du Noüy ring can be coupled with a conventional rotational rheometer for evaluating systems characterized by high interfacial moduli and viscosities, particularly for samples with limited volumes.[207, 220] While previous studies have outlined flow/velocity field calculations to derive true shear rates based on these systems, a noteworthy aspect is that the liquid cells in these systems can be designed to exchange materials with the surrounding bulk environment. This feature enables the investigation of various parameters, including pH, and their effects on interfacial rheology in these systems.

6.2.3.2 Interfacial rheometry at changing area using droplet shape analysis

Dilation/compression interfacial rheology typically involves the study of the mechanical properties of interfaces, e.g., liquid-liquid or liquid-gas interfaces, when subjected to changes in area or volume.[14, 207] The significance of this approach becomes particularly pronounced when delving into the realm of nanoscale interfacial assemblies. By dilating or compressing the interface, the concentration and surface coverage of active materials at the interface change, creating additional factors that affect the surface stresses and rheology of the liquid-fluid interface. Recently, Jaensson and Vermant[207] reviewed several approaches regarding interfacial rheometry under changing area conditions, including drop/bubble-based methods, capillary pressure tensiometry, drop shape rheometry, and troughs with pure dilatation.[212, 221-224] Among these methods, drop shape rheometry stands out as a straightforward approach for evaluating the mechanical characteristics of complex interfaces containing surface-active materials under dilation or compression. Utilizing a simple pendant drop tensiometer coupled with image processing, this method offers a direct and accessible means to assess the mechanical properties of interfaces experiencing dynamic changes in their area or volume.

In this regard, Knoche et al.[222] advanced a fitting procedure based on image analysis to examine the mechanical characteristics of the interface based on the wrinkles that form at a buckled interface. In their study, pendant drops with elastic interfaces were affixed to a capillary tube and contracted by sucking some of the enclosed media back into the tube. Thereafter, by probing the pendant drop's shape and wrinkling patterns, the elastic characteristics of the interface, including the surface Young modulus (Y_{2D}), describing the membrane's resistance to stretching, the Poisson ratio (υ_{2D}) describing the lateral contraction upon stretching, and the bending modulus of the interface (E_B), were obtained (Figure 37h). This method particularly attracted our attention as it only requires a simple, off-the-shelf, entry-level tensiometer. Besides, the same research group recently released open-source software to analyze the mechanical characteristics of pendant drops with solid-like skins using non-linear constitutive models such as the non-linear Hookean, neo-Hookean, and Mooney-Rivlin models.[225] They conclude that non-linear Hookean elasticity is the best option for analyzing the elastic interface of pendant drops, especially as this method requires minimum computational costs. However, coupling more advanced constitutive models is quite intriguing for future studies.[207] Besides, the above-mentioned computational platforms assume that the initial state of the system is stress-free, while this scenario is hard and sometimes impractical to achieve, especially in the case of NPS assemblies at liquid-liquid interfaces.

Solving the problem mentioned above, i.e., the requirement of a stress-free initial state for analyzing the elastic behavior of a liquid-liquid interface, began with a study by Danov et al.[226] In this study, a pressure transducer was attached to the droplet side of a pendant drop tensiometer to measure the Laplace pressure directly and, consequently, the surface stress. Combining this upgraded tensiometer with image analysis, they were able to directly assess the stress field at the oil/water interface and its degree of anisotropy. Subsequently, Nagal et al.[196] integrated a similar methodology with an innovative constitutive model and fitting procedure using a spectral method to precisely derive the curvature of a pendant drop with minimized noise. The primary benefit of this technique, referred to as stress-fitting elastometry (SFE), lies in its ability to eliminate the contribution of surface tension to isotropic stress by conducting the analysis at two distinct compression states. This eliminates the necessity for a stress-free initial state, thereby lifting the constraint mentioned earlier in evaluating the mechanical characteristics of an interface through droplet shape evaluation.

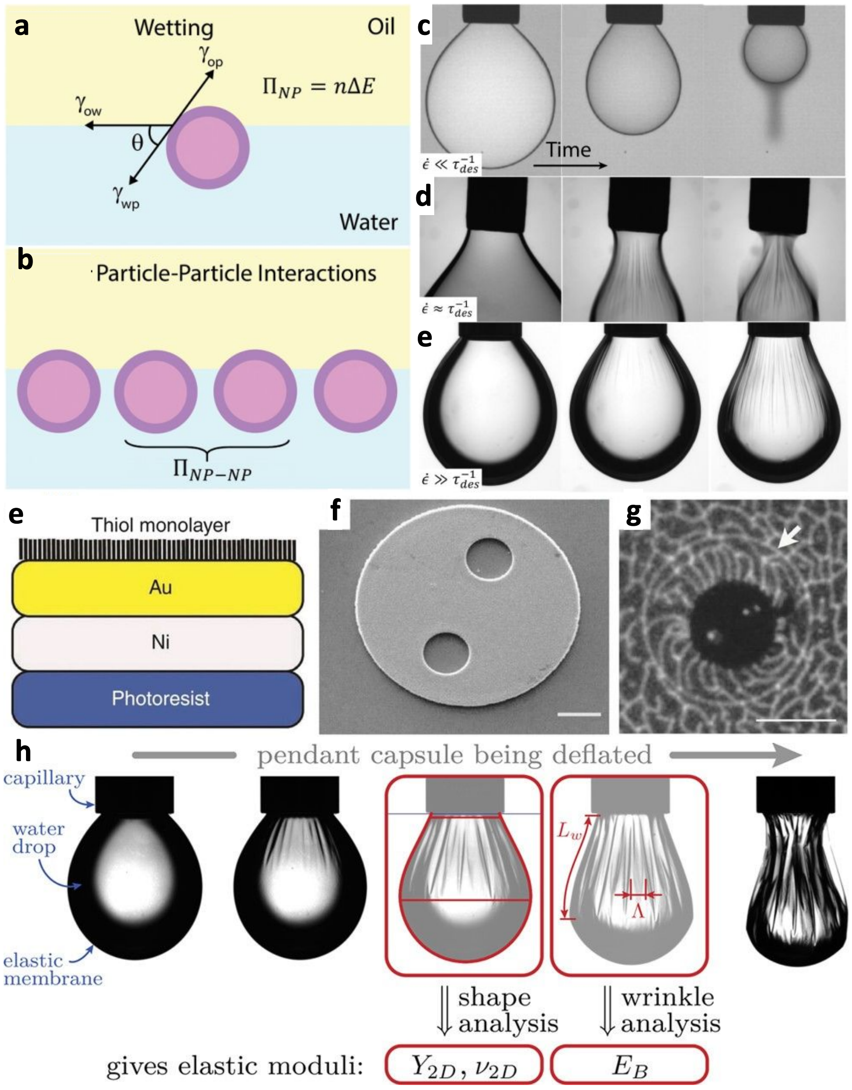

Figure 37: Macroscopic evaluation of nanoscale assemblies at liquid-liquid interfaces. (a) Segregating nanoparticles into the liquid-liquid interface and (b) nanoparticle-nanoparticle interaction at the interface as parameters that affect interfacial tension. (a-b) Reproduced with permission.[14] Copyright 2019, Wiley-VCH. During droplet contraction, its volume diminishes, resulting in a proportional reduction in interfacial area and the imposition of compressive forces on the interface. These compressive forces may cause (c) the desorption of active materials, (d) the formation of surface wrinkles at the liquid-liquid interface that subsequently undergoes relaxation and disappearance, and (e) the creation of permanent wrinkles that signify the irreversible bonding of active materials at the interface. (c) Reproduced with permission.[204] Copyright 2012, American Chemical Society. (d) Reproduced with permission.[205] Copyright 2014, American Chemical Society. (c-e) Reproduced with permission.[14] Copyright 2019, Wiley-VCH. (e-f) Ferromagnetic micro-buttons with amphiphilic surface chemistry were designed for a magnetic button rheometer. (g) A fluorescence microscopy image was captured from the shear rheology apparatus that features magnetic buttons. (e-g) Reproduced with permission.[216] Copyright 2011, Nature Publishing Group. (h) The elastic characteristics of the interface can be evaluated based on the pendant drop's shape and wrinkling patterns. (h) Reproduced with permission.[222] Copyright 2013, American Chemical Society.

7 Current challenges and prospects

In this article, we provided an overview of how the interfacial assembly of nanoparticles and supramolecules can be used to create functional and reconfigurable all-liquid structured systems. We discussed the fundamental chemistry of nanoscale components that adsorbed at liquid-liquid interfaces and explored how their collective behavior can transform the mechanical properties of these interfaces, leading to structured liquids exhibiting dual solid/liquid-like behavior. In these systems, the densely packed interfacial layer ensures structural stability, while the flowability within the compartmentalized liquid ensures adaptability comparable to that of traditional fluids. Furthermore, we discussed the reconfigurability and diverse applications of structured liquids, showcasing their potential to change our understanding of material and structural design across a spectrum of fields, including material encapsulation, soft robotics, microfluidics, and advanced electronics.

Starting with the interfacial assembly and jamming of NPSs, we have demonstrated the diverse range of nanoparticles and ligands that can be utilized to develop functional structured liquids. In these systems, the intrinsic characteristics of ligands and nanoparticles are synergistically combined to tailor the collective properties of the final constructs as needed. Nevertheless, we believe that there is significant potential for further advancements in the functionality of structured liquids. For instance, integrating magnetic, conductive, catalytic, or photoresponsive attributes with structured liquids could yield functionalities unparalleled by other material processing technologies. A notable example is our recent research on Janus structured liquid threads, where nanomaterials with distinct functionalities are precisely assigned to different parts of these structures at the macroscale.[3]

The potential of such Janus structures is immense. Imagine magnetic or conductive segments engineered to respond to stimuli selectively, bending in precise ways to encircle an object and transport it to a designated location. These are the foundational components for constructing soft robots. The range of possibilities expands further as we incorporate additional materials, particularly those with photocatalytic properties. In these designs, a magnetic segment could control the overall movement of the structure, while the photocatalytic side addresses environmental contaminants. Ultimately, the capacity to develop structured liquids with specialized functionalities offers a degree of flexibility that surpasses that of other soft functional materials.

More importantly, the behavior and characteristics of the liquid-liquid interface remain a complex subject within the realm of structured liquids, especially when NPSs are used to stabilize it. In this scenario, the assembly and behavior of nanoparticles depend on various parameters such as pH, ionic strength, temperature, and other external forces acting on the interface. As a result, in-situ and direct characterization of these interfacially active nanomaterials under various conditions is of utmost importance. In this context, the assembly and jamming of functionalized silica nanoparticles at the liquid-liquid interface have been explored in-situ by AFM.[187] However, there is still much work to be done in characterizing the interfacial assemblies of nanoparticles in aqueous-aqueous systems, and more importantly, other types of nanomaterials, including 2D graphene, GO, and MXenes, should be visually characterized. In this respect, characterizing the interfacial assembly of 0D nanomaterials such as graphene quantum dots (GQD) that possess specific functionalities required for interfacial assembly is quite interesting. Although assembling such materials at the liquid-liquid interface to achieve structured liquids can be quite challenging due to their small size, incorporating them can lead to a wide range of applications, including cargo delivery, environmental remediation, and liquid color change layers for LEDs.[227]

On the other hand, supramolecular assemblies, when compared to NPS jamming, offer a direct route to prepare structured liquids capable of withstanding both compressive and expansive forces. However, future studies in this field should focus on the choice of molecules and monomers when designing these systems. More importantly, this class of interfacial assemblies should be extended to water/water systems, where unique applications such as enzyme immobilization and encapsulation of living matter can be realized.

In-situ characterization of supramolecular assemblies, with a particular focus on the early-stage assembly, is another topic worth highlighting. In this regard, we can think about in-situ liquid cell transmission microscopy that, upon coupling with custom-made liquid cells capable of injecting a droplet of liquid phase into another phase and contracting it on demand, could be quite interesting. However, in this scenario, special attention should be devoted to the possible damage of electron beams to assemblies in order to gain a clear vision regarding the complex kinetics of supramolecular assemblies.

Finally, the reconfigurability of both NPSs and supramolecular assemblies deserves attention in future studies. To date, there has been limited information on stimuli-responsive water-in-water structured liquids that have many applications in fields related to living matter and cargo delivery in biological environments. In this regard, developing water-soluble ligands that can interact with functional nanomaterials in water-water systems or developing stimuli-responsive all-aqueous supramolecular assemblies remains an outstanding topic in this field.

In addition, particular emphasis should be placed on stimuli itself, as each type of stimulus comes with its own set of limitations. For example, temperature-responsive structures suffer from a relatively longer response time and are sensitive to environmental changes, whereas light-responsive structures are constrained by specific material types and vulnerable to ambient light conditions.[124] Electric or magnetic fields also incur energy and equipment costs, significantly restricting their applications. On the other hand, internal stimuli such as pH and redox reactions are easier to achieve by simply altering the conditions between acidic/base or oxidation/reduction, respectively. However, the concept of introducing a material to alter system behavior seems constrained for large-scale industrial applications.

In this context, the development of systems that respond to multiple external or internal stimuli simultaneously is highly intriguing. Such systems, if strategically designed, could leverage the benefits of various stimuli while compensating for their individual limitations in terms of application scope. This approach enhances the versatility and adaptability of these systems, making them more effective across a broader range of applications. In this vein, we can look to the work of Yang et al.[153], who developed structured liquids responsive to various stimuli, including redox potential, pH, and voltage, providing multiple pathways to control NPS assembly at the interface and transition them from a jammed to an unjammed state.

Overall, we believe that the field of structured liquids holds the potential to advance the domain of soft materials and structural design. The functionality and reconfigurability of these constructs can be finely tuned to meet specific needs, a critical capability not offered by other types of soft materials. Future research focused on incorporating diverse functionalities into structured liquids, along with efforts to characterize these assemblies thoroughly, has the potential to further elevate this emerging field in materials science. These advancements could transition structured liquids from laboratory research to practical applications, marking a significant milestone in their development.

Acknowledgments

A.G., S.A.H., A.I., and M.A. express gratitude for the financial support from the Natural Sciences and Engineering Research Council of Canada (NSERC) under funding reference numbers ALLRP 555586-20 and 569824-21. A.G., M.P., and O.J.R. extend their thanks for the funding support from the Canada Excellence Research Chair Program (CERC-2018-00006) and the Canada Foundation for Innovation (Project number 38623). M.A. acknowledges the Canada Research Chairs program (CRC-2018-00234) for their financial assistance. T.P.R. received support from the U.S. Department of Energy, Office of Science, Office of Basic Energy Sciences, Materials Sciences and Engineering Division under Contract No. DE-AC02-05-CH11231 within the Adaptive Interfacial Assemblies Towards Structuring Liquids program (KCTR16). The authors also acknowledge the Syilx Okanagan and Musqueam Nations for graciously allowing the use of their traditional, ancestral, and unceded territory for the research activities.

References

1. S. Shi and T. P. Russell, *Adv. Mater.*, 2018, **30**, 1800714.
2. Y. Yang, Z. Xia, Y. Luo, Z. Wu, S. Shi and T. P. Russell, *Supramolecular Materials*, 2022, 100013.
3. A. Ghaffarkhah, S. A. Hashemi, F. Ahmadijokani, M. Goodarzi, H. Riazi, S. E. Mhatre, O. Zaremba, O. J. Rojas, M. Soroush and T. P. Russell, *Nat. Commun.*, 2023, **14**, 7811.
4. X. Wu, H. Xue, Z. Fink, B. A. Helms, P. D. Ashby, A. K. Omar and T. P. Russell, *Angew. Chem.*, 2024, e202403790.
5. S. Zhao, J.-Y. Zhang, Y. Fu, S. Zhu, H. C. Shum, X. Liu, Z. Wang, R. Ye, B. Z. Tang and T. P. Russell, *Nano Lett.*, 2022, **22**, 5538-5543.
6. J. Forth, X. Liu, J. Hasnain, A. Toor, K. Miszta, S. Shi, P. L. Geissler, T. Emrick, B. A. Helms and T. P. Russell, *Adv. Mater.*, 2018, **30**, 1707603.
7. A. Toor, S. Lamb, B. A. Helms and T. P. Russell, *ACS nano*, 2018, **12**, 2365-2372.
8. C. Huang, Z. Sun, M. Cui, F. Liu, B. A. Helms and T. P. Russell, *Advanced Materials*, 2016, **28**, 6612-6618.
9. S. Shi, X. Liu, Y. Li, X. Wu, D. Wang, J. Forth and T. P. Russell, *Advanced Materials*, 2018, **30**, 1705800.
10. W. Feng, Y. Chai, J. Forth, P. D. Ashby, T. P. Russell and B. A. Helms, *Nat. Commun.*, 2019, **10**, 1-9.
11. C. Huang, J. Forth, W. Wang, K. Hong, G. S. Smith, B. A. Helms and T. P. Russell, *Nat. Nanotechnol.*, 2017, **12**, 1060-1063.
12. P. Gu, X. Luo, S. Zhou, D. Wang, Z. Li, Y. Chai, Y. Zhang, S. Shi and T. P. Russell, *Angewandte Chemie International Edition*, 2023, **62**, e202303789.

13. P. Y. Gu, P. Y. Kim, Y. Chai, P. D. Ashby, Q. F. Xu, F. Liu, Q. Chen, J. M. Lu and T. P. Russell, *Small*, 2022, **18**, 2105017.
14. J. Forth, P. Y. Kim, G. Xie, X. Liu, B. A. Helms and T. P. Russell, *Adv. Mater.*, 2019, **31**, 1806370.
15. D. Popple, M. Shekhirev, C. Dai, P. Kim, K. X. Wang, P. Ashby, B. A. Helms, Y. Gogotsi, T. P. Russell and A. Zettl, *Adv. Mater.*, 2023, **35**, 2208148.
16. J. Yan, M. A. Baird, D. C. Popple, A. Zettl, T. P. Russell and B. A. Helms, *J. Am. Chem. Soc.*, 2022, **144**, 3979-3988.
17. S. Sun, S. Li, W. Feng, J. Luo, T. P. Russell and S. Shi, *Nat. Commun.*, 2024, **15**, 1058.
18. S. Zhu, G. Xie, H. Cui, Q. Li, J. Forth, S. Yuan, J. Tian, Y. Pan, W. Guo and Y. Chai, *ACS nano*, 2022, **16**, 13761-13770.
19. A. Ghaffarkhah, S. A. Hashemi, S. Rostami, M. Amini, F. Ahmadijokani, A. Pournaghshband Isfahani, S. E. Mhatre, O. J. Rojas, M. Kamkar and S. Wuttke, *Adv. Funct. Mater.*, 2023, **33**, 2304748.
20. Z. Yang, J. Wei, Y. I. Sobolev and B. A. Grzybowski, *Nature*, 2018, **553**, 313-318.
21. T. Liu, Y. Yin, Y. Yang, T. P. Russell and S. Shi, *Adv. Mater.*, 2022, **34**, 2105386.
22. Y. Lin, H. Skaff, A. Böker, A. Dinsmore, T. Emrick and T. P. Russell, *J. Am. Chem. Soc.*, 2003, **125**, 12690-12691.
23. Y. Lin, H. Skaff, T. Emrick, A. Dinsmore and T. P. Russell, *Science*, 2003, **299**, 226-229.
24. A. Böker, J. He, T. Emrick and T. P. Russell, *Soft matter*, 2007, **3**, 1231-1248.
25. Y. Lin, A. Böker, H. Skaff, D. Cookson, A. Dinsmore, T. Emrick and T. P. Russell, *Langmuir*, 2005, **21**, 191-194.
26. F. Reincke, S. G. Hickey, W. K. Kegel and D. Vanmaekelbergh, *Angewandte Chemie-International Edition*, 2004, **43**, 458-462.
27. H. Duan, D. Wang, D. G. Kurth and H. Möhwald, *Angew. Chem. Int. Ed.*, 2004, **43**, 5639-5642.
28. Y. J. Li, W. J. Huang and S. G. Sun, *Angew. Chem. Int. Ed.*, 2006, **45**, 2537-2539.
29. P.-P. Fang, S. Chen, H. Deng, M. D. Scanlon, F. Gumy, H. J. Lee, D. Momotenko, V. Amstutz, F. Cortés-Salazar and C. M. Pereira, *ACS nano*, 2013, **7**, 9241-9248.
30. Y.-K. Park, S.-H. Yoo and S. Park, *Langmuir*, 2007, **23**, 10505-10510.
31. S. Biswas and L. T. Drzal, *Nano Lett.*, 2009, **9**, 167-172.
32. L. Hu, L. Wu, M. Liao and X. Fang, *Adv. Mater.*, 2011, **17**, 1988-1992.
33. M. Chen, L. Hu, J. Xu, M. Liao, L. Wu and X. Fang, *Small (Weinheim an der Bergstrasse, Germany)*, 2011, **7**, 2449-2453.
34. H. Chen, L. Hu, X. Fang and L. Wu, *Adv. Funct. Mater.*, 2012, **22**, 1229-1235.
35. R. Ma, M. Osada, L. Hu and T. Sasaki, *Chem. Mater.*, 2010, **22**, 6341-6346.
36. H. M. Jaeger, *Soft matter*, 2015, **11**, 12-27.
37. A. J. Liu and S. R. Nagel, *Nature*, 1998, **396**, 21-22.
38. L. Li, Z. Deng, M. Chen, Z.-Z. Yu, T. P. Russell and H.-B. Zhang, *Nano Lett.*, 2022, **23**, 155-162.
39. B. Wu, C. Yang, Q. Xin, L. Kong, M. Eggersdorfer, J. Ruan, P. Zhao, J. Shan, K. Liu and D. Chen, *Advanced Materials*, 2021, **33**, 2102362.
40. S. A. Hashemi, A. Ghaffarkhah, M. Goodarzi, A. Nazemi, G. Banvillet, A. S. Milani, M. Soroush, O. J. Rojas, S. Ramakrishna and S. Wuttke, *Adv. Mater.*, 2023, **35**, 2302826.
41. M. Cui, T. Emrick and T. P. Russell, *Science*, 2013, **342**, 460-463.
42. C. Huang, M. Cui, Z. Sun, F. Liu, B. A. Helms and T. P. Russell, *Langmuir*, 2017, **33**, 7994-8001.
43. H. Yao, O. Momozawa, T. Hamatani and K. Kimura, *Bulletin of the Chemical Society of Japan*, 2000, **73**, 2675-2678.
44. S. Chen, H. Yao and K. Kimura, *Langmuir*, 2001, **17**, 733-739.
45. D. G. Kurth, P. Lehmann and C. Lesser, *Chemical Communications*, 2000, 949-950.
46. H. Yao, O. Momozawa, T. Hamatani and K. Kimura, *Chemistry of materials*, 2001, **13**, 4692-4697.

47. T. Feng, D. A. Hoagland and T. P. Russell, *Langmuir*, 2014, **30**, 1072-1079.
48. T. Feng, D. A. Hoagland and T. P. Russell, *Soft Matter*, 2016, **12**, 8701-8709.
49. Y. Chai, A. Lukito, Y. Jiang, P. D. Ashby and T. P. Russell, *Nano Lett.*, 2017, **17**, 6453-6457.
50. B. P. Binks, J. A. Rodrigues and W. J. Frith, *Langmuir*, 2007, **23**, 3626-3636.
51. B. P. Binks and J. A. Rodrigues, *Langmuir*, 2007, **23**, 7436-7439.
52. D. Lin, T. Liu, Q. Yuan, H. Yang, H. Ma, S. Shi, D. Wang and T. P. Russell, *ACS applied materials & interfaces*, 2020, **12**, 55426-55433.
53. R. Xu, T. Liu, H. Sun, B. Wang, S. Shi and T. P. Russell, *ACS Appl. Mater. Interfaces.*, 2020, **12**, 18116-18122.
54. M. Kamkar, E. Erfanian, P. Bazazi, A. Ghaffarkhah, F. Sharif, G. Xie, A. Kannan, M. Arjmand, S. H. Hejazi and T. P. Russell, *Adv. Mater. Interfaces.*, 2022, **9**, 2101659.
55. M. Kamkar, A. Ghaffarkhah, R. Ajdary, Y. Lu, F. Ahmadijokani, S. E. Mhatre, E. Erfanian, U. Sundararaj, M. Arjmand and O. J. Rojas, *Small*, 2022, **18**, 2200220.
56. S. A. Hashemi, A. Ghaffarkhah, F. Ahmadijokani, H. Yousefian, S. E. Mhatre, A. Sinelshchikova, G. Banvillet, M. Kamkar, O. J. Rojas and S. Wuttke, *Nanoscale*, 2024.
57. X. Xie, Z. Xu, X. Yu, H. Jiang, H. Li and W. Feng, *Nature Communications*, 2023, **14**, 4289.
58. X. Liu, S. Shi, Y. Li, J. Forth, D. Wang and T. P. Russell, *Angew. Chem.*, 2017, **129**, 12768-12772.
59. A. Toor, B. A. Helms and T. P. Russell, *Nano letters*, 2017, **17**, 3119-3125.
60. Y. Zhang, G. Zhu, B. Dong, F. Wang, J. Tang, F. J. Stadler, G. Yang, S. Hong and F. Xing, *Nature communications*, 2021, **12**, 111.
61. S. U. Pickering, *J. Chem. Soc., Trans*, 1907, **91**, 2001-2021.
62. B. P. Binks, *Current opinion in colloid & interface science*, 2002, **7**, 21-41.
63. R. Aveyard, B. P. Binks and J. H. Clint, *Advances in colloid and interface science*, 2003, **100**, 503-546.
64. P. Finkle, H. D. Draper and J. H. Hildebrand, *Journal of the American Chemical Society*, 1923, **45**, 2780-2788.
65. J. H. Schulman and J. Leja, *transactions of the Faraday society*, 1954, **50**, 598-605.
66. Y. Liu, Z. Xu, W. Gao, Z. Cheng and C. Gao, *Advanced Materials*, 2017, **29**, 1606794.
67. S. Naficy, R. Jalili, S. H. Aboutalebi, R. A. Gorkin III, K. Konstantinov, P. C. Innis, G. M. Spinks, P. Poulin and G. G. Wallace, *Materials Horizons*, 2014, **1**, 326-331.
68. D. T. Chen, Q. Wen, P. A. Janmey, J. C. Crocker and A. G. Yodh, *Annu. Rev. Condens. Matter Phys.*, 2010, **1**, 301-322.
69. S. Shi, B. Qian, X. Wu, H. Sun, H. Wang, H. B. Zhang, Z. Z. Yu and T. P. Russell, *Angew. Chem. Int. Ed.*, 2019, **58**, 18171-18176.
70. Z. Sun, T. Feng and T. P. Russell, *Langmuir*, 2013, **29**, 13407-13413.
71. B. E. Rapp, *Microfluidics: modeling, mechanics and mathematics*, Elsevier, 2022.
72. O. Breslouer, *Project Report*, 2010.
73. Y. Yan, J. Gong, J. Chen, Z. Zeng, W. Huang, K. Pu, J. Liu and P. Chen, *Adv. Mater.*, 2019, **31**, 1808283.
74. L. Li, H. Sun, M. Li, Y. Yang, T. P. Russell and S. Shi, *Angew. Chem. Int. Ed.*, 2021, **60**, 17394-17397.
75. S. Zhao, L. Li, H.-B. Zhang, B. Qian, J.-Q. Luo, Z. Deng, S. Shi, T. P. Russell and Z.-Z. Yu, *Materials Chemistry Frontiers*, 2020, **4**, 910-917.
76. J. D. Cain, A. Azizi, K. Maleski, B. Anasori, E. C. Glazer, P. Y. Kim, Y. Gogotsi, B. A. Helms, T. P. Russell and A. Zettl, *ACS nano*, 2019, **13**, 12385-12392.
77. X. Hui, X. Ge, R. Zhao, Z. Li and L. Yin, *Adv. Funct. Mater.*, 2020, **30**, 2005190.
78. C. J. Zhang, *Journal of Energy Chemistry*, 2021, **60**, 417-434.
79. M. E. Cates and P. S. Clegg, *Soft Matter*, 2008, **4**, 2132-2138.

80. A. Mohraz, *Current Opinion in Colloid & Interface Science*, 2016, **25**, 89-97.
81. A. Mohraz, *Nature Nanotechnology*, 2017, **12**, 1021-1022.
82. M. Reeves, A. Brown, A. B. Schofield, M. Cates and J. Thijssen, *Physical Review E*, 2015, **92**, 032308.
83. M. Reeves, K. Stratford and J. H. Thijssen, *Soft Matter*, 2016, **12**, 4082-4092.
84. V. Jhawat, M. Gulia and A. K. Sharma, in *Chemoinformatics and Bioinformatics in the Pharmaceutical Sciences*, Elsevier, 2021, pp. 455-481.
85. J. Ahmad, S. Amin, K. Kohli and S. R. Mir, *Int. J. Drug Dev. Res*, 2013, **5**, 84-90.
86. M. Gradzielski, M. Duvail, P. M. de Molina, M. Simon, Y. Talmon and T. Zemb, *Chemical reviews*, 2021, **121**, 5671-5740.
87. E. M. Herzig, K. White, A. B. Schofield, W. C. Poon and P. S. Clegg, *Nature materials*, 2007, **6**, 966-971.
88. B. Kinkead, R. Malone, G. Smith, A. Pandey and M. Trifkovic, *Chemistry of Materials*, 2019, **31**, 7601-7607.
89. Y. Xi, R. S. Lankone, L.-P. Sung and Y. Liu, *Nature communications*, 2021, **12**, 910.
90. Y. Lu, M. Kamkar, S. Guo, X. Niu, Z. Wan, J. Xu, X. Su, Y. Fan, L. Bai and O. J. Rojas, *Small*, 2023, 2300686.
91. D. Cai, F. H. Richter, J. H. Thijssen, P. G. Bruce and P. S. Clegg, *Materials Horizons*, 2018, **5**, 499-505.
92. M. F. Haase, K. J. Stebe and D. Lee, *Advanced Materials*, 2015, **27**, 7065-7071.
93. S. Guo, H. Tao, G. Gao, S. Mhatre, Y. Lu, A. Takagi, J. Li, L. Mo, O. J. Rojas and G. Chu, *Biomacromolecules*, 2022, **24**, 367-376.
94. S. A. Vitale and J. L. Katz, *Langmuir*, 2003, **19**, 4105-4110.
95. M. A. Khan, A. J. Sprockel, K. A. Macmillan, M. T. Alting, S. P. Kharal, S. Boakye-Ansah and M. F. Haase, *Advanced Materials*, 2022, **34**, 2109547.
96. M. F. Haase, N. Sharifi-Mood, D. Lee and K. J. Stebe, *ACS nano*, 2016, **10**, 6338-6344.
97. S. P. Kharal and M. F. Haase, *Small*, 2022, **18**, 2106826.
98. M. F. Haase, H. Jeon, N. Hough, J. H. Kim, K. J. Stebe and D. Lee, *Nature communications*, 2017, **8**, 1234.
99. A. V. Davis, R. M. Yeh and K. N. Raymond, *Proceedings of the National Academy of Sciences*, 2002, **99**, 4793-4796.
100. Z. Liu and Y. Liu, *Chemical Society Reviews*, 2022, **51**, 4786-4827.
101. D. Truzzolillo, S. Mora, C. Dupas and L. Cipelletti, *Physical Review X*, 2016, **6**, 041057.
102. Z. Niroobakhsh, J. A. LaNasa, A. Belmonte and R. J. Hickey, *Physical review letters*, 2019, **122**, 178003.
103. X. Yan, F. Wang, B. Zheng and F. Huang, *Chemical Society Reviews*, 2012, **41**, 6042-6065.
104. I. Insua, J. Bergueiro, A. Méndez-Ardoy, I. Lostalé-Seijo and J. Montenegro, *Chemical Science*, 2022, **13**, 3057-3068.
105. H. Hou, J. Li, X. Li, J. Forth, J. Yin, X. Jiang, B. A. Helms and T. P. Russell, *Angew. Chem.*, 2019, **131**, 10248-10253.
106. R. Varshney, C. Agashe, A. K. Gill, M. Alam, R. Joseph and D. Patra, *Chemical Communications*, 2021, **57**, 10604-10607.
107. Y. Hata, S. Yoneda, S. Tanaka, T. Sawada and T. Serizawa, *Journal of Colloid and Interface Science*, 2021, **590**, 487-494.
108. H. Kamada, Y. Hata, K. Sugiura, T. Sawada and T. Serizawa, *Carbohydrate Polymers*, 2024, **331**, 121896.
109. Y. Zheng, Z. Yu, R. M. Parker, Y. Wu, C. Abell and O. A. Scherman, *Nature communications*, 2014, **5**, 5772.

110. M. Pfeffermann, R. Dong, R. Graf, W. Zajaczkowski, T. Gorelik, W. Pisula, A. Narita, K. Müllen and X. Feng, *Journal of the American Chemical Society*, 2015, **137**, 14525-14532.
111. J. Zhang, R. J. Coulston, S. T. Jones, J. Geng, O. A. Scherman and C. Abell, *Science*, 2012, **335**, 690-694.
112. J. W. Steed and J. L. Atwood, *Supramolecular chemistry*, John Wiley & Sons, 2022.
113. P. Jonkheijm, P. van der Schoot, A. P. Schenning and E. Meijer, *Science*, 2006, **313**, 80-83.
114. P. A. Korevaar, S. J. George, A. J. Markvoort, M. M. Smulders, P. A. Hilbers, A. P. Schenning, T. F. De Greef and E. Meijer, *Nature*, 2012, **481**, 492-496.
115. P. Y. Gu, Y. Chai, H. Hou, G. Xie, Y. Jiang, Q. F. Xu, F. Liu, P. D. Ashby, J. M. Lu and T. P. Russell, *Angewandte Chemie International Edition*, 2019, **58**, 12112-12116.
116. M. Sayed and H. Pal, *Physical Chemistry Chemical Physics*, 2021, **23**, 26085-26107.
117. M. D. Pluth and K. N. Raymond, *Chemical Society Reviews*, 2007, **36**, 161-171.
118. T.-H. Shi, S. Ohtani, K. Kato, S. Fa and T. Ogoshi, *Trends in Chemistry*, 2023.
119. B. Tang, J. Zhao, J. F. Xu and X. Zhang, *Chemistry–A European Journal*, 2020, **26**, 15446-15460.
120. Q.-D. Hu, G.-P. Tang and P. K. Chu, *Accounts of chemical research*, 2014, **47**, 2017-2025.
121. B. Wang, H. Chen, T. Liu, S. Shi and T. P. Russell, *Engineering*, 2021, **7**, 603-614.
122. M. J. Webber and R. Langer, *Chemical Society Reviews*, 2017, **46**, 6600-6620.
123. G. Fang, X. Yang, S. Chen, Q. Wang, A. Zhang and B. Tang, *Coordination Chemistry Reviews*, 2022, **454**, 214352.
124. Y. Fu, S. Zhao, W. Chen, Q. Zhang and Y. Chai, *Nano Today*, 2024, **54**, 102073.
125. Z. Xia, Y. Yang, Y.-F. Song and S. Shi, *ACS Macro Letters*, 2024, **13**, 99-104.
126. K. P. Xie, Z. Y. Ruan, B. H. Lyu, X. X. Chen, X. W. Zhang, G. Z. Huang, Y. C. Chen, Z. P. Ni and M. L. Tong, *Angew. Chem.*, 2021, **133**, 27350-27356.
127. K. Bujak, H. Orlikowska, J. G. Małecki, E. Schab-Balcerzak, S. Bartkiewicz, J. Bogucki, A. Sobolewska and J. Konieczkowska, *Dyes and Pigments*, 2019, **160**, 654-662.
128. H. Sun, L. Li, T. P. Russell and S. Shi, *J. Am. Chem. Soc.*, 2020, **142**, 8591-8595.
129. S. Yang, W. Qin, X. Zhao, F. He, H. Liu, Q. Zhou, J. Huang, G. Yu, Y. Feng and J. Li, *J. Colloid Interface Sci.*, 2023, **645**, 580-590.
130. Z. Li, Y. Shi, A. Zhu, Y. Zhao, H. Wang, B. P. Binks and J. Wang, *Angew. Chem.*, 2021, **133**, 3974-3979.
131. J. G. Hardy, M. Palma, S. J. Wind and M. J. Biggs, *Adv. Mater.*, 2016, **28**, 5717-5724.
132. Y. Tan, Y. Zhang, Y. Zhang, J. Zheng, H. Wu, Y. Chen, S. Xu, J. Yang, C. Liu and Y. Zhang, *Chem. Mater.*, 2020, **32**, 7670-7678.
133. H. Hemmatpour, V. Haddadi-Asl, T. C. Burgers, F. Yan, M. C. Stuart, C. Reker-Smit, R. Vlijm, A. Salvati and P. Rudolf, *Nanoscale*, 2023, **15**, 2402-2416.
134. X. Pei, K. Zhai, C. Wang, Y. Deng, Y. Tan, B. Zhang, Y. Bai, K. Xu and P. Wang, *Langmuir*, 2019, **35**, 7222-7230.
135. X. Li, Y. Wang, Q. Hou, W. Cai, Y. Xu and Y. Zhao, *Research on Chemical Intermediates*, 2021, **47**, 3899-3917.
136. Z. Yu, Y. Lan, R. M. Parker, W. Zhang, X. Deng, O. A. Scherman and C. Abell, *Polymer Chemistry*, 2016, **7**, 5996-6002.
137. M. Ranka, H. Katepalli, D. Blankschtein and T. A. Hatton, *Langmuir*, 2017, **33**, 13326-13331.
138. B. Su, J.-P. Abid, D. J. Fermín, H. H. Girault, H. Hoffmannová, P. Krtil and Z. Samec, *J. Am. Chem. Soc.*, 2004, **126**, 915-919.
139. M. Janjua, S. Nudurupati, P. Singh and N. Aubry, *Electrophoresis*, 2011, **32**, 518-526.
140. M. K. Bera, H. Chan, D. F. Moyano, H. Yu, S. Tatur, D. Amoanu, W. Bu, V. M. Rotello, M. Meron and P. Král, *Nano Lett.*, 2014, **14**, 6816-6822.

141. W. Wang, J. V. Timonen, A. Carlson, D.-M. Drotlef, C. T. Zhang, S. Kolle, A. Grinthal, T.-S. Wong, B. Hatton and S. H. Kang, *Nature*, 2018, **559**, 77-82.
142. X. Wu, R. Streubel, X. Liu, P. Y. Kim, Y. Chai, Q. Hu, D. Wang, P. Fischer and T. P. Russell, *Proceedings of the National Academy of Sciences*, 2021, **118**, e2017355118.
143. X. Liu, N. Kent, A. Ceballos, R. Streubel, Y. Jiang, Y. Chai, P. Y. Kim, J. Forth, F. Hellman and S. Shi, *Science*, 2019, **365**, 264-267.
144. Z. Zhang, Y. Jiang, C. Huang, Y. Chai, E. Goldfine, F. Liu, W. Feng, J. Forth, T. E. Williams and P. D. Ashby, *Sci. Adv.*, 2018, **4**, eaap8045.
145. P. Liu, X. Pei, Z. Cui, B. Song, J. Jiang and B. P. Binks, *Langmuir*, 2023, **39**, 841-850.
146. K. Liu, J. Jiang, Z. Cui and B. P. Binks, *Langmuir*, 2017, **33**, 2296-2305.
147. J. Jiang, S. Yu, W. Zhang, H. Zhang, Z. Cui, W. Xia and B. P. Binks, *Angew. Chem. Int. Ed.*, 2021, **60**, 11793-11798.
148. J. Luo, M. Zeng, B. Peng, Y. Tang, L. Zhang, P. Wang, L. He, D. Huang, L. Wang and X. Wang, *Angew. Chem. Int. Ed.*, 2018, **57**, 11752-11757.
149. X. Xin, V. Kumar, F. Lin, V. Kumar, R. Bhattarai, V. R. Bhatt, C. Tan and R. I. Mahato, *Sci. Adv.*, 2020, **6**, eabd6764.
150. E. Mirhadi, M. Mashreghi, M. F. Maleki, S. H. Alavizadeh, L. Arabi, A. Badiee and M. R. Jaafari, *International journal of pharmaceutics*, 2020, **589**, 119882.
151. S. Sun, C. Xie, J. Chen, Y. Yang, H. Li, T. P. Russell and S. Shi, *Angew. Chem. Int. Ed.*, 2021, **60**, 26363-26367.
152. H. Sun, M. Li, L. Li, T. Liu, Y. Luo, T. P. Russell and S. Shi, *J. Am. Chem. Soc.*, 2021, **143**, 3719-3722.
153. Y. Yang, H. Sun, M. Wang, M. Li, Z. Zhang, T. P. Russell and S. Shi, *Angew. Chem. Int. Ed.*, 2023, **62**, e202218440.
154. G. Xie, J. Forth, Y. Chai, P. D. Ashby, B. A. Helms and T. P. Russell, *Chem*, 2019, **5**, 2678-2690.
155. C.-Y. Xie, S.-X. Meng, L.-H. Xue, R.-X. Bai, X. Yang, Y. Wang, Z.-P. Qiu, B. P. Binks, T. Guo and T. Meng, *Langmuir*, 2017, **33**, 14139-14148.
156. A. J. Zarbin, *Materials Horizons*, 2021, **8**, 1409-1432.
157. Y. Lu, Y. Chun, X. Shi, D. Wang, F. Ahmadijokani and O. J. Rojas, *Adv. Mater.*, 2024, 2400311.
158. V. E. Blair, K. Celebi, K. Müllen and J. Vermant, *Adv. Mater. Interfaces.*, 2019, **6**, 1801570.
159. V. Souza, S. Husmann, E. Neiva, F. Lisboa, L. Lopes, R. Salvatierra and A. Zarbin, *Electrochimica Acta*, 2016, **197**, 200-209.
160. B. Le Ouay, S. Guldin, Z. Luo, S. Allegri and F. Stellacci, *Adv. Mater. Interfaces.*, 2016, **3**, 1600191.
161. H. S. Sasmal, A. Halder, S. Kunjattu H, K. Dey, A. Nadol, T. G. Ajithkumar, P. Ravindra Bedadur and R. Banerjee, *J. Am. Chem. Soc.*, 2019, **141**, 20371-20379.
162. M. K. Jana, B. Murali, S. Krupanidhi, K. Biswas and C. Rao, *J. Mater. Chem. C.*, 2014, **2**, 6283-6289.
163. S.-Y. Zhang, J.-W. Liu, C.-L. Zhang and S.-H. Yu, *Nanoscale*, 2013, **5**, 4223-4229.
164. Y. Geng, M. Liu, K. Tong, J. Xu, Y.-I. Lee, J. Hao and H.-G. Liu, *Langmuir*, 2014, **30**, 2178-2187.
165. L. Hostert, E. G. Neiva, A. J. Zarbin and E. S. Orth, *J. Mater. Chem. A*, 2018, **6**, 22226-22233.
166. X. Li, Z. Huang, C. E. Shuck, G. Liang, Y. Gogotsi and C. Zhi, *Nature Reviews Chemistry*, 2022, **6**, 389-404.
167. K. R. G. Lim, M. Shekhirev, B. C. Wyatt, B. Anasori, Y. Gogotsi and Z. W. Seh, *Nature Synthesis*, 2022, **1**, 601-614.
168. S. Rostami, A. Ghaffarkhah, A. Isari, S. A. Hashemi and M. Arjmand, *Materials Advances*, 2023.
169. A. A. Isari, A. Ghaffarkhah, S. A. Hashemi, S. Wuttke and M. Arjmand, *Adv. Mater.*, 2024, 2310683.
170. A. Ghaffarkhah, M. Kamkar, Z. A. Dijvejin, H. Riazi, S. Ghaderi, K. Golovin, M. Soroush and M. Arjmand, *Carbon*, 2022, **191**, 277-289.

171. S. A. Hashemi, A. Ghaffarkhah, E. Hosseini, S. Bahrani, P. Najmi, N. Omidifar, S. M. Mousavi, M. Amini, M. Ghaedi and S. Ramakrishna, *Matter*, 2022, **5**, 3807-3868.
172. M. Kamkar, A. Ghaffarkhah, E. Hosseini, M. Amini, S. Ghaderi and M. Arjmand, *New J. Chem.*, 2021.
173. F. Schulz, I. Lokteva, W. J. Parak and F. Lehmkühler, *Particle & Particle Systems Characterization*, 2021, **38**, 2100087.
174. X. Lu, Y. Huang, B. Liu, L. Zhang, L. Song, J. Zhang, A. Zhang and T. Chen, *Chem. Mater.*, 2018, **30**, 1989-1997.
175. J. C. Meyer, C. O. Girit, M. Crommie and A. Zettl, *Nature*, 2008, **454**, 319-322.
176. M. P. Blakeley, S. S. Hasnain and S. V. Antonyuk, *IUCrJ*, 2015, **2**, 464-474.
177. H. Borchert, E. V. Shevchenko, A. Robert, I. Mekis, A. Kornowski, G. Grübel and H. Weller, *Langmuir*, 2005, **21**, 1931-1936.
178. H. Wu, H. Friedrich, J. P. Patterson, N. A. Sommerdijk and N. De Jonge, *Adv. Mater.*, 2020, **32**, 2001582.
179. V. Mihali and A. Honciuc, *Adv. Mater. Interfaces.*, 2022, **9**, 2101713.
180. V. N. Paunov, *Langmuir*, 2003, **19**, 7970-7976.
181. L. Isa, F. Lucas, R. Wepf and E. Reimhult, *Nat. Commun.*, 2011, **2**, 438.
182. L. N. Arnaudov, O. J. Cayre, M. A. C. Stuart, S. D. Stoyanov and V. N. Paunov, *Physical Chemistry Chemical Physics*, 2010, **12**, 328-331.
183. J. Vialetto, S. N. Ramakrishna and L. Isa, *Sci. Adv.*, 2022, **8**, eabq2019.
184. J. Vialetto, F. Camerin, S. N. Ramakrishna, E. Zaccarelli and L. Isa, *Adv. Sci*, 2023, **10**, 2303404.
185. L. Costa, G. Li-Destri, D. Pontoni, O. Konovalov and N. H. Thomson, *Adv. Mater. Interfaces.*, 2017, **4**, 1700203.
186. L. Costa, G. Li-Destri, N. H. Thomson, O. Konovalov and D. Pontoni, *Nano Lett.*, 2016, **16**, 5463-5468.
187. Y. Chai, J. Hasnain, K. Bahl, M. Wong, D. Li, P. Geissler, P. Y. Kim, Y. Jiang, P. Gu and S. Li, *Sci. Adv.*, 2020, **6**, eabb8675.
188. P. Y. Kim, A. E. Ribbe, T. P. Russell and D. A. Hoagland, *ACS nano*, 2016, **10**, 6257-6264.
189. Z. Fink, P. Y. Kim, S. Srivastava, A. E. Ribbe, D. A. Hoagland and T. P. Russell, *Nano Lett.*, 2023, **23**, 10383-10390.
190. G. Lin, X. Zhu, U. Anand, Q. Liu, J. Lu, Z. Aabdin, H. Su and U. Mirsaidov, *Nano Lett.*, 2016, **16**, 1092-1096.
191. M. Cui, C. Miesch, I. Kosif, H. Nie, P. Y. Kim, H. Kim, T. Emrick and T. P. Russell, *Nano Lett.*, 2017, **17**, 6855-6862.
192. D. M. Balazs, T. A. Dunbar, D.-M. Smilgies and T. Hanrath, *Langmuir*, 2020, **36**, 6106-6115.
193. A. Huerre, F. Cacho-Nerin, V. Poulichet, C. E. Udoh, M. De Corato and V. Garbin, *Langmuir*, 2018, **34**, 1020-1028.
194. P. Y. Kim, Z. Fink, Q. Zhang, E. M. Dufresne, S. Narayanan and T. P. Russell, *ACS nano*, 2022, **16**, 8967-8973.
195. J. D. Berry, M. J. Neeson, R. R. Dagastine, D. Y. Chan and R. F. Tabor, *J. Colloid Interface Sci.*, 2015, **454**, 226-237.
196. M. Nagel, T. A. Tervoort and J. Vermant, *Advances in colloid and interface science*, 2017, **247**, 33-51.
197. C. Tian, J. Feng, H. J. Cho, S. S. Datta and R. K. Prud'homme, *Nano Lett.*, 2018, **18**, 4854-4860.
198. Y. Zhang, S. Wang, J. Zhou, R. Zhao, G. Benz, S. Tcheimou, J. C. Meredith and S. H. Behrens, *Langmuir*, 2017, **33**, 4511-4519.
199. K. Du, E. Glogowski, T. Emrick, T. P. Russell and A. D. Dinsmore, *Langmuir*, 2010, **26**, 12518-12522.

200. J. Smits, R. P. Giri, C. Shen, D. Mendonça, B. Murphy, P. Huber, K. Rezwan and M. Maas, *Langmuir*, 2021, **37**, 5659-5672.
201. N. Bizmark, M. A. Ioannidis and D. E. Henneke, *Langmuir*, 2014, **30**, 710-717.
202. X. Hua, M. A. Bevan and J. Frechette, *Langmuir*, 2018, **34**, 4830-4842.
203. X. Hua, J. Frechette and M. A. Bevan, *Soft matter*, 2018, **14**, 3818-3828.
204. V. Garbin, J. C. Crocker and K. J. Stebe, *Langmuir*, 2012, **28**, 1663-1667.
205. V. Pauchard, J. P. Rane and S. Banerjee, *Langmuir*, 2014, **30**, 12795-12803.
206. A. A. Isari, A. Ghaffarkhah, S. A. Hashemi, H. Yousefian, O. J. Rojas and M. Arjmand, *Adv. Funct. Mater.*, 2024, 2402365.
207. N. Jaensson and J. Vermant, *Curr. Opin. Colloid Interface Sci.*, 2018, **37**, 136-150.
208. M. Pepicelli, *Complex fluid-fluid interfaces: the interplay between interfacial tension and viscoelasticity*, ETH Zurich, 2017.
209. L. E. Scriven, *Chemical Engineering Science*, 1960, **12**, 98-108.
210. H. Brenner, *Interfacial transport processes and rheology*, Elsevier, 2013.
211. J. C. Slattery, L. Sagis and E.-S. Oh, *Interfacial transport phenomena*, Springer Science & Business Media, 2007.
212. M. Pepicelli, T. Verwijlen, T. A. Tervoort and J. Vermant, *Soft Matter*, 2017, **13**, 5977-5990.
213. S. Reynaert, C. F. Brooks, P. Moldenaers, J. Vermant and G. G. Fuller, *Journal of Rheology*, 2008, **52**, 261-285.
214. T. Verwijlen, P. Moldenaers, H. A. Stone and J. Vermant, *Langmuir*, 2011, **27**, 9345-9358.
215. S. Fitzgibbon, E. S. Shaqfeh, G. G. Fuller and T. W. Walker, *Journal of Rheology*, 2014, **58**, 999-1038.
216. S. Choi, S. Steltenkamp, J. Zasadzinski and T. Squires, *Nat. Commun.*, 2011, **2**, 312.
217. I. Williams and T. M. Squires, *J. R. Soc. Interface*, 2018, **15**, 20170895.
218. C.-C. Chang, A. Nowbahar, V. Mansard, I. Williams, J. Mecca, A. K. Schmitt, T. H. Kalantar, T.-C. Kuo and T. M. Squires, *Langmuir*, 2018, **34**, 5409-5415.
219. S. Vandebril, A. Franck, G. G. Fuller, P. Moldenaers and J. Vermant, *Rheologica Acta*, 2010, **49**, 131-144.
220. E. C. Hollenbeck, J. C. Fong, J. Y. Lim, F. H. Yildiz, G. G. Fuller and L. Cegelski, *Biophysical journal*, 2014, **107**, 2245-2252.
221. G. G. Fuller and J. Vermant, *Annual review of chemical and biomolecular engineering*, 2012, **3**, 519-543.
222. S. Knoche, D. Vella, E. Aumaitre, P. Degen, H. Rehage, P. Cicuta and J. Kierfeld, *Langmuir*, 2013, **29**, 12463-12471.
223. A. Javadi, J. Krägel, A. Makievski, V. Kovalchuk, N. Kovalchuk, N. Mucic, G. Loglio, P. Pandolfini, M. Karbaschi and R. Miller, *Colloids and Surfaces A: Physicochemical and Engineering Aspects*, 2012, **407**, 159-168.
224. D. Pradilla, S. Simon, J. Sjoblom, J. Samaniuk, M. Skrzypiec and J. Vermant, *Langmuir*, 2016, **32**, 2900-2911.
225. J. Hegemann, S. Knoche, S. Egger, M. Kott, S. Demand, A. Unverfehrt, H. Rehage and J. Kierfeld, *J. Colloid Interface Sci.*, 2018, **513**, 549-565.
226. K. D. Danov, R. D. Stanimirova, P. A. Kralchevsky, K. G. Marinova, N. A. Alexandrov, S. D. Stoyanov, T. B. Blijdenstein and E. G. Pelan, *J. Colloid Interface Sci.*, 2015, **440**, 168-178.
227. A. Ghaffarkhah, E. Hosseini, M. Kamkar, A. A. Sehat, S. Dordanihaghighi, A. Allahbakhsh, C. van der Kuur and M. Arjmand, *Small*, 2021, 2102683.

Data Availability Statement

No primary research results, software or code have been included and no new data were generated or analysed as part of this review.